

Establishing a sea bottom model by applying a multi-sensor acoustic remote sensing approach

Proefschrift

ter verkrijging van de graad van doctor
aan de Technische Universiteit Delft,
op gezag van de Rector Magnificus prof. ir. K.C.A.M. Luyben,
voorzitter van het College voor Promoties,
in het openbaar te verdedigen op vrijdag 5 juli 2013 om 12:30 uur

door

Kerstin SIEMES

Diplom-Ingenieurin
Rheinische Friedrich-Wilhelms-Universität Bonn, Duitsland
geboren te Wermelskirchen, Duitsland

Dit proefschrift is goedgekeurd door de promotoren:

Prof. dr. D.G. Simons

Prof. dr. J.-P.O.F.G. Hermand

Samenstelling promotiecommissie:

Rector Magnificus,	voorzitter
Prof. dr. D.G. Simons,	Technische Universiteit Delft, promotor
Prof. dr. J.-P.O.F.G. Hermand,	Université libre de Bruxelles, promotor
Prof. dr. ir. O.D. Debeir,	Université libre de Bruxelles
Prof. dr. A. Stepnowski,	Gdansk University of Technology
Prof. dr. C. de Mol,	Université libre de Bruxelles
Prof. dr. ir. C.P.A. Wapenaar,	Technische Universiteit Delft
Dr. ir. M. Snellen,	Technische Universiteit Delft
Prof. dr. G.J.W. van Bussel,	Technische Universiteit Delft, reservelid

Université libre de Bruxelles and Delft University of Technology made important contributions to the work described in this dissertation.

The research was supported by The Netherlands Organization for Applied Research (TNO) and by the U.S. Office of Naval Research.

ISBN 978-90-8891-641-0

Copyright ©2013 by Kerstin Siemes

Some rights reserved. Chapters 4 and 5 are adapted from published work (DOI:10.1109/JOE.2010.2066711 and DOI:10.1121/1.3569718) and are reprinted here, with permission.

Typeset by the author with the L^AT_EX Documentation System.

Cover design: Proefschriftmaken.nl || Uitgeverij BOXPress

Printed by: Proefschriftmaken.nl || Uitgeverij BOXPress

Published by: Uitgeverij BOXPress, 's-Hertogenbosch

Establishing a sea bottom model by applying a multi-sensor acoustic remote sensing approach

Dissertation

submitted for the degree of Doctor in Engineering Sciences

Kerstin SIEMES

2012/2013

thesis directors:

Prof. dr. J.-P.O.F.G. Hermand
Prof. dr. D.G. Simons



Contents

1	Introduction	1
1.1	Historic background of underwater measurements	2
1.2	Recent developments in classifying the sea bottom	2
1.3	Research objectives	4
1.4	Outline of the thesis	4
2	Underwater acoustic sensors	7
2.1	Sensors for hydrographic surveying	7
2.1.1	Seafloor mapping tools	8
2.1.2	Profiling tools	9
2.2	Dedicated acoustic systems	10
3	Trial areas and measurements	13
3.1	The MREA/BP'07 trial	13
3.1.1	Equipment and measurements	15
3.1.2	Bathymetry	17
3.1.3	Properties of the sea bottom	20
3.2	CBBC'04	23
3.2.1	Equipment and measurements	23
3.2.2	Bathymetry	24
3.2.3	Properties of the sea bottom	25
4	Classification of SBES data	27
4.1	The SBES echo and its parameters	27
4.2	Phenomenological classification by echo shape parameters	30
4.2.1	Principal component analysis (PCA) and clustering	30
4.2.2	Application of the PCA to the MREA/BP'07 data	31
4.3	Model-based classification using the full echo envelope	35
4.3.1	Method	35
4.3.2	Application of the echoshape model to the CBBC'04 data	37
4.3.3	Applicability of the echoshape model to an environment with soft sediments	40
4.4	Model-based classification using the echo energy	41
4.4.1	Method	41
4.4.2	Application of the echo energy model to the CBBC'04 area	42

4.5	Conclusions	45
5	Bayesian classification of MBES data	47
5.1	The Bayesian approach	48
5.2	Application of the Bayesian approach to the MREA/BP'07 data	52
5.3	Conclusions	54
6	Efficient geoacoustic inversion strategies	55
6.1	Multi-frequency geoacoustic inversion approaches	56
6.2	Establishing an optimal inversion strategy	57
6.2.1	Criteria for comparing inversion strategies	58
6.2.2	Settings of the global optimization method	61
6.2.3	Frequency dependence of the inversion results	70
6.3	Conclusions	73
7	Geoacoustic inversion in practice	75
7.1	Confirmation of the optimal inversion strategy	75
7.1.1	Inversion of synthetic vs. real data	76
7.1.2	Confirmation by hydrographic data	81
7.2	The effect of environmental variability on the inversion results	84
7.2.1	Very soft sediments and the presence of gas	84
7.2.2	Environments with a thick sediment layer	87
7.3	Conclusions	91
8	An integrated environmental picture	93
8.1	A combined survey	93
8.2	Interpretation of the environmental picture	94
8.3	Perspective	95
A	Sediment characteristics	97
A.1	Sampling and analysis	97
A.2	Sediment type definitions	97
A.3	Sediment properties affecting acoustic signals	100
B	Previous samples taken in the research areas	101
B.1	Sediments in the MREA/BP'07 area	101
B.2	Sediments in the CBBC'04 area	103
C	Environmental models	105
C.1	Sound propagation in the water column	105
C.2	Sound interaction with the water–sediment interface and sediment body	106
D	Modeling the acoustic field	111
D.1	Solving the acoustic wave equation	112
D.2	Normal mode modeling	112
D.2.1	Normal modes in a lossy medium	114

D.2.2	The relevance of modes	114
D.2.3	Relations between the normal modes and the environment	117
E	Global optimization	119
E.1	Overview of global optimization strategies	119
E.2	Differential Evolution (DE)	120
E.2.1	Optimization strategy	120
E.2.2	The performance of DE in inverting sediment properties	122
	Bibliography	129
	Summary	135
	Samenvatting	139
	Acknowledgements	143
	Curriculum vitae	145

Introduction

About 70% of the Earth's surface is covered by sea water [1]. What is lying beneath the sea surface, however, remained unknown to mankind for ages. It was not until the industrial flourishing of the nineteenth century that one began to explore the ocean scientifically [2]. Today, modern technology enables an even more detailed investigation of the underwater environment.

Investigations of the ocean have already brought forth a global understanding of the underwater topography. From this, the deep ocean basins are known to reach several kilometers of depth, whereas the wide flat margin of the continental shelf, spanning along the continents with an average width of 70-75 km, is less than 300 m deep. Containing most of the accessible resources for commercial use, such as fish, oil, gas, and sediment deposits, the shallow continental shelf has become focus of a large amount of human activities at sea, including shipping, naval operations, and coastal engineering. Many of these activities at sea require detailed information about the ocean environment to guarantee safe navigation and to enable the discovery and localization of resources. This motivates the gathering of information about properties of the water column, the water-sediment interface and sediment layers.

Techniques for monitoring the underwater environment, however, are limited. Commonly, cost intensive and locally restricted sampling methods are applied. An appropriate remote sensing technique, on the opposite, would allow for a larger coverage. Optical methods are not applicable beyond a few meters of depth since light is absorbed easily by the sea water. The same holds for radio waves. Sound, on the other hand, is less attenuated in the water column. Dependent on its frequency, sound can also penetrate into the sediment body, where sound waves are altered according to the prevailing environmental condition. Sound waves, therefore, are most suited for obtaining information about the underwater environment and have been used intensively for this purpose for already more than half a century. In this period, different acoustic systems have been developed to fulfill specific tasks in observing the underwater environment, including bathymetric measurements, imaging the seafloor, and detecting sediment layers. Still, the interpretation of acoustic measurements is a challenging task. This especially holds for shallow water environments, where sound propagation is rather complex due to interaction of sound with the boundaries at the sea surface and seafloor.

This thesis analyses the effect of varying bottom properties on acoustic signals and provides valuable information for refining environmental models. From this analysis, also an efficient strategy for classifying sea bottom sediments is deduced.

1.1 Historic background of underwater measurements

At the early stage of ocean exploration, the first and foremost parameter to measure was the water depth since knowledge of it enables safe navigation. Ancient navigation at sea was dependent on rather simple but intricate mechanical soundings of the water depth with the aid of a burlap rope or lead line. This technique did not change much for centuries. However, measurements were facilitated in the course of the industrial flourishing of the nineteenth century. This also enabled large-scale research projects on the underwater environment, such as the Challenger expedition in the years 1872-1876. This expedition was carried out in an attempt to understand the environment below the sea surface, thereby covering a large range of measurements, including besides detailed bathymetric measurements also sampling of the sea bottom [3].

Although sound was known to travel in the ocean since the observation of distant shipping noise by Leonardo da Vinci in 1490, underwater acoustic applications emerged relatively late. The first underwater sound speed measurements were carried out in the Lake Geneva by D. Colladon and C. Sturm in 1826. However, it took almost another century before underwater sound was applied for measuring distances. In 1912, L. F. Richardson obtained a patent on echo ranging based on sound. This principal found application during World War I (1914-1918). In this time, the focus of underwater research got directed toward object detection and localization. In order to deal with the threat of enemy submarines, one began to passively listen to their noise and inferring their positions. Research on active acoustics followed shortly thereafter. In 1917, P. Langevin was the first to use electrically generated sound (generated by a piezoelectric transducer) in underwater acoustics. Using an active source emitting high-frequency pulses, one could now listen to the reflections from any target, independent of its own noise. The distance to the object was obtained by time measurements of traveling pulses. Whether an object was moving could be discerned by observing changes in the tone, which occur due to the Doppler effect. The first active sonar (sound navigation and ranging) system has been invented in the 1920s and research on these systems has been intensified during World War II (1939-1945). After the war, active sonar systems slowly replaced the lead line for bathymetric measurements. Since then, they have been systematically used for depth measurements and mapping of the oceans topography. These first systems were single-beam echosounders (SBESs), using a pulsed signal. From these, diverse systems emerged, including subbottom profilers (early 1930s), side-scan sonars (1960s), and multibeam echosounders (late 1970s).

1.2 Recent developments in classifying the sea bottom

The classical technique applied for classification of the sea bottom material is based on taking samples of the sediments. These measurements and their evaluations are expensive, time consuming, and provide information at point positions only. Therefore, significant research effort has been dedicated to methods allowing of remote classification for the sea bottom. Acoustic signals were found to be a suitable tool for sea bottom classification purposes, since they contain information on sea bottom characteristics. One of the first to employ multibeam echosounder signals for environmental characterization was de Moustier [4]. Since then, various classification methods using underwater acoustics have been developed over the last few decades.

A large part of the research on acoustic means for sediment classification has focused on hydrographic systems that nowadays are widely available, such as multibeam echosounders (MBESs), [4–9]; single-beam echosounders (SBESs), [10–16]; and side scan sonars (SSSs), [17]. In general, these approaches can be divided into two groups, the phenomenological (or empirical) and the model-based (or physical) approaches. In the phenomenological approaches, features such as energy or time spread are determined from the received echo signals. These features are known to be indicative for the sediment type. However, independent measurements, such as sediment samples or cores, are needed to link the sediment classes, obtained from signal features, to real sediment properties or sediment type. In contrast, the model-based approaches make use of physical models and determine the seafloor type by maximizing the match between modeled and measured signals or signal features, where seafloor type or parameters indicative for seafloor type are input into the model. In principle, no independent measurements are needed and the application of a model-based approach directly provides the sediment parameters. Approaches presented in literature mainly differ in the complexity of the sound propagation and sediment interaction accounted for.

Contrary to these widespread commercially available systems, research has also focused on the use of dedicated systems, such as vertical line arrays spanning a large part of the water column. Geoacoustic inversion techniques have been developed and have demonstrated to adequately assess the physical properties of the sediments [18–23].

The advantage of the hydrographic systems is that they are widely used already, and therefore no additional hardware is required. The disadvantage, however, is that sediment information often is obtained only at positions along the ship's track since these systems typically are mounted on board of a ship. In addition, these systems often employ high frequencies in the order of several hundreds of kilohertz, sensing the upper part of the sediment only. Exceptions hold for systems such as the towed ocean bottom instrument TOBI [24], operating at a few tens of kilohertz. However, such systems were not available for the current study.

Frequencies employed with dedicated line arrays typically lie in the range of several hundreds of hertz, thereby penetrating and characterizing also the deeper sediment layers. Another advantage of these systems is that the geoacoustic sediment properties, in principle, can be obtained over a large area without the need for a dedicated ship to navigate over all parts of interest within the area. However, most of the systems employed in previous experiments are not suited for application in an operational context since they are based on relatively complex systems, with for example highly instrumented vertical line arrays spanning the entire water column as the receiving system. In the late 1990s the use of sparse arrays of hydrophones down to a single hydrophone combined with frequency-coherent, model-based matched filter processing was shown to produce correct geoacoustic parameters [25]. Further experimental work demonstrated that geoacoustic inversion results can be operationally obtained using a short array deployed from a small vessel [26] or an underwater robot [27]. For the same purpose the use of vector sensors is investigated [28].

1.3 Research objectives

In this thesis, we further investigate means of efficiently obtaining a detailed picture of the underwater environment. For this purpose, a large number of acoustic techniques for the classification of sea bottom sediments is analyzed and assessed. The following main research objective is defined.

- Establish a 3D model of a shallow underwater environment with the aid of acoustic classification techniques.

For achieving this, the following secondary objectives are aimed at.

- Existing techniques are extended to increase their efficiency.
- Strengths and weaknesses of acoustic techniques for classifying the sea bottom sediments are defined and used for increasing the efficiency in underwater environmental characterization by combining different techniques.

In order to fulfill these aims, acoustic data of two environmentally different regions are investigated.

1.4 Outline of the thesis

This thesis is organized as follows.

Chapter 2 introduces the sensors typically applied for obtaining characteristics of the sea bottom sediments. The focus is on acoustic sensors. Both, commercial hydrographic systems and dedicated line arrays are treated.

In *Chapter 3*, the datasets used throughout this research are described and placed into their environmental context. Data from two different locations, one in the Mediterranean Sea and the other in the North Sea, are considered. With this selection, a large range of sediment types is covered, ranging from a variety of clay fractions in the Mediterranean to silt, sand, and gravel in the North Sea. This variety of sediments allows for a detailed assessment of sediment classification techniques, as provided in the following.

The *Chapters 4–7* address different approaches for obtaining environmental information from acoustic data. The aim is to assess their performance for practical application, which is the mapping of sediment parameters over an area of interest.

The first system considered is an SBES. In *Chapter 4*, three different classification approaches for SBES signals are presented and evaluated: one empirical method based on echo shape parameters and two model-based approaches employing either the full echo envelope or again shape parameters. The empirical method employs a principal component analysis. The basic principles of the two model-based approaches are based on [13] and [16].

In *Chapter 5* a Bayesian approach for classifying MBES backscatter strength is presented. This approach is based on [8], who introduced it for a single angle. Here, the approach has been extended to be capable of handling a large number of beam angles.

The *Chapters 6 and 7* are dedicated to the geoacoustic inversion of environmental parameters from the acoustic field observed by hydrophone arrays. First, synthetic data are considered for performance tests in *Chapter 6*. These synthetic inversions then provide an

optimal inversion strategy, which is used for inversion of the measured acoustic field in three environments in *Chapter 7*. Here, the focus is on the effect of environmental variability on the parameter estimates.

Finally, *Chapter 8* concludes with a review of the major findings of this thesis, combining the efforts to a comprehensive environmental picture. Also recommendations for further research are presented.

Underwater acoustic sensors

Since the first sonar emerged in the early twentieth century, numerous acoustic systems have been developed, including single- and multibeam echosounders, side-scan sonars, parametric arrays, seismic systems, and dedicated systems composed of several receivers and/or sources. Each of these systems was developed for slightly different purposes, resulting in the use of different frequencies, apertures, or position in the water column.

Conventional systems designed for hydrographic surveying, such as single- and multi-beam echosounders, are recently employed for the classification of seafloor sediments. Furthermore, dedicated systems, such as hydrophone arrays developed for monitoring the acoustic field, allow for inverting environmental parameters. While most of the hydrographic systems employ high frequencies in the range of a few ten to a few hundred kilohertz and provide insight into the upper part of the seabed only, the dedicated systems, operating at frequencies typically in the range of several hundred hertz, enable us to obtain environmental parameters also for the deeper sediment layers. This motivates a combined use of the different types of systems when we aim at establishing a 3D picture of the underwater environment that helps understanding the acoustic processes.

The current chapter describes the principal of operation and the acquired data for each of the systems considered. Most of this information is gathered from [1].

2.1 Sensors for hydrographic surveying

Hydrographic systems are commercially available systems for underwater surveying. In general, they are mounted on or towed by a vessel. Different hydrographic systems initially have been designed for specific purposes, such as depth measurements, mapping of the seafloor, and profiling of sediment layers. Their scope, however, has broadened recently.

Most commonly used for depth measurements are single-beam echosounders (SBESs) and multibeam echosounders (MBESs). Echosounders, however, are multi-functional systems. In the last few decades, they have also been considered for sediment classification. Echosounders are also capable for mapping purposes, a task that was originally dedicated to side-scan sonars. While all these systems, due to their use of generally high frequencies, are restricted to observations of the upper thin layer of sediments, specific tools are dedicated to sediment profiling. These include seismic systems, typically using chirp signals or sound created by vibrating plates (boomers), subbottom profilers, and systems operating on parametric arrays.

In the following, we focus on those hydrographic systems available for the current study, which are SBESs, MBESs, and seismic systems. Other hydrographic systems are addressed only briefly in this chapter.

2.1.1 Seafloor mapping tools

The side-scan sonar (SSS) was the first system designed purely for imaging the seafloor. Later, the multibeam echosounder (MBES) emerged as a combination of the bathymetry measuring single-beam echosounder (SBES) and the imaging SSS, providing input to geological maps. While SSS and MBES are commonly used for sediment classification, recently also the SBES was recognized to have this potential. Despite its low coverage, the SBES also can be used for mapping sediment classes.

Side-scan sonars provide images of the seafloor, using reflected intensities recorded versus time. These systems generally consist of two long antennas mounted on each side of a fish, which is towed close to the seafloor to obtain high resolution (see Fig. 2.1). An SSS sends pulsed signals with frequencies in the order of 100–500 kHz. These signals are narrow in along-track direction and wide in across-track direction. They can thus cover large distances. However, for most of the systems no angular information or other geometrical properties are available. Exceptions hold for interferometric systems. Classification is, therefore, often based on image processing.



Figure 2.1: Schematic of a survey with a side-scan sonar (left) and illustration of a Klein 5900 side-scan sonar (right, <http://www.1-3klein.com/>).

Echosounder systems are commonly hull-mounted. The central part of an echosounder is its transducer, which contains both a source to transmit acoustic signals and a receiving unit. The transducer of an SBES commonly points at nadir direction and has a small aperture of a few degrees. The aperture of an MBES is also narrow along-track (often 1° or less), however, is large across-track, allowing it to cover a wide swath. An illustration of the coverage of SBES and MBES systems is given in Fig. 2.2. Also shown are typical sonar heads.

Within the transducer head, pulsed signals are generated by the source, commonly applying a piezo-electric material that is caused to change its shape when exposed to a voltage and which returns to its original shape when the voltage is removed. This technique was first applied in the field of underwater acoustics by P. Langevin during World War I.

The generated pulses travel toward the seafloor, where they are scattered and partly reflected back to the transducer. Here, the two-way travel time of the arrivals and the echo intensities per time are recorded. In case of an MBES, these recordings are done per beam, after beamforming has been applied. Given the sound speed in the water column, water depth can be determined from the travel time of the first arrival. Further, information on the bottom properties is contained in the shape and intensity of the received signal. However, to determine the actual sediment properties, corrections for the transmission loss, footprint effects, and the directivity of the sensor are standardly applied.

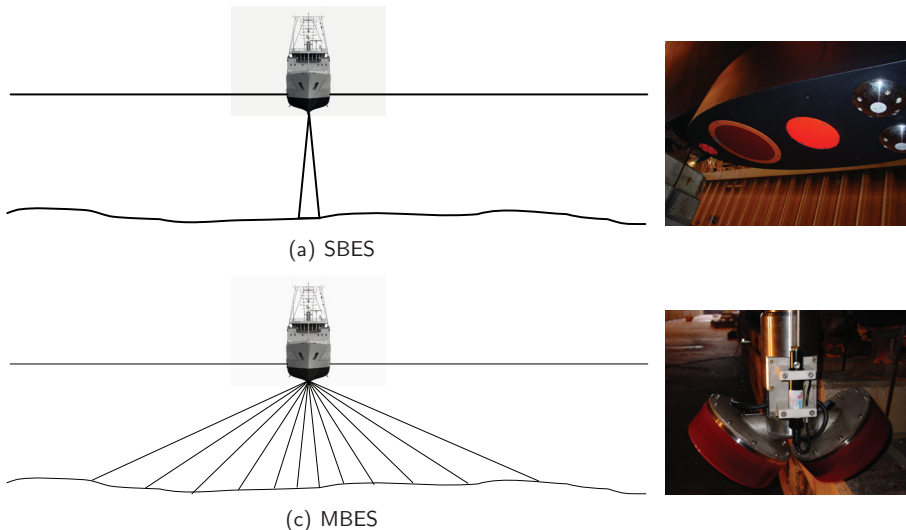


Figure 2.2: Schematic of the coverage (left) and illustration of typical sonar heads (right) of an SBES and MBES system, respectively. The SBES shown is a EA600 and the MBES is a EM3000D dual head system, both manufactured by Kongsberg.

2.1.2 Profiling tools

Two types of hydrographic systems are generally applied for profiling of the sea bottom sediments. These are subbottom profilers and seismic systems.

Seismic systems generally consist of a towed source and a towed receiving array as schematized in Fig. 2.3. The source generates low frequency signals, which are capable to penetrate deep into the sediment body where they can sense the deep sediment layering.

Different types of sources exist. Commonly used in shallow water surveying are boomer sources and chirp sources. A boomer stores energy in capacitors. When released, this energy causes a plate to move, resulting in a seismic pulse. Chirp sources, on the other hand, create sound with increasing or decreasing frequency.

The measurements are based on the acoustic impedance contrast between two distinct sediment layers (see App. C). These interfaces cause reflections, which are detected by the receiving array. Travel time provides the depth of each layer. The signals thus provide a vertical cross section of the sediment layers.

Subbottom profilers use the concept of seismics together with a structure similar to an SBES. An illustration is given in Fig. 2.4. They send signals in normal direction. Contrary to an SBES, subbottom profilers commonly employ low frequencies (1-10 kHz) in form of frequency modulated signals. Lower frequencies, in general, require a wider aperture at the expense of resolution. An exception are parametric sources, which have a narrow directivity. Detected are reflections from impedance contrasts rather than surface scattering.

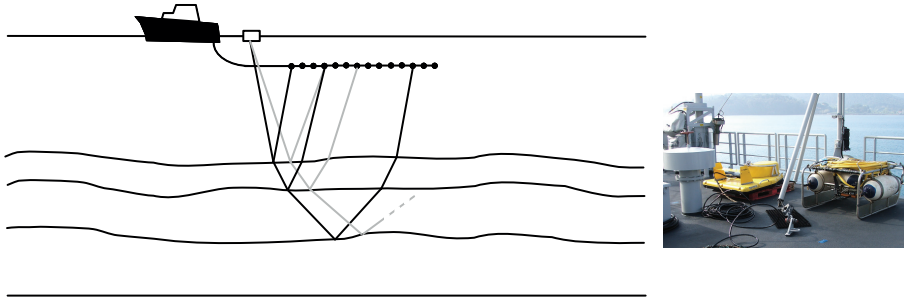


Figure 2.3: Schematic of a seismic survey (left) and illustration of two seismic systems (right): an Edgetech X-Star and a Uniboom system.

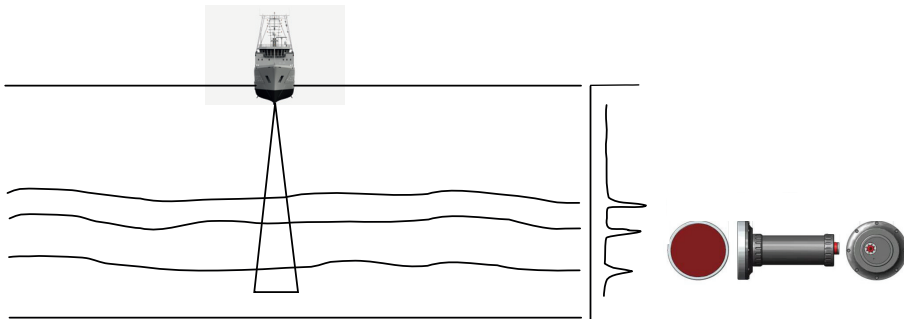


Figure 2.4: Principle of subbottom profiling (left) and illustration of a Tritech SeaKing parametric subbottom profiler (right, <http://www.tritech.co.uk/>).

2.2 Dedicated acoustic systems

Dedicated systems, such as hydrophone arrays, have been developed for monitoring the acoustic field. While high-frequency hydrographic systems provide insight into the upper part of the sea bottom only, the dedicated systems, operating at frequencies typically in the range of a few hertz to several hundred hertz, can also sense deeper sediment layers. Opposite to seismic systems, the dedicated systems allow for obtaining environmental parameters, using geoacoustic inversion.

Monitoring the acoustic field is generally performed by employing a source, sending either a single tone or a modulated waveform, and a set of receivers placed in a distance (generally a few hundred meters to several kilometers) to the source. Commonly, the receiving hydrophones are arranged in a dense array, which is either moored or towed behind a ship sailing over the area of interest (Fig. 2.5). Two types of arrays are in use: the horizontal line array (HLA) and the vertical line array (VLA). Nowadays, research is done towards sparse arrays down to a single hydrophone. Of special interest are drifting sparse arrays, which allow for covering large areas without the need of a dedicated ship to sail and which can enter also shallow water areas.

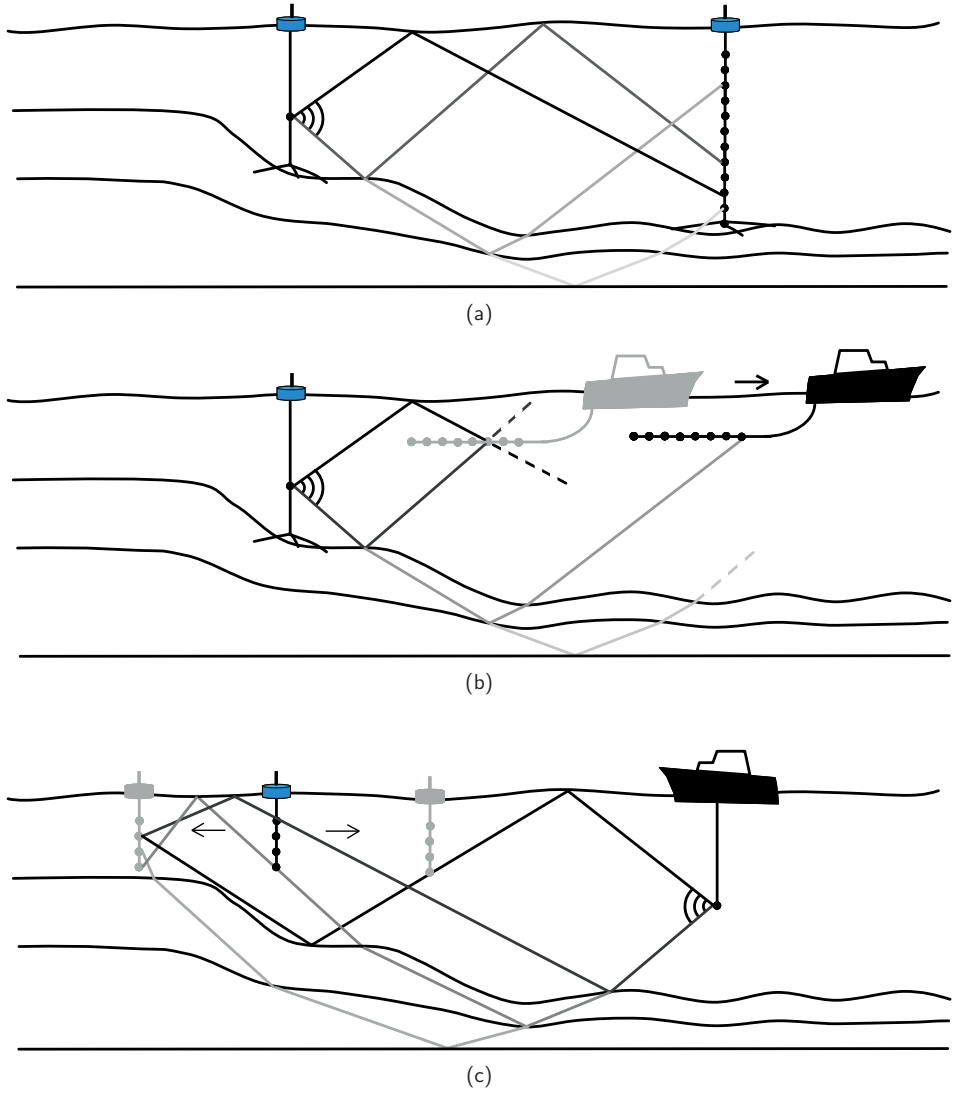


Figure 2.5: Possible source–receiver configurations for VLAs: (a) moored source and receiver, (b) moored source and towed receiver, and (c) ship-mounted source together with a sparse drifting array.

Trial areas and measurements

The present study considers data from two different sea trials, providing independent results. One is situated in the Mediterranean Sea and the other in the North Sea. The trial in the Mediterranean is more complex in terms of the amount of different acoustic measurement techniques employed. Therefore, it is well suited for establishing a multi-sensor approach, as presented throughout this thesis. The challenge, however, lies in the softness of the sediment present in this area. The trial area in the North Sea, on the other hand, features a large variety of both soft and rough/hard sediments that fall into the scope of common models. This makes it suitable for testing model-based approaches.

3.1 The MREA/BP'07 trial

The Maritime Rapid Environmental Assessment / Blue Planet (MREA/BP07) sea trial was carried out in the Mediterranean Sea in the spring of 2007. In the context of MREA, it aimed at addressing novel concepts of characterizing the underwater environment, thereby investigating means of efficiently obtaining a detailed picture of the underwater environment [26]. For this purpose, a large number of different acoustic and non-acoustic sensors have been employed. The measured parameters concern both the water column and the sediments. For a detailed description of the experiment, we refer to [29–31].

The sea trial was located in the BP 3 area southeast of Elba Island and off the coast of Grosseto, Italy, as illustrated in Figs. 3.1 and 3.2. This region was also in the focus of earlier experiments, such as the Yellow Shark experiments in 1994/1995, documented in [18, 25, 32]. These provide indications of the expected environmental conditions, making the region an ideal area for testing novel techniques of environmental classification.

The measurements considered throughout this thesis, however, were taken in a somewhat smaller region within the BP 3 area, covering the northern half of the REA I area and ranging from 10.7° to 11.0° eastern longitude and from 42.5° to 42.8° northern latitude.

This chapter is based on the following publications, with minor changes.

K. Siemes, M. Snellen, A.R. Amiri-Simkooei, D.G. Simons, and J.-P. Hermand: "Predicting spatial variability of sediment properties from hydrographic data for geo-acoustic inversion," *IEEE J. Ocean. Eng.*, 35(4), 2010. [DOI:10.1109/JOE.2010.2066711] ©2010 IEEE. Parts are reprinted, with permission.

K. Siemes, J.-P. Hermand, M. Snellen, and D.G. Simons: "Frequency and signal type dependence of the performance of broad-band geoacoustic inversion in a shallow water environment with soft sediments," in *Proceedings of the Underwater Acoustic Measurements (UAM) conference*, 2011.

M. Snellen, K. Siemes, and D. G. Simons: "Model-based sediment classification using single-beam echo sounder signals," *J. Acoust. Soc. Am.*, 129(5), 2011. [DOI:10.1121/1.3569718] ©2011 Acoustical Society of America. Parts are reprinted, with permission.

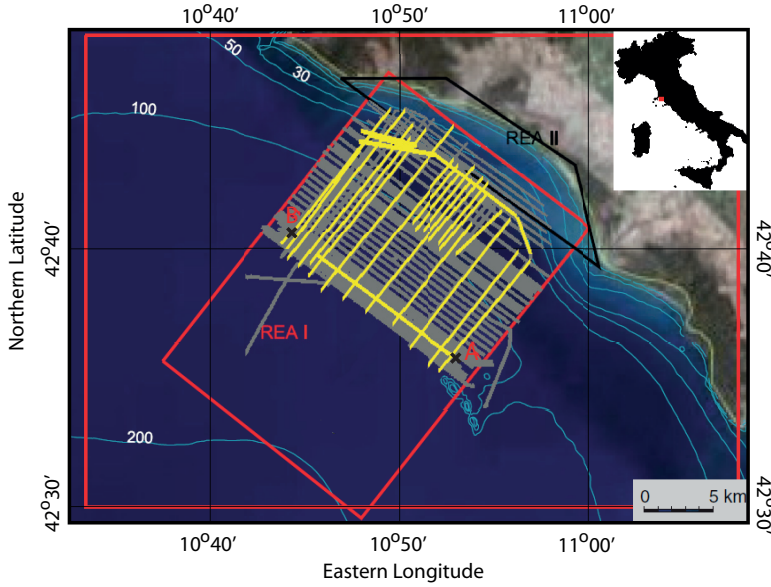


Figure 3.1: Overview of the hydrographic surveys in the MREA/BP'07 research area. The red rectangles mark the research area. Gray lines indicate the tracks of the MBES. Similar tracks are covered by the SBES measurements. Yellow lines are the seismic transects of both the X-Star and Uniboom.

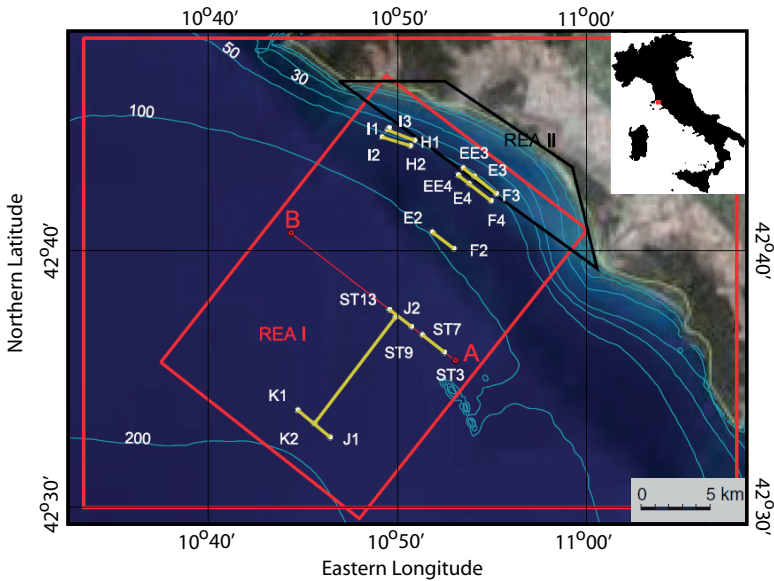


Figure 3.2: Overview of the source and receiver locations in the MREA/BP'07 research area, employed for geoacoustic inversion.

Table 3.1: Acoustic devices

Type	Specification	Frequency [kHz]	Beamwidth [°]	Direction	Ping rate [Hz]
MBES	Kongsberg EM3000D	300 (high)	1.5	normal to grazing	3–5 (max. 40)
SBES	Kongsberg EA600	200, 38, and 12 (high–medium)	7.2–15.5	normal	(max. 20)
Seismic	Edgetech X-STAR SB-512i	0.5–12 (low)	16–32	near-normal	(user-selected)
Seismic	Uniboom	0.5–15 (low)	N/A	omnidirectional	1

3.1.1 Equipment and measurements

Vessels participating in the MREA/BP'07 experiment were the North Atlantic Treaty Organization (NATO) research vessel (NRV) *Leonardo*, the Italian Ship (ITS) *Galatea* and *Are-tusa*, and the His/Her Netherlands Majestys Ship (HNLMS) *Snellius* of the Royal Netherlands Navy.

Acoustic sensors employed include both standard hydrographic systems and dedicated hydrophone arrays (see Ch. 2). The hydrographic equipment consists of an SBES, an MBES, and two seismic systems, as specified in Table 3.1.

Both the SBES and the MBES were mounted underneath the *HNLMS Snellius* of the Royal Netherlands Navy. The SBES system used is a Kongsberg EA600, operating at the frequencies 12 kHz, 38 kHz, and 200 kHz. The MBES is a Kongsberg EM3000D dual head, operating at 300 kHz with a selected ping rate of 3–5 Hz. This system has a total aperture of 130°, within which up to 254 beams are formed. Both, the SBES and MBES are considered for bathymetric measurements and classification of the upper few centimeters of the seafloor sediments. The area surveyed by the MBES is illustrated in Fig. 3.1 by the gray lines. A similar area is covered by the SBES measurements.

Indications of the deeper sediment layering are provided by the two seismic systems: an Edgetech X-STAR SB-512i operating on low-frequency (0.5–12 kHz) chirp signals, which was towed behind the HNLMS *Snellius* at a depth of 1.3 m below the sea surface, and a Uniboom system, which uses a vibrating plate to create low-frequency (0.5–15 kHz) pressure waves, mounted on a catamaran. Seismic measurements were conducted in the same area covered by the MBES and SBES. However, due to a tight schedule, the coverage with seismic data is less dense. In total, twenty eight profiles have been taken, twelve by the X-STAR and sixteen by the Uniboom. One of the X-STAR profiles was taken in the deeper part of the experimental area along the transect AB (which corresponds to the XF transect of the former Yellow Shark experiments [18, 25]). All other X-STAR profiles lie perpendicular to this profile, covering both the shallow and the deep part of the MREA/BP'07 area. The Uniboom profiles again lie perpendicular to the AB transect. Few additional transects were also sailed parallel to the coastline in the shallower part of the experimental area.

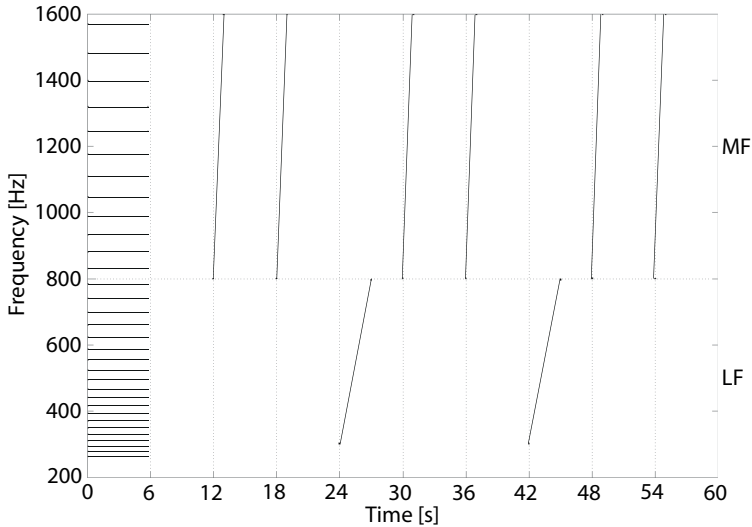


Figure 3.3: Sequence of signals as used for geoacoustic inversion. A sequence, containing 250–1600Hz multitones, 300–800Hz low-frequency (LF) chirps, and 800–1600Hz mid-frequency (MF) chirps, was sent every full minute. To ensure synchronization, triggering took place every six seconds, as indicated by the gridding of the x-axis. A sequence starts with a 5.8-s multitone, followed by a repetition of two 1.0-s MF chirps and one 3.0-s LF chirp, and ends with two 1.0-s MF chirps.

Table 3.2: Localization of the geoacoustic inversion runs.

RUN ID	Source position		Receiver position		
	ID	Stationary location (avg.) [°]	ID	Start location [°]	End location [°]
RUN 2	ST 3	N 42.6010	ST 7	N 42.6099	N 42.6049
		E 10.8748		E 10.8590	E 10.8698
RUN 3	ST 9	N 42.6176	ST 13	N 42.6284	N 42.6297
		E 10.8459		E 10.8267	E 10.8364
RUN 5	F 4	N 42.7041	E 4	N 42.7107	N 42.7072
		E 10.9202		E 10.9115	E 10.9193

Table 3.3: Properties of the geoacoustic inversion runs.

RUN ID	Ranges [m] ^a	Avg. water depth [m] ^b	Source depth [m] ^c	Receiver depth (upper hydrophone) [m] ^d
RUN 2	630–1620	106.8	N/A	18.64
RUN 3	1550–1980	107.9	92.75	11.79
RUN 5	360–1025	45.4	40.96	7.05

^aobtained from GPS measurements

^bobtained from 200 kHz SBES measurements

^cobtained from pressure sensor between the MF and LF source (MF: -30cm, LF: +30cm)

^dobtained from pressure sensor at the upper hydrophone

For investigating the actual sediment composition of the deeper part of the sediment body, a measurement configuration of a stationary source and a drifting array of hydrophones has been set up at different locations. These are depicted in Fig. 3.2. Three of these locations have been selected for the current study and are listed in Tables 3.2-3.3. In the cases (RUNs) considered, the distance between source and receiver lies between several hundred meters to two kilometers. The depth of the sensors is chosen dependent on the bathymetry, but constant for a single RUN.

The receiving unit is a vertical line array (VLA), composed of four 5-m spaced hydrophones. It was attached to a rigid-hulled inflatable boat (RHIB), launched from the HNLMS Snellius and drifting toward the NRV Leonardo. The latter was carrying both a low- (250–800 Hz) and mid-frequency (800–1600 Hz) source. These sources sent predefined sequences of acoustic signals, as shown in Fig. 3.3, including signals composed of tones at discrete frequencies (multi-tones) and frequency modulated waveforms (chirps) in both bands. The multi-tones consist of 32 frequencies, 20 in the low-frequency band and 12 in the mid-frequency band. The chirps are sampled at 1 Hz in the 300–800 Hz and 800–1600 Hz band.

The acoustic measurements have been accompanied by a set of non-acoustic measurements, including conductivity-temperature-depth (CTD) measurements to obtain actual sound speed profiles needed for accurate environmental modeling, and grab samples for validation purposes. Twenty four bottom grab samples have been taken by a Hamon grabber during the MREA/BP'07 trial. They contain information about the composition of the upper ten centimeters of the seafloor. Information about deeper sediments is available from core samples of former experiments (see Appendix B).

3.1.2 Bathymetry

Depth values, provided from the SBES and MBES measurements, cover the wide range of a few meters to approximately 130 m, as can be seen in the bathymetry map (Fig. 3.4). Starting at approximately 10 m in the shallow coastal area in the north, depth increases with the distance to the coast and shows isobaths that tend to follow the coastline. At 15-km distance to the coast, the deepest part of the area under study is reached.

Generally, the change in depth per unit of distance is small, except for a small region near the coast (between 20- and 40-m depth). This is shown in Fig. 3.5, presenting the bathymetric slope as a function of position. In general, slope values of the MREA/BP'07 experimental area lie below 1° . At some locations, such as the above mentioned region, they are slightly increased, however do not exceed 3° . Contrary to the bathymetric map, the map of slope values shows more texture. Three distinct regions can be discerned. The first one is the region of transition from the shallow to the deeper parts in the north, which shows slightly higher slope values. A second region in which high values for the slopes are present lies close to the Ombrone estuary in the east, at water depths less than 70 m. Here, the slope values indicate the presence of a regular structure, which is orientated parallel the isobaths. In the third region, an irregular, inhomogeneous structure can be found in the deep, western part of the research area, which features the softest sediments of the experimental area (see Section 3.1.3).

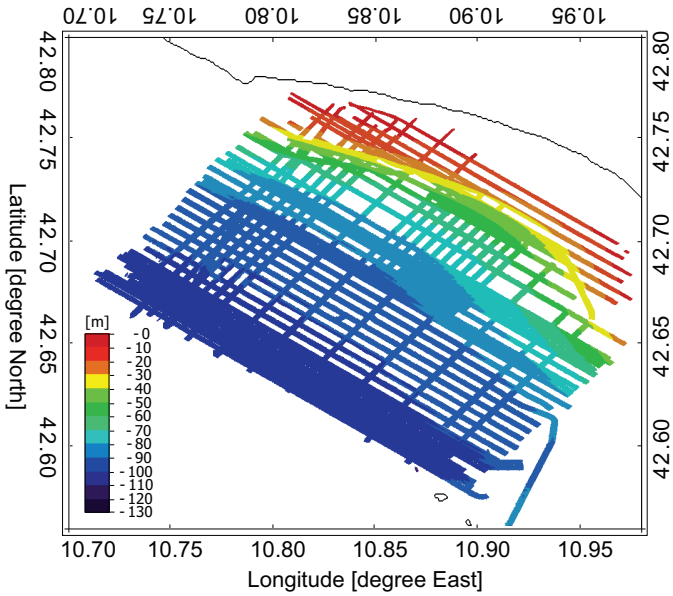


Figure 3.4: Bathymetry in the MREA/BP'07 experimental area obtained from MBES (two-way) travel time measurements (fully corrected for ship attitude and water column properties).

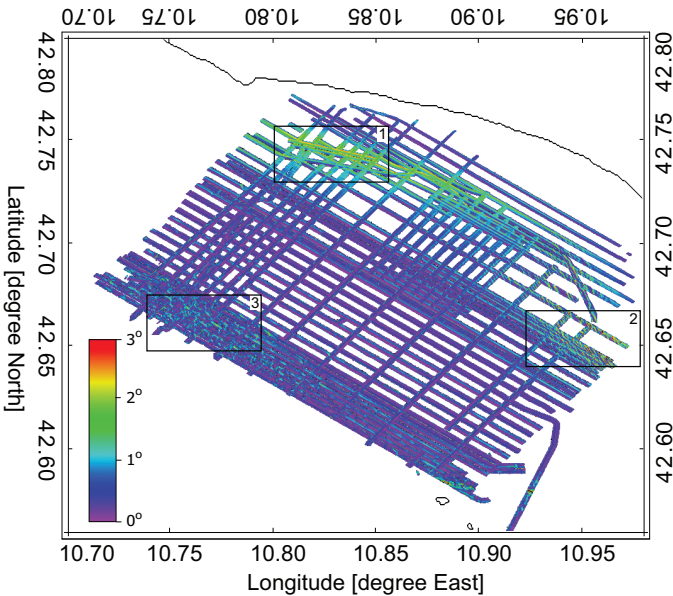


Figure 3.5: Slope in the MREA/BP'07 experimental area: 1) continuously increased slope, 2) regular structure, and 3) irregular structure.

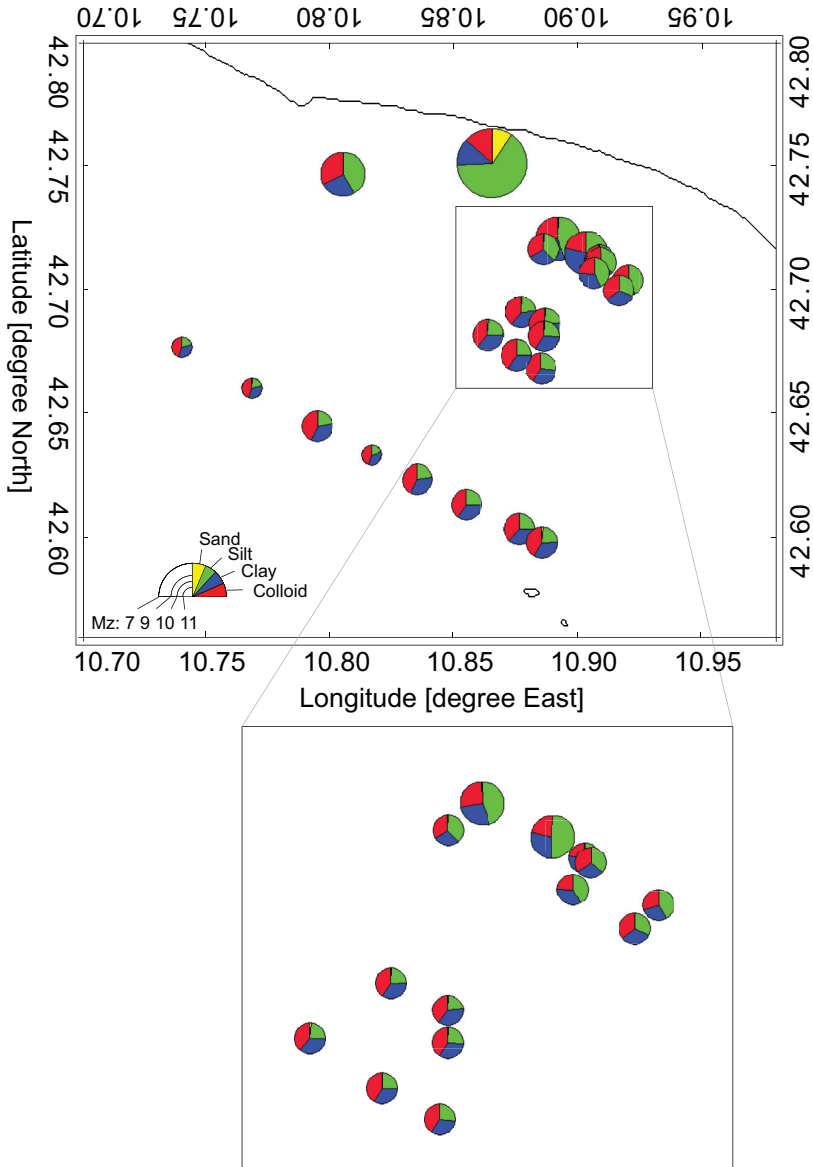
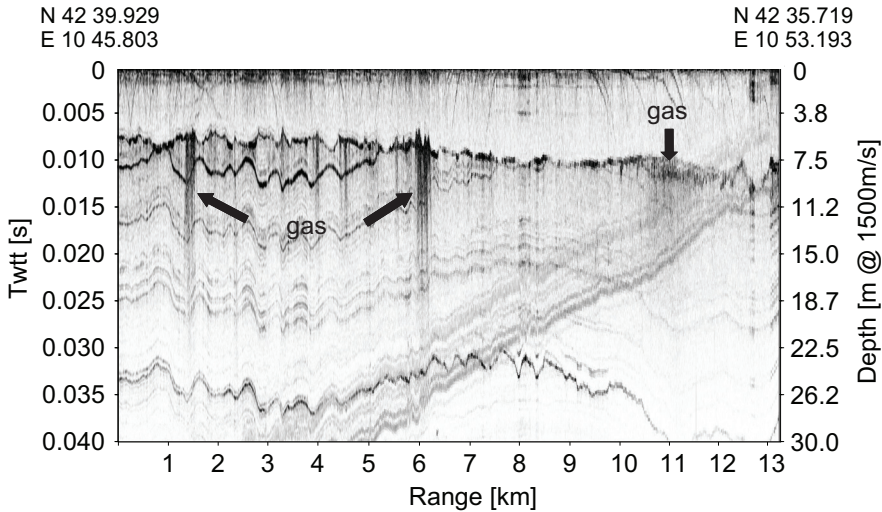


Figure 3.6: Sediment distribution in the MREA/BP'07 experimental area obtained from the analysis of grab samples taken during the experiment. This figure presents two parameters that describe the sediment type. One is the composition (sand, silt, clay, and colloid) of the sediment samples, given as pie charts, thereby accounting for all particles within a sample. The other is the mean grain size M_z of the sediment, calculated according to Eq. A.3 and rounded to integer values. M_z is indicated by the diameter of the symbols, which is reciprocally proportional to its value.

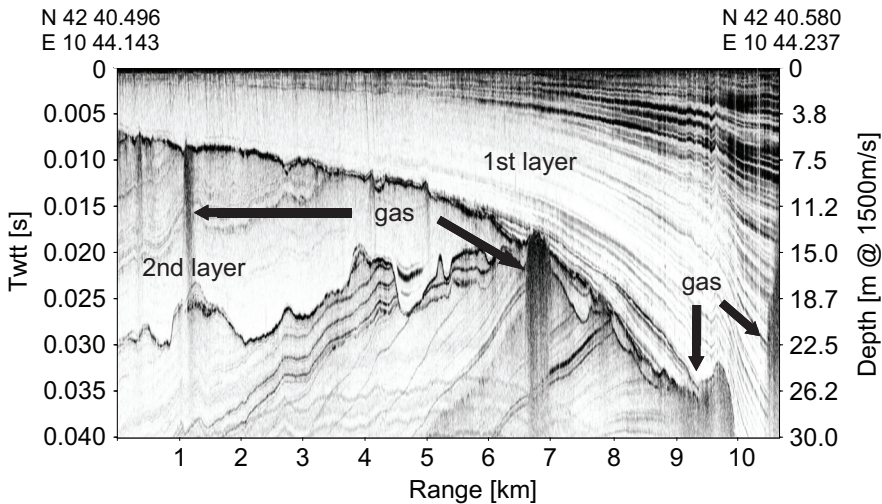
3.1.3 Properties of the sea bottom

The MREA/BP'07 area is part of the shallow continental shelf which links Elba to the Italian peninsula. The shelf was subject to large sediment supplies during the Pleistocene epoch [33]. Today, still large amounts of muddy sediments cover the basement, as documented by core samples [25], which are illustrated in Appendix B.

The presence of soft sediments is further confirmed by the bottom grab samples that



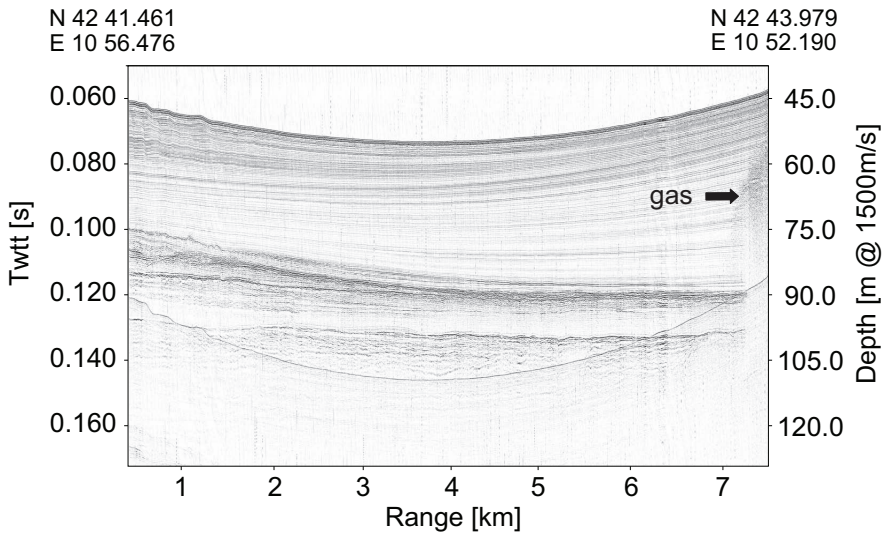
(a) X-Star profile AB.



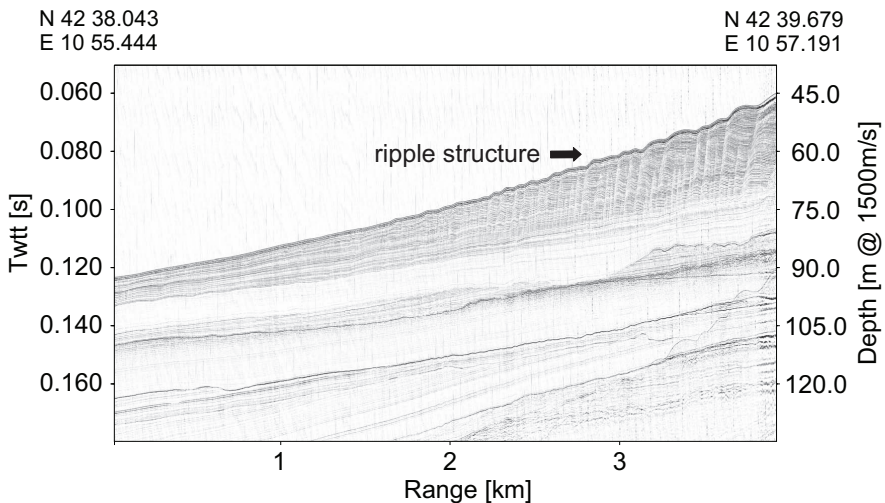
(b) X-Star profile CD.

Figure 3.7: Comparison of two seismic X-star profiles: profile AB lies in the deep part of the MREA/BP'07 area and runs parallel to the coastline, profile CD runs perpendicular to it. Both profiles start at zero travel-time at the water-sediment interface.

have been taken during the recent sea trial. The sediment distribution obtained from the grab samples is given in Fig. 3.6. The grab samples indicate very fine sediments with mean grain sizes of $M_z = 7 \phi$ to $M_z = 11 \phi$, which equal a grain diameter of 0.008 mm and less. A definition of grain sizes is given in App. A. The finest sediments with $M_z = 11 \phi$ occur in the deepest parts of the MREA/BP'07 area, while the somewhat coarser sediments with $M_z = 7 \phi$ settle close to the coast, as expected from common transport and settling



(a) Uniboom profile 13.



(b) Uniboom profile 11 (shallow part).

Figure 3.8: Comparison of two Uniboom profiles: profile 13 lies in the shallow part of the MREA/BP'07 area and runs parallel to the coastline, profile 11 runs perpendicular to it. Both profiles have zero travel time at source depth.

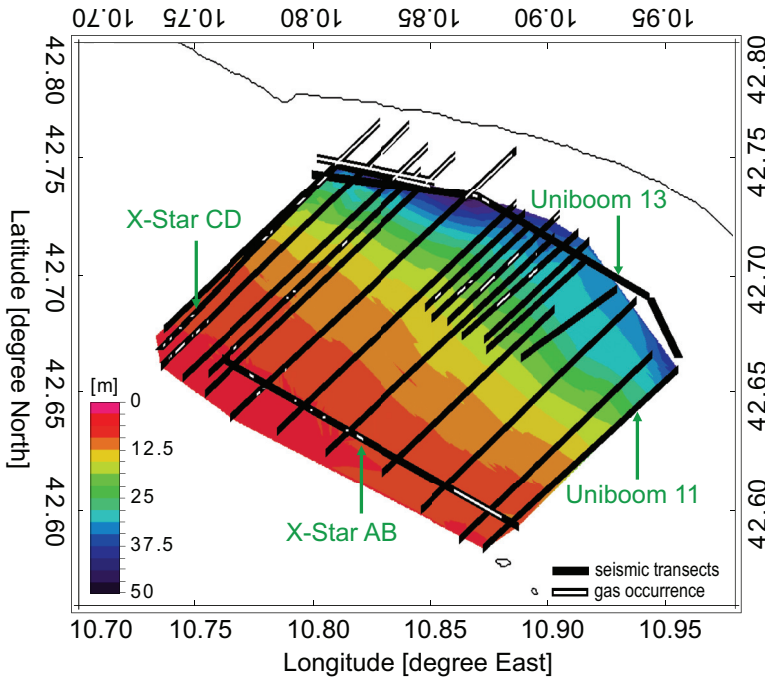


Figure 3.9: Thickness [m] of the upper sediment layer in the MREA/BP'07 research area (color) and gas deposits (white lines) along the seismic transects (black lines).

behavior. The mean grain sizes are depicted in Fig. 3.6 as the diameter of the symbols. Also, the percentages of the sand, silt, clay, and colloid contribution of the upper sediment layer, calculated from all particles within a sediment sample, are shown. From these, it can be concluded that the contribution of the finer sediments slightly increases from the shallow to the deeper part of the trial area.

Seismic profiles taken in the area additionally show variations of the sediment layer thickness. Four representative profiles are given in Figs. 3.7 and 3.8, depicting the reflections recorded by the X-STAR and UNIBOOM, respectively. Beside variation in the layer thickness, they indicate the presence of additional layering underneath the upper sediment layer and the presence of gas at several locations. This is confirmed by other profiles not shown here.

Both the sediment layer thickness, calculated from the travel time between the reflections at the water–sediment interface and the sediment–subbottom interface, and the occurrence of gas have been extracted from the seismic profiles and are mapped in Fig. 3.9. From this map it is evident that the thickness of the upper sediment layer varies with distance to the coast. In the shallow-water area this thickness is larger than 40 m, whereas it amounts to about 5 m only in the deepest part.

Gas is found in the shallowest parts of the research area as well as at a few other spots in the deeper parts. The gas mainly remains below the first sediment layer. However, this does not hold for the shallow coastal area, where gas reaches the water–sediment interface. Here also the largest amount of gas is detected.

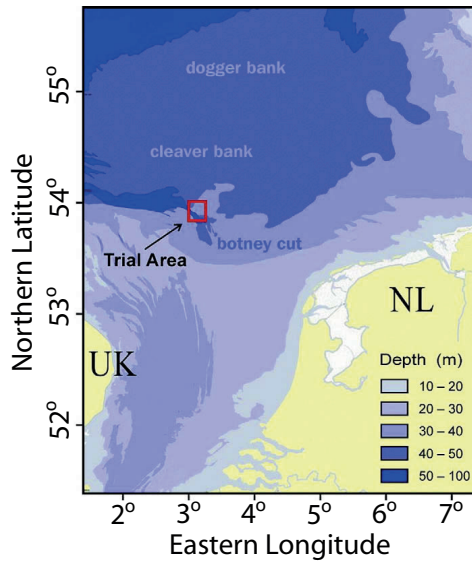


Figure 3.10: Overview of the CBBC'04 area, taken from [8]

3.2 CBBC'04

The area of the Cleaver Bank and Botney Cut 2004 (CBBC'04) sea trial is located in the North Sea, close to the Cleaver Bank and Botney Cut, north-west of the Netherlands as documented in Fig. 3.10. The area is of interest due to its variability in sediment types, which was already indicated in Ref. [34].

3.2.1 Equipment and measurements

A dense pattern of east-west tracks was sailed during the measurements in 2004, while taking hydrographic measurements. Both SBES and MBES data are available.

The SBES measurements considered here were taken by a 38 kHz Kongsberg EA600 SBES system, similar to the one employed in the MREA/BP'07 experiment. This 38-kHz echosounder has a beamwidth of 9.6° and a pulse length of $256 \mu\text{s}$. Ping rates typically are 5 Hz. The individual SBES returns indicate a clear ping-to-ping variability, which is due to the stochastic nature of the backscatter process, motions of the ship, and presence of bottom features. To constrain these effects at least partly and to capture the effects of the seafloor type on the acoustic signals instead, a series of sequential pings is averaged. Here, the averaging was carried out over 50 sequential pings, which cover a distance of approximately 50 m. This value was chosen as a compromise between the aim to average out the above described effects and still keeping an acceptable spatial resolution.

The MBES employed is also similar to the one used during the MREA/BP'07 experiment, a 300 kHz Kongsberg EM3000D dual-head with an aperture of 1.5° for each of the 254 beams. These data have been analyzed in [8] and are not presented in this thesis.

During the 2004 trial, no grab samples have been collected. We thus have to rely on samples of former experiments.

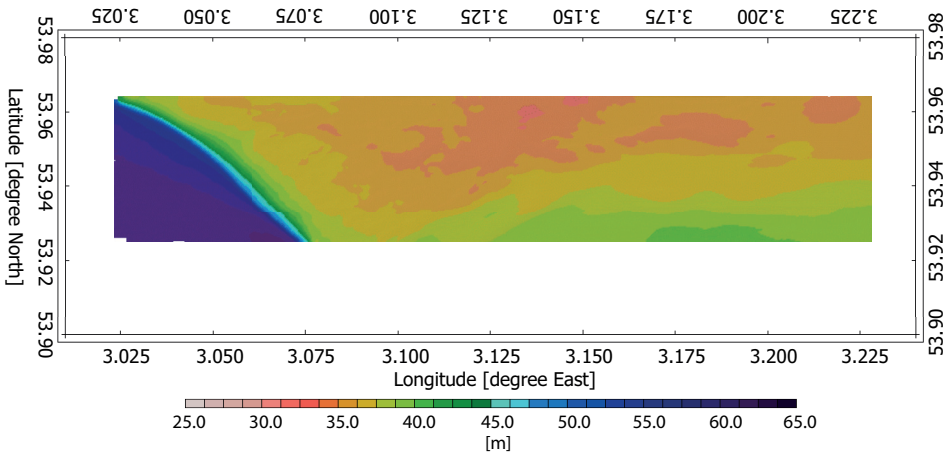


Figure 3.11: Water depth in the CBBC'04 trial area.

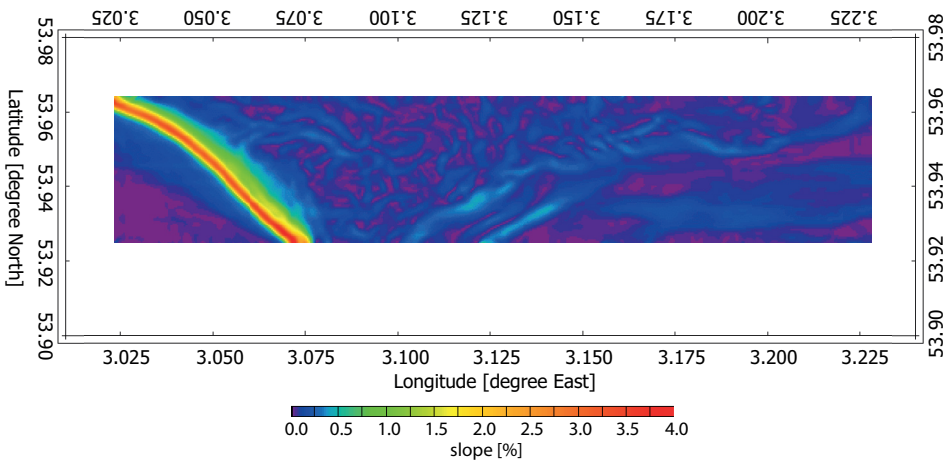


Figure 3.12: Slope in the CBBC'04 trial area.

3.2.2 Bathymetry

Water depths in the area vary between 30 m and 60 m as illustrated in Fig. 3.11. The shallow eastern part forms the Cleaver Bank. Here, variation in depth is rather small. This is confirmed by the map of the bathymetric slope in Fig. 3.12. Slope values at the Cleaver Bank do not exceed 0.5%. However, from the slope map, two regions with distinct slope patterns are evident in this shallow part. While the south-eastern part of the Cleaver Bank shows only moderate changes in slope, the north-western part of the Cleaver Bank is characterized by inhomogeneous, curled structures. Further to the west, the sea bottom rather abruptly drops more than 10 m and forms a 60 m deep trench, the Botney Cut. This harsh intersection comes along with slope values increased to 4%. The Botney Cut itself features the smallest slope values, with less than 0.25%.

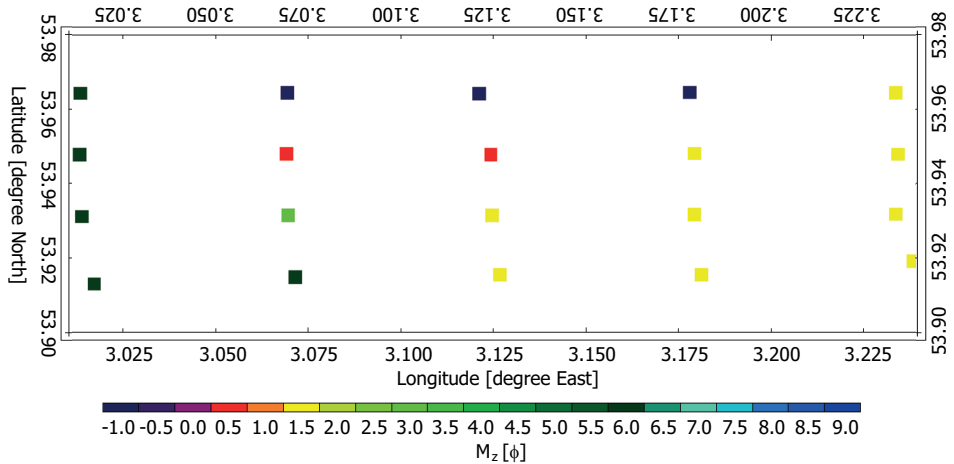


Figure 3.13: Grain sizes in the CBBC'04 trial area.

3.2.3 Properties of the sea bottom

Information about the sediment composition is available from an earlier sea trial in November 2000. During this trial, a series of 20 bottom grabs was taken in the area under investigation. An overview of the Folk classes in the trial area is given in Fig. 3.13. The softest sediments, such as silt and clay, occur in the deeper Botney Cut. The shallow Cleaver Bank, on the other hand, is composed of various types of sand. In the north-western part of this plateau, additionally gravel fractions are present.

Classification of SBES data

Currently, almost any modern vessel is equipped with an echosounder. Among these, single-beam echosounders (SBESs) are widespread. However, they provide only an insight into a small part of the seafloor, namely that part which actually falls under their footprint. Still, each single acoustic signal contains information about the sea bottom with which it interacted. The objective of this chapter is to investigate SBES signals in order to assess their discriminating properties for different sediment types. For this purpose, either the full received SBES echo or parameters that describe the shape of this echo can be employed, since they represent deformations in the signal which are due to the interaction with the sea bottom sediments. Existing approaches for coupling the signal information to sediment parameters [10–13, 15, 16, 35] can be grouped in phenomenological and model-based approaches. Phenomenological approaches give an acoustic classification of the environment based on signal parameters. The resulting classes are then linked to sediment types by a comparison with ground truth data, for example bottom grab samples. Model-based approaches, on the other hand, fit a physical description of either the full echo shape or its descriptive parameters to the measurements and thus couple the signal information directly to sediment parameters. Both types of approaches are explored in the following, after a description of the SBES signal is given.

4.1 The SBES echo and its parameters

SBES transducers transmit acoustic pulses toward the sea bottom, which are received back at the transducer after the signal has interacted with the sea bottom (see Ch. 2.1). On their way from the source to the receiver, these signals expand and experience different kinds of losses, which have to be corrected for. The corrections described in the following are standardly applied to underwater acoustic signals.

While traveling, the signal intensity decreases due to geometrical spreading and absorption. Geometrical spreading, or transmission loss, affects the signal on both the way down

This chapter is based on the following publications, with minor changes.

K. Siemes, M. Snellen, A.R. Amiri-Simkooei, D.G. Simons, and J.-P. Hermand: "Predicting spatial variability of sediment properties from hydrographic data for geo-acoustic inversion," *IEEE J. Ocean. Eng.*, 35(4), 2010. [DOI:10.1109/JOE.2010.2066711] ©2010 IEEE. Parts are reprinted, with permission.

M. Snellen, K. Siemes, and D. G. Simons: "Model-based sediment classification using single-beam echo sounder signals," *J. Acoust. Soc. Am.*, 129(5), 2011. [DOI:10.1121/1.3569718] ©2011 Acoustical Society of America. Parts are reprinted, with permission.

M. Snellen, K. Siemes and D.G. Simons: "On the practical applicability of single-beam model-based seafloor classification," in *Proceedings of the European Conference on Underwater Acoustics (ECUA)*, Istanbul, 2010.

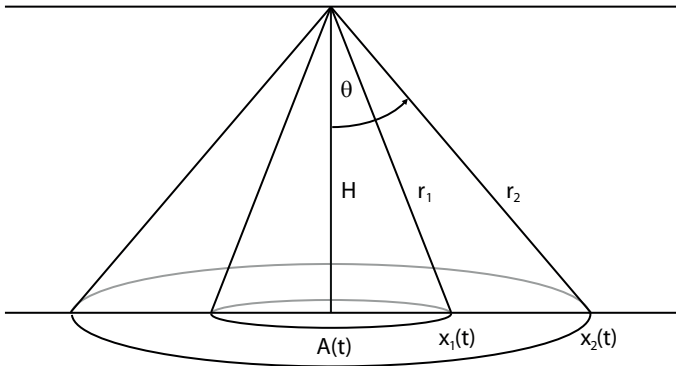


Figure 4.1: Schematic of the SBES footprint. With increasing time t , the area A increases circularly, before it decreases again out of its center and becomes a disk. The points $x_1(t)$ and $x_2(t)$ describe the inner and outer boundary of this disk.

to the seafloor and on its way back to the receiver. The received signal further depends on the footprint A , thus the area of the seafloor contributing to the response, which is dependent on the angle ϕ under which the signal is sent, on the time t , and additionally on the water depth and slope. For a constant water depth and slope, the footprint dependence on the ϕ is schematized in Fig. 4.1. At the receiver, the signal is affected by the sensitivity of the sensor, which can be expressed in a directional response function. Point sources are omnidirectional but less sensitive to a special direction, whereas larger sensors are more sensitive to a specific direction.

In the following, the SBES signals are treated as being fully corrected. Due to the scattering properties of the seafloor¹, the basic shape of an SBES signal is the same for all seafloor types. It features a strong first peak, formed by the sound that has been traveling on the direct path, and a tail, formed by the sound that has been scattered and will therefore arrive later. Variations in the roughness and hardness of the seafloor, however, can cause delays in the arrival time of either parts of the signal. The actual shape of the received echo, therefore, depends on the sediment composition. Figure 4.2 gives an overview of typical SBES signals for different types of seafloor sediments.

Several features of the received signal, such as total energy, time spread, and skewness, contain information on the sea bottom composition and can potentially be used as parameters in seafloor classification [35]. These features are conceptually similar to the first, second, and third statistical moments. The echo energy E depends on the signal intensity $I(t)$ and, therefore, the sound pressure p .

$$E = \int_0^{T_0} I(t) dt \quad (4.1)$$

The time spread T is defined as

$$T = \sqrt{\frac{4}{E} \int_0^{T_0} I(t)(t - t_0)^2 dt} \quad (4.2)$$

¹At the seafloor the signal is scattered and/or reflected. Reflection- and scatter theory is treated in App. C.

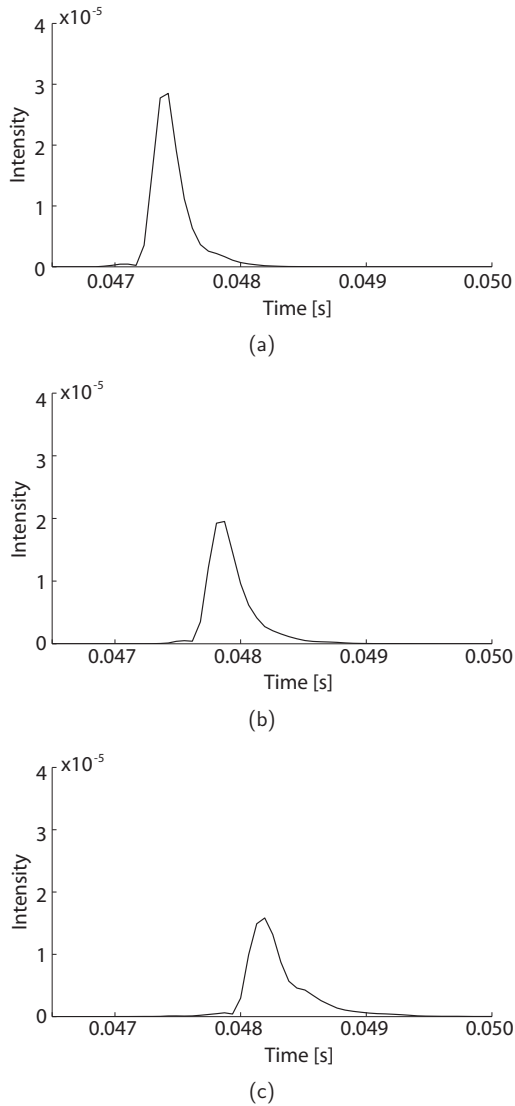


Figure 4.2: Typical SBES signals for three different sediment types: (a) sandy gravel ($M_z = -1$), (b) muddy sand ($M_z = 3$), and (c) sandy clay ($M_z = 7$).

and includes information about the temporal extent of the echo. Here, t_0 is the echo center of gravity. Further, the echo's asymmetry is described by the skewness S , defined by

$$S = \frac{8}{T^3 E} \int_0^{T_0} I(t)(t - t_0)^3 dt. \quad (4.3)$$

Both, T and S have been normalized such that their correlation is reduced. The typical form of the SBES echo with its tail following the main peak results in S being positive for all sediment types.

4.2 Phenomenological classification by echo shape parameters

4.2.1 Principal component analysis (PCA) and clustering

Although the (normalized) echo shape features, introduced in Ch. 4.1, are intrinsically different in nature, they are statistically correlated. The PCA is adopted according to [36] to reduce the dimensionality of the extracted features, while retaining most of the variation of the features. PCA transforms a number of different but possibly correlated variables via linear combination into a smaller number of uncorrelated variables, called principal components, by means of an eigenvalue decomposition of the parameter covariance matrix. The first few principal components account for as much of the variability in the data as possible. They are then fed to a cluster analysis based on the well-known k -means clustering algorithm [37]. In the following, we give a brief summary of these concepts as they are applied to an underwater acoustics case in a colleague's paper [38].

In general, measured parameters are collected in a $n \times m$ matrix Y , consisting of n measurements of the m parameters. For the current application, these parameters represent the measured features E , T , and S , extracted from the acoustic signals. These measurements are normalized in such a way that for each feature, the mean parameter value has been subtracted and the resulting values are divided by its standard deviation. Each of the columns of Y thus has zero mean and unit variance. The covariance matrix of Y is then defined as

$$\Sigma = \frac{Y'Y}{n-1}. \quad (4.4)$$

The eigenvalue decomposition of Σ is given as

$$\Sigma = U\Omega U' \quad (4.5)$$

with U containing the eigenvectors, columnwise, and Ω containing the related eigenvalues in its diagonal and zeros elsewhere. The eigen vectors are sorted such that the first one represents the direction of maximal variation in the data and the following each represent directions with decreasing variation.

A product of the i -th column of U with the data matrix Y , which is a linear combination of the three signal features, represents the i -th principal component.

The principal components are statistically uncorrelated. They represent the directions in which the maximum variation occurs, except for the higher order principal components. Often, only the high-order principal components are selected as members of the new parameter set, neglecting those directions which only show slight variation.

In order to distribute the selected principal components over k classes, a number which has to be predefined, the parameter space is divided into clusters. This is achieved by employing the k -means clustering method. It starts with k initial centroids around which the clusters are formed. In the following, these initial centroids are randomly selected and each point, representing a measured parameter value combination, is assigned to its nearest centroid, in terms of Euclidean distance. In an iterative process of assigning the cluster members and updating the centroid positions, the sum of the distances between the assigned points and their related centroids is minimized.

4.2.2 Application of the PCA to the MREA/BP'07 data

A well-described application of the PCA to SBES signal features in the CBBC'04 area can be found in [39]. Here, the PCA has been applied to the MREA/BP'07 SBES data. For the current application we focus on the features energy E , time spread T , and skewness S , extracted from the SBES signals. In three independent classifications, data from the frequencies 12 kHz, 38 kHz, and 200 kHz are considered. Of special interest are the data taken at the frequency of 200 kHz since this frequency has a similar magnitude as the one of the MBES (300 kHz). Therefore, both datasets can be used for mutual validation (Ch. 8.1).

The intensities of the received signals have been corrected for spherical spreading and footprint effects. Another depth-dependent correction scales the echoes in time in relation to a given reference depth. This correction compresses signals that are obtained at a depth greater than the reference depth and elongates signals from a depth smaller than the reference depth.

After the three signal features E , T , and S have been extracted from the recorded signals, they have been normalized such that each echo feature has a zero mean and unit variance. For each extracted feature the noise level has been reduced by averaging over 40 consecutive pings. All three resulting parameters show correlations, as displayed in Tables 4.1-4.3. Especially, the energy and time spread are highly correlated, except for the 38 kHz data.

Table 4.1: Correlation between the SBES signal parameters at 12 kHz

	Energy	Time spread	Skewness
Energy	1.0000	-0.3913	-0.1622
Time spread	-0.3913	1.0000	0.0446
Skewness	-0.1622	0.0446	1.0000

Table 4.2: Correlation between the SBES signal parameters at 38 kHz

	Energy	Time spread	Skewness
Energy	1.0000	0.3657	-0.7815
Time spread	0.3657	1.0000	-0.3700
Skewness	-0.7815	-0.3700	1.0000

Table 4.3: Correlation between the SBES signal parameters at 200 kHz

	Energy	Time spread	Skewness
Energy	1.0000	-0.7121	-0.5511
Time spread	-0.7121	1.0000	0.2757
Skewness	-0.5511	0.2757	1.0000

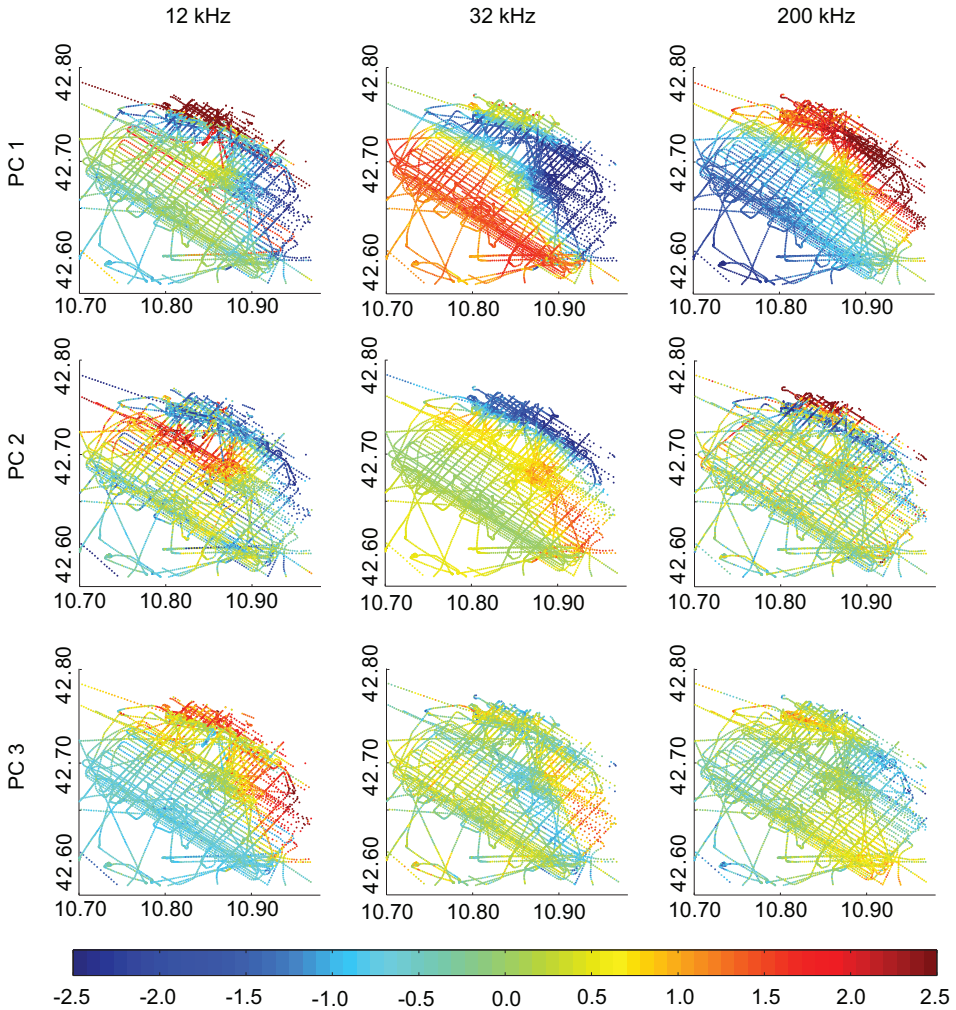


Figure 4.3: Maps of the three principal components (rows) at the frequencies 12, 38, and 200 kHz (columns).

The PCA has been applied to assess the three signal feature combinations that contain the relevant information for discriminating between different bottom types for each frequency. The principal components are given in Fig. 4.3. For each frequency, two out of the three principal components, which contain most of the variability of the data, are used for cluster analysis. The results obtained at the different frequencies are as follows.

12 kHz: The first and second principal component account for approximately 48% and 32% of the variability of the data, respectively. The first principal component is influenced by all parameters, however less by the skewness. The skewness, on the other hand, dominates the second component.

38 kHz: The first and second principal component account for approximately 68% and 25% of the variability of the data, respectively. All features contribute to both components.

The timespread, however, appears to be stronger in the second component and weaker in the first component.

200 kHz: The first and second principal component account for approximately 68% and 25% of the variability of the data, respectively. The first principal component is again influenced by all three features, which are in decreasing order: energy, time spread, and skewness. The second principal component, on the other hand, is dominated by the skewness and time spread.

Based on the inspection of the first two principal components, the number of clusters with similar acoustic properties was set to four for each frequency. The resulting classification maps are given in Figs. 4.4–4.6.

For all frequencies a similar map of the acoustic classes is obtained. Largest variations among these results occur in the center part of the area. These variations might be explained by the different penetration depth of the different frequencies and the presence of slightly different material at these depths. In a first instance, the so found classes are related to neither an acoustic or sediment property and require ground truth data for interpretation. This is given by the sediment samples, provided in Ch. 3.1.3. The arrangement of the four classes tends to represent variations which are also visible in the sediment distribution. A comparison to other data sets will be provided in Ch. 8.1.

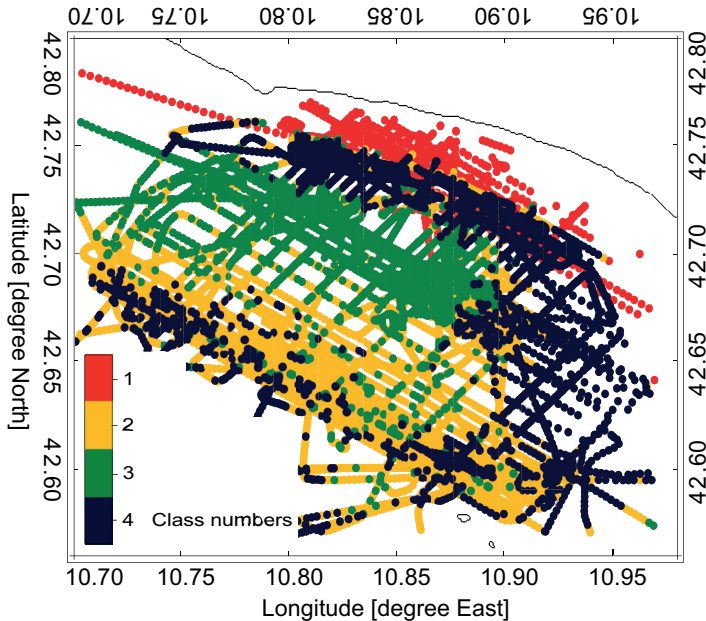


Figure 4.4: Classification results of the PCA and clustering based on SBES signal features (energy, time-spread, and skewness) at 12 kHz.

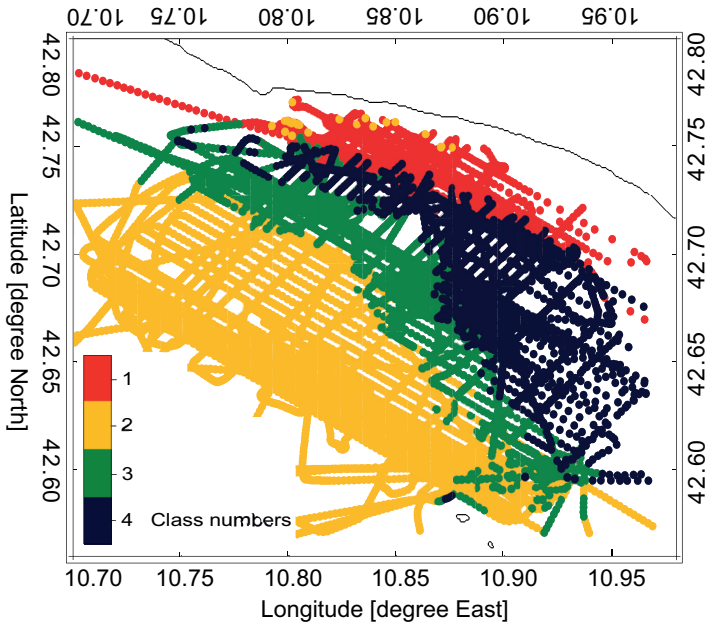


Figure 4.5: Classification results of the PCA and clustering based on SBES signal features (energy, time-spread, and skewness) at 38 kHz.

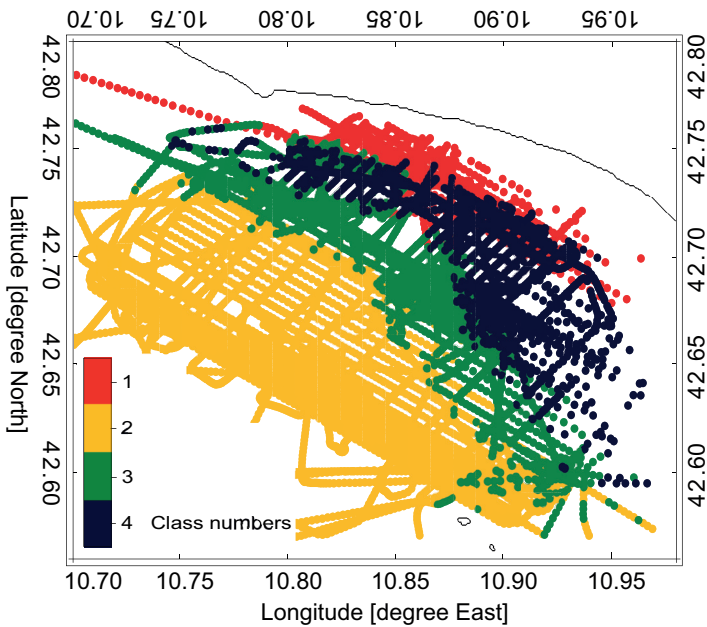


Figure 4.6: Classification results of the PCA and clustering based on SBES signal features (energy, time-spread, and skewness) at 200 kHz.

4.3 Model-based classification using the full echo envelope

Instead of using ground truth data to infer an environmental interpretation from the SBES measurements, environmental parameters can also be inverted from the measured signals. This requires a sophisticated model of the acoustic behavior of the SBES signal for a large range of environments. We follow the approach of predicting the full SBES echo envelope that was proposed by [13] and which is further described in [14]. The received echoes are modeled as being the result of scattering at the rough sediment interface and at inhomogeneities in the sediment volume. The complexity of the medium accounted for comes at the price of a series of unknowns, requiring efficient optimization methods. Three sediment parameters are searched for, being the sediment mean grain size, the surface roughness, expressed as the spectral strength, and the volume scattering parameter.

4.3.1 Method

The approach taken for the classification is schematized in Fig. 4.7. Following [13], use is made of a physical model that predicts the SBES signal return. An optimization algorithm is employed that searches for those input parameters that maximize the agreement between measured and predicted signal. As a measure of the agreement between modeled echo signal and measured echo signal, a cost function C is evaluated at each iterative step of the optimization process. Here, the following cost function is used.

$$C = \frac{\sum_k [y_{meas}(t_k) - y_{mod}(t_k)]^2}{\sum_k [y_{meas}^2(t_k) + y_{mod}^2(t_k)]}, \quad (4.6)$$

with y_{meas} and y_{mod} denoting the measured and modeled echo envelope, respectively. Further, k is the number of time samples considered, with t_k being the corresponding time.

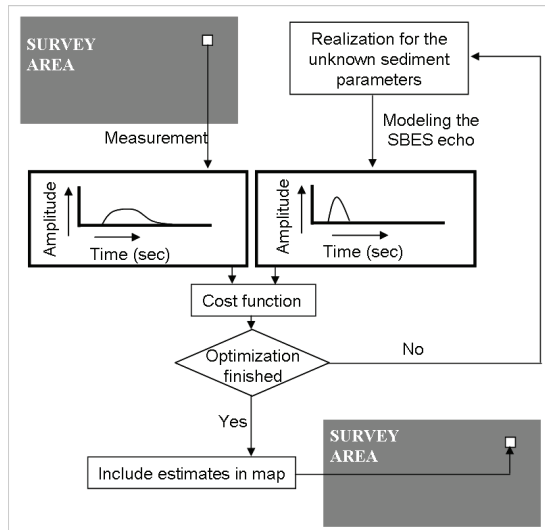


Figure 4.7: Schematic of the SBES classification approach based on echo envelope modeling.

To obtain an overview of the sediment properties over large areas, large numbers of pings need to be inverted. This requires the use of a very efficient optimization method for minimizing C . Here, we have chosen Differential Evolution (DE), as described in Appendix E.

Further, an appropriate model for predicting the received echo envelope needs to be chosen. Here, we follow [40] as described in the following.

For the envelope of the received SBES signal we can write

$$y(t) = \int_{A(t)} \sigma_b(\theta) B(\theta) \frac{e^{-4\alpha r}}{r^4} S_A(r) dA, \quad (4.7)$$

with $A(t)$ the instantaneously ensonified area that contributes to the sound received at time t and $\sigma_b(\theta)$ the backscattering cross section at the angle of incidence θ , which in turn depends on t . $B(\theta)$ is the transmit/receive directivity pattern of the transducer and $S_A(r)$ is the shape of the emitted signal, projected on the footprint to account for the variation of the signal amplitude over the footprint. It depends on the slant range $r = \sqrt{x^2 + H^2}$, with x the horizontal distance towards the receiver and H the water depth. A schematic is given in Fig. 4.1. The signal further is corrected for the absorption α in the water column.

Equation 4.7 can be expanded as follows.

$$y(t) = \int_{x=x_1(t)}^{x_2(t)} \sigma_b \left(\tan^{-1} \left(\frac{x}{H} \right) \right) \times \\ B \left(\tan^{-1} \left(\frac{x}{H} \right) \right) \frac{e^{-4\alpha r}}{r^4} S_A \left(\frac{2}{c} (r_2 - r) \right) 2\pi x dx \quad (4.8)$$

Here, x_1 and x_2 denote the two x-values that bound $A(t) = \pi(x_2^2 - x_1^2)$, and $r_2 = \sqrt{x_2^2 + H^2}$ is the slant range at x_2 . We have the upper bound

$$x_2(t) = \sqrt{\frac{c^2 t^2}{4} - H^2}, \quad (4.9)$$

with c being the speed of sound in the water, which is assumed to be constant. The lower bound x_1 is dependent on t according to

$$x_1(t) = \begin{cases} 0 & \text{for } t \leq t_0 + T_p; \\ \sqrt{\left(\frac{ct}{2} - \frac{cT_p}{2} \right)^2 - H^2} & \text{for } t > t_0 + T_p, \end{cases}$$

with $t_0 = \frac{2H}{c}$ and T_p the pulse duration.

In general, the transducer characteristics, such as the beam pattern, the signal length, and its shape, are known. This also holds for the data considered here. The water depth can be derived from the measured two-way travel time and the water column sound speed. Consequently, the only unknown in Eq. 4.8 is the backscattering cross section $\sigma_b(\theta)$. In literature, several expressions for $\sigma_b(\theta)$ are discussed.[14, 40, 41] These expressions differ in the level of detail accounted for describing the interaction between sound and sediment.

Here, we have considered the considerably detailed and well-established backscattering cross section as presented in [40], where both the backscatter cross section due to interface roughness scattering σ_r and the one due to volume scattering σ_v are accounted for. Expressed in decibel the backscatter cross section reads

$$\sigma_b(\theta) = 10 \log_{10}(\sigma_r(\theta) + \sigma_v(\theta)). \quad (4.10)$$

Both components are further described in App. C.

The sediment parameters that affect the backscatter cross section are: the mean grain size M_z , the sediment–water ratios of the mass density ρ and of the sound speed ν , the ratio of the imaginary and real part of the wave number δ , the ratio of the sediment volume scattering cross section to attenuation coefficient σ_2 (also referred to as volume scattering parameter), the exponent of the bottom relief spectrum γ , and the strength of the bottom relief spectrum w_2 (or spectral strength). In [40], a value of 3.25 for the exponent of γ is found to work well for many types of sediments. Further, empirical expressions are provided in [40] that relate the remaining parameters to mean grain size (here, expressed in ϕ units as described in Appendix A). These relations are valid for mean grain sizes in the range of -1ϕ to 9ϕ . For this range, the derived empirical parameter values of the above mentioned parameters are listed in Table C.2 of App. C. Employing these empirical expressions, thus, can theoretically reduce the search to a single parameter only. However, the spectral strength w_2 and the volume scattering parameter σ_2 are known to possibly deviate significantly from default values obtained from expressions relating them to M_z and are, therefore, included in the search. To assess the need to indeed account for all three unknowns, we also present inversions where only the mean grain size is optimized and the empirical expressions are used to assign values to the spectral strength and volume scattering parameter, based on the mean grain size.

Based on a synthetic study [42] and preliminary inversions, DE settings were selected such that 2400 forward calculations were applied.

4.3.2 Application of the echoshape model to the CBBC'04 data

In total, about 16000 averaged SBES pings have been inverted, covering the entire CBBC'04 trial area. The parameters inverted for are the mean grain size M_z , the spectral strength w_2 , and the volume scattering parameter σ_2 . The resulting estimates for mean grain size are shown in Fig. 4.8. In addition, mean grain sizes as determined from the Folk classes of the grab samples are included in the plot.

The spatial behavior indicated by the Folk classes, showing coarser sediments in the center part of the area, is in agreement with that of the inverted mean grain size. For the 60-m deep trench in the south-western part of the area, inverted M_z values indicate the presence of fine sediments ($\geq 4 \phi$). This is expected due to the, in general, lower currents in the deeper area and is in agreement with the M_z values obtained from the grab samples. In the remainder of the area, both sets of M_z values are lower, indicating coarser sediments. Here, however, they agree to a lesser extent. Whereas, the grab samples indicate only a minor variation in composition for the south-eastern area, resulting in the same mean grain size of typically 1.5ϕ , the inversions reveal consistent regions with different mean grain size values, showing variations of about 4ϕ . The ability to identify these structures from the grab samples is at least partly hampered by the small number of grab samples.

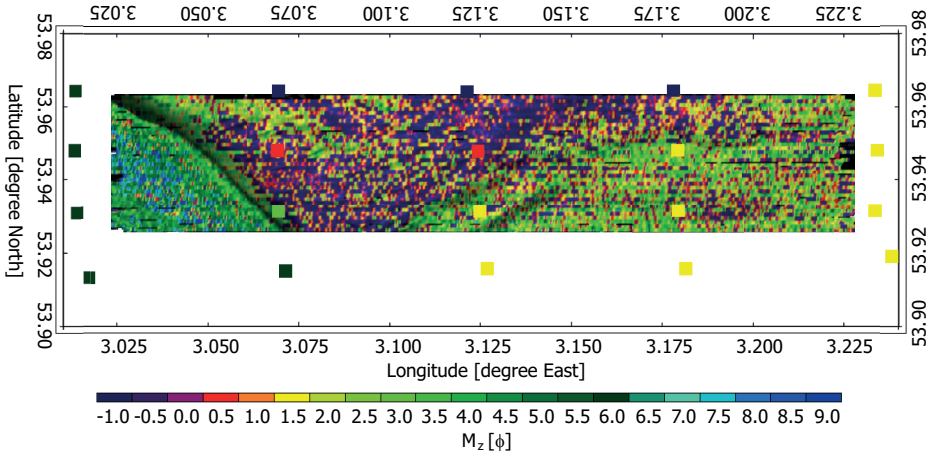


Figure 4.8: Map of inverted mean grain size. Also shown is the measured mean grain size as obtained from the grab samples as the colored squares. For the grab samples the Folk classes are displayed, which are related to M_z according to empirical relations given in [40].

A more detailed comparison, for example, aiming at establishing a relation between estimated M_z and all other parameters of the samples (shell percentage; gravel percentage; and values for the 10%, 50%, and 90% threshold for grain sizes) is not feasible due to the limited number of grab samples. In addition, the grab samples are located not exactly along the acoustic tracks. Distances between grab samples and acoustic samples are at least 50 m, whereas the acoustic classification indicates variability on typically these scales.

Figures 4.9 and 4.10 present the estimates for the spectral strength and the volume scattering parameter, respectively. In general, these two estimated parameters reveal a similar spatial pattern as M_z , dividing the area into three distinct regions. In Fig. 4.9, clear lines are visible in the eastern part. In [16], it is hypothesized that these lines are caused by fishing gear dragged over the seafloor. As can be observed from the inversion results, these plough marks affect the spectral strength, but not the mean grain size and volume scattering parameter. Figure 4.10 indicates higher values for the volume scattering parameter for clay ($0 < \sigma_2 < 0.0075$) than for fine sand ($0.005 < \sigma_2 < 0.0175$). As expected from [40], the highest values are found for the coarsest sediments that include gravel ($\sigma_2 > 0.00175$).

For w_2 and σ_2 , no independent measurements are available for validation purposes. In order to assess the sensitivity of the inversion to these two parameters, we have also carried out inversions where only M_z is estimated and empirical relations (see Table C.2 in App. C) are employed that express the spectral strength and volume scattering parameter as a function of mean grain size. The results are presented in Fig. 4.11. Comparing these to the results in Fig. 4.8, where M_z is determined from the inversion of all three parameters, it can be seen that both figures indicate the same distribution of the coarse and fine sediments. Inverting for M_z only, however, features higher M_z estimates, thus finer sediment grains, resulting in a decreased correspondence with the mean grain size estimates from the grab samples. In contrast, correspondence is somewhat enhanced in

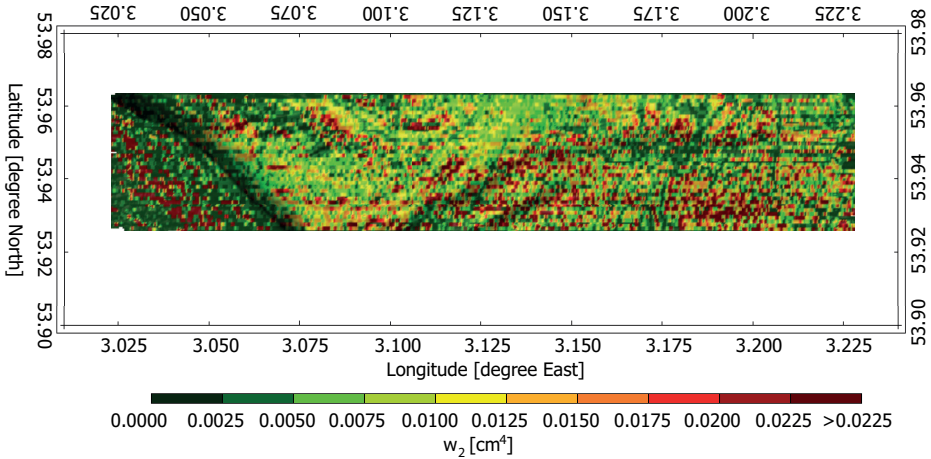


Figure 4.9: Map of the inverted spectral strength w_2 .

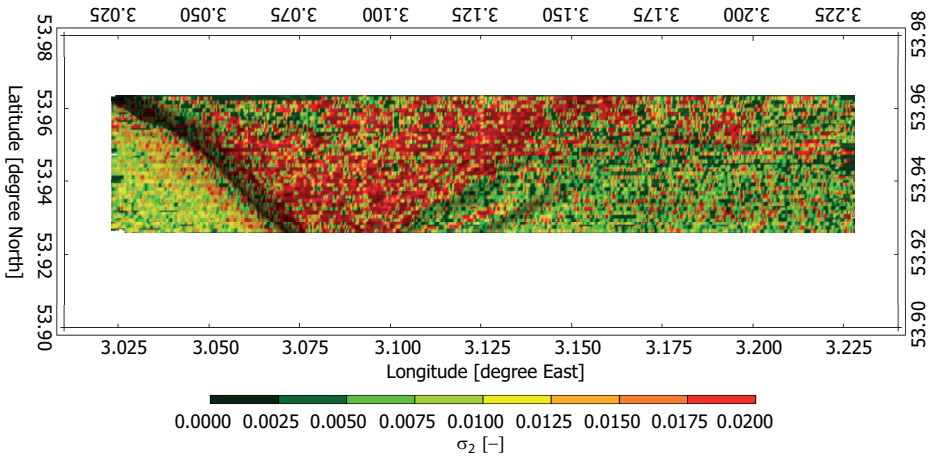


Figure 4.10: Map of the inverted volume scattering parameter σ_2 .

the center part of the coarse grained area. Furthermore, the presence of plough marks is now revealed in the map as lines with lower M_z values.

The parameters w_2 and σ_2 are known to often deviate significantly from the values as predicted by the empirical relations. For the results shown in Fig. 4.11, the deviation of w_2 and σ_2 from the empirical expressions contributes to mean grain sizes that differ from their real values. By not relying on the empirical relations, more realistic values for M_z will consequently be obtained and, therefore, Fig. 4.8 should represent the reality better than Fig. 4.11. Furthermore, the obtained estimates for the spectral strength and volume scattering parameter provide additional information about the sediment characteristics.

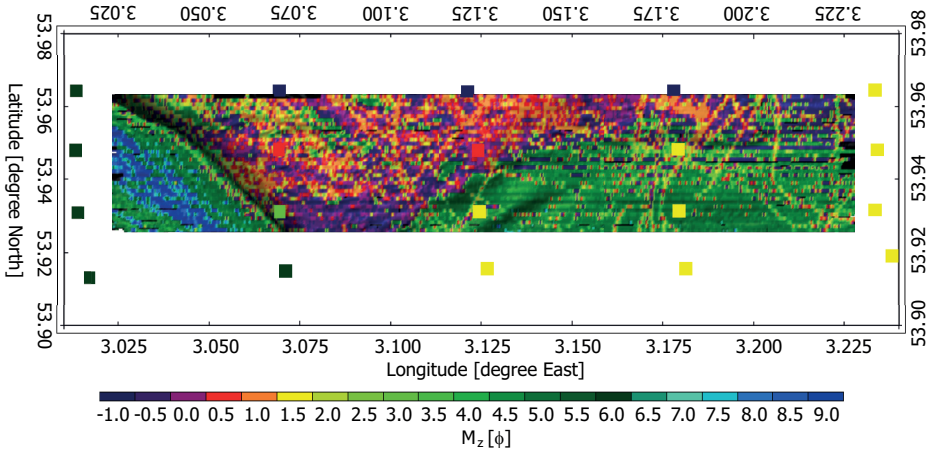


Figure 4.11: Map of the mean grain size obtained from optimization where only M_z is searched for.

Computation times, however, are significant for the three-parameter model. Using a standard personal computer and MATLAB as the programming language, inverting a single averaged ping requires several minutes computation time. Despite this effort for the three-parameter model, off-line mapping is feasible as shown by Figs. 4.8-4.10. Beside its possibility of classifying and mapping sea bottom sediments, this approach can also contribute to a gain of insight into the scattering process, when applied to a large number of different data sets. This would, consequently, allow for improving the modeling capabilities.

4.3.3 Applicability of the echoshape model to an environment with soft sediments

For fine grained sediments, such as present in the MREA/BP'07 area, volume scattering is known to dominate roughness scattering. A complex model accounting for volume scattering is therefore recommendable. However, available models, such as the one presented here, are commonly designed for standard grain sizes in the range of -1ϕ to 9ϕ . Extensions of these models are thus needed.

In a first attempt, the empirical parameter values given in Table C.2 have been extrapolated for grain sizes up to 12ϕ . However, these parameters show only slight variations among these fine grains (see Fig. 4.12). This is also reflected in the inversions employing these extrapolated values (not shown here), which are found to be unable to distinguish between the small grain sizes. Furthermore, too small M_z -values are assigned to the fine grained sediments and too large M_z -values are assigned to the less fine grained sediments. These differences, however, are likely to results from the presence of gas, as evident from the seismic profiles provided in Ch. 3.1.3. Further investigation is needed both for finding more suitable empirical values for fine grained sediments and for modeling the presence of gas.

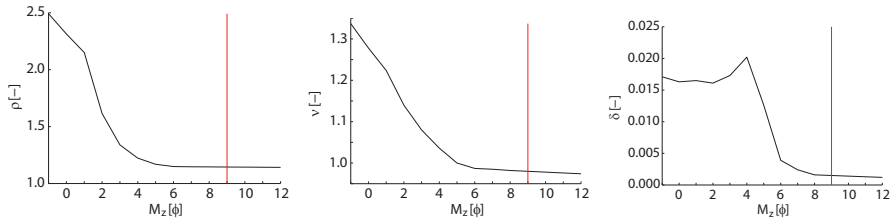


Figure 4.12: Empirical values from left to right of the ratios of density, sound speed, and wave number, as displayed in Table C.2 and extrapolated for grain sizes $> 9 \phi$.

4.4 Model-based classification using the echo energy

Since the inversion of the full echo envelope is time consuming, inverting only part of the echo or its descriptive parameters (see Ch. 4.1) becomes highly attractive. Such an approach is proposed by [16], coupling the echo energy to the reflection coefficient and modeling the latter dependent on mean grain size. We further investigate this approach for its practical applicability.

4.4.1 Method

From existing phenomenological classification approaches, it is well known that the energy of the received signal allows for discriminating sediment types.[15, 35] This knowledge is fully exploited in [16], where the received echo energy is assumed to be directly proportional to the square of the amplitude reflection coefficient at normal incidence. Empirical relations then relate the reflection coefficient to mean grain size.

Assuming that all received energy is the result of a reflection at the water–sediment interface, the amplitude reflection coefficient can be determined from the SBES echo energy as

$$R = \frac{1}{\sqrt{E_{TX}}} \frac{2H\sqrt{E_{RX}}}{e^{-2\alpha H}}, \quad (4.11)$$

with R the amplitude reflection coefficient, H the water depth, E_{TX} the energy of the transmitted pulse, E_{RX} the energy of the received pulse, and α the absorption coefficient in the water.

Based on the empirical relations in [40], the relation between M_z and the reflection coefficient, R , is calculated based on the sediment–water ratio of mass density, ρ , and the sediment–water ratio of sound speed, ν , under the assumption of normal incidence.

$$R(M_z) = \frac{\rho(M_z) \cdot \nu(M_z) - 1}{\rho(M_z) \cdot \nu(M_z) + 1} \quad (4.12)$$

The resulting reflection coefficient is presented in Fig. 4.13. Whereas Eq. 4.12 potentially allows for estimating the mean grain size from the received signal energy, Fig. 4.13 illustrates that R is not sensitive to mean grain sizes larger than 5.5ϕ .

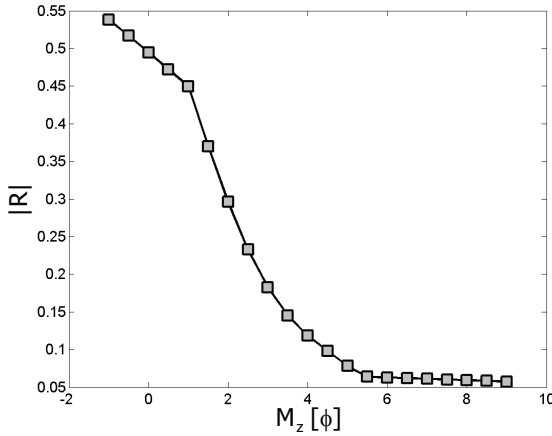


Figure 4.13: Theoretical relation between sediment mean grain size and reflection coefficient, obtained from Eq. 4.12.

4.4.2 Application of the echo energy model to the CBBC'04 area

The data considered are averaged in the same way as for the inversions employing the full echo envelope (Sec. 4.3). Figure 4.14 presents the reflection coefficients estimated from these averaged signals according to Eq. 4.11. Their values lie in the range from ~ 0.05 to ~ 0.3 . According to the theoretical relation in Fig. 4.13, these values of the reflection coefficient can be related to M_z values larger than 2ϕ . However, from the analysis of the bottom grab samples and also from the inversion results for the full echo envelope, see Fig. 4.8, lower M_z values are known to occur in the area.

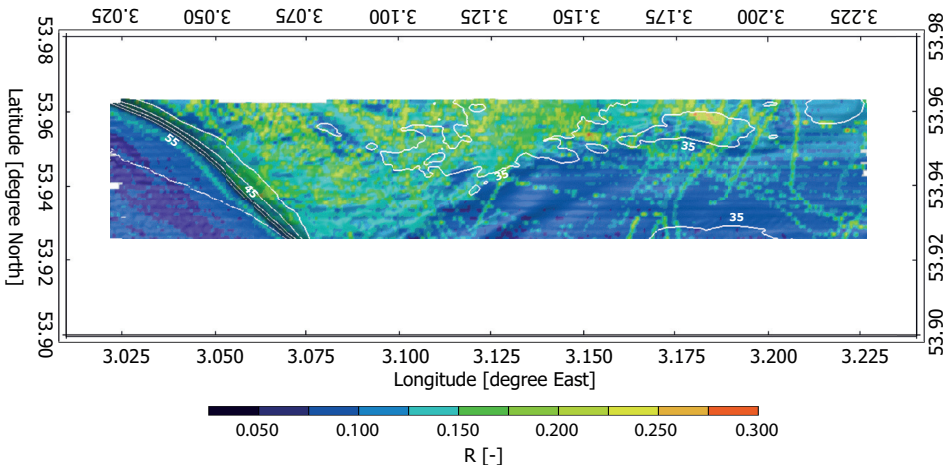


Figure 4.14: Map of the reflection coefficient as determined from the averaged SBES returns. The white lines indicate equal bathymetry contours.

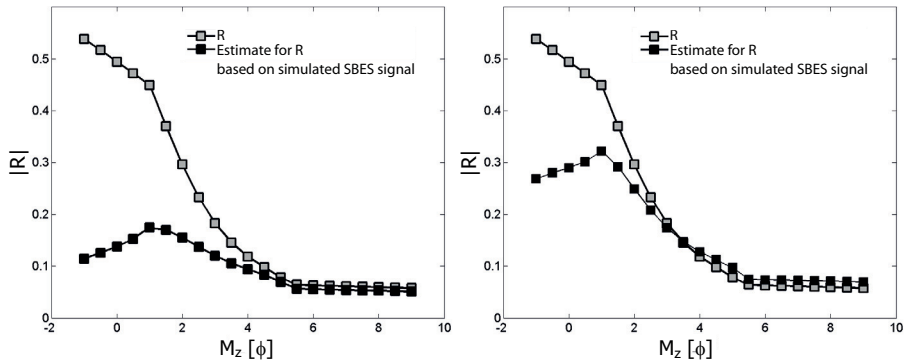


Figure 4.15: Theoretical relation between the mean grain size and the reflection coefficient, one reproduced from Fig. 4.13 (gray squares) indicating the Rayleigh reflection coefficient and the other obtained from the energy of the simulated SBES signals (black squares) for SBESs with a beamwidth of 9.6° (left) and 30° (right).

To investigate possible causes of this effect, we have used Eq. 4.8 to predict the envelope of the SBES returns for a series of mean grain size values. For the grain sizes considered, all other sediment parameters of the model, including also w_2 and σ_2 , are calculated according to the empirical relations of [40], as given in Table C.2. Then, Eq. 4.11 is used to obtain an estimate for the reflection coefficient based on the echo energy. The left plot in Fig. 4.15 shows the results for an SBES with a beamwidth of 9.6° , as considered in the CBBC'04 experiment.

Clearly, the reflection coefficient estimated from the simulated signal is much lower for the coarse grains than expected. The main reason for this deviation is the limited beamwidth of the transducer, which strongly reduces the amount of sound that impinges upon the SBES at angles away from normal incidence. This also causes non-uniqueness in the conversion of energy to mean grain size, hampering the mapping of the mean grain sizes based on the reflection coefficient. Using an SBES with a larger beamwidth will reduce these effects.[43] This is demonstrated in the right plot of Fig. 4.15, where the same procedure as above is followed for an SBES with an increased beamwidth of 30° . However, the contribution of the volume scattering now results in a reflection coefficient that slightly exceeds the theoretical curve for the fine grained sediments.

Still, for the SBES with a standard beamwidth, as the 9.6° considered here, regions with different sediment types are revealed by the echo energy.

An additional effect, hampering the coupling of the detected regions of the estimated reflection coefficient to mean grain size, is the uncertainty in the spectral strength and volume scattering parameter, as shown in the following. Again, the only parameter searched for is the mean grain size, whereas all other parameters affecting the interaction of sound with the seafloor are taken according to the assumed empirical relations (Table C.2). As mentioned before, these relations are known to hold well for the sediment sound speed, density, and attenuation, but less for the spectral strength and volume scattering parameter. While, in general, these parameters are not known, here, the inversions of the full echo envelope (Ch. 4.3) have provided estimates for w_2 and σ_2 for each averaged signal, in addition to the estimates of M_z . This allows for assessing the influence of deviations in w_2 and σ_2 from their empirical values on the estimates of the reflection coefficient.

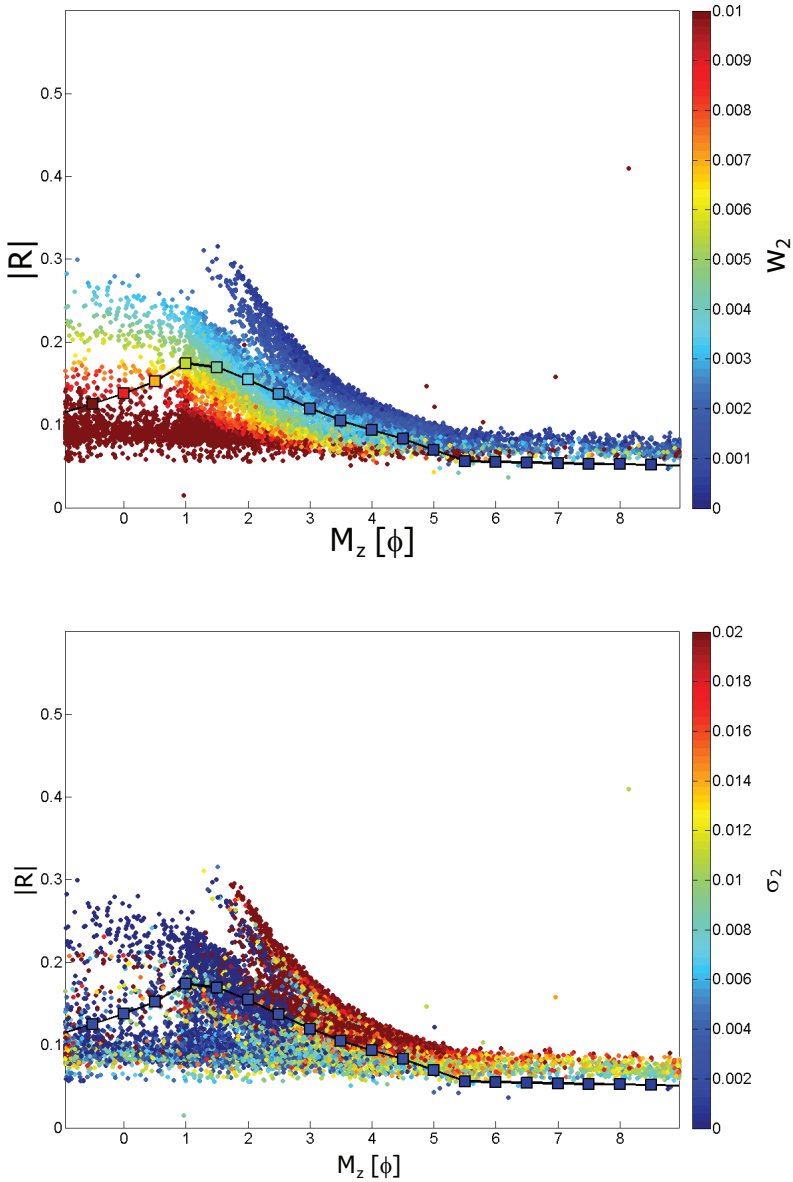


Figure 4.16: The relation between the mean grain sizes inverted from the full echo envelope and the measured reflection coefficients (dots). The color of the dots represents the inverted spectral strength. For comparison, the graph of the simulated reflection coefficient is reproduced from Fig. 4.15. Here, the color of the squares represents the empirical value of (a) the spectral strength and (b) the volume scattering parameter, respectively.

For this purpose, the measured values of the reflection coefficient are plotted in Fig. 4.16 versus the estimates of M_z obtained from the inversions using the full echo envelope (see Fig. 4.8). The theoretical relationship between R and M_z for an SBES with 9.6° beamwidth, given in Fig. 4.15, is added for comparison. In case the empirical relations between the mean grain size and the spectral strength and volume scattering parameter hold, the measured reflection coefficient versus inverted mean grain size would repeat the theoretical relation. However, the values of the R show a spread around these theoretical values, further adding to the non-uniqueness of their relation. Maximum measured values of R can be twice as large as the simulated values. An exception holds for reflection coefficients at mean grain sizes between 2ϕ and 5ϕ , where the upper bound of the reflection coefficient is more restricted (only 1.5 times of the simulated value). The lower bound of R , on the other hand, is approximately 0.05 throughout the entire range of mean grain sizes, disallowing an allocation of mean grain sizes at these small reflection coefficients.

We hypothesize that a major part of the spread is caused by deviations of the spectral strength and volume scattering parameter from their empirical values, in addition to effects of a possibly not fully converged optimization and a possible imperfectness of the model. In the upper graphic of Fig. 4.16, the spectral strength is indicated by the color, whereas the color of the lower graphic represents the volume scattering parameter. For the relation between the reflection coefficient and the inverted mean grain size, the inverted spectral strength and volume scattering parameter are displayed, respectively. For the theoretical relation, the spectral strength and volume scattering values as obtained from the empirical expressions are shown. The empirical values of the spectral strength indicate an increasing spectral strength with decreasing M_z . Despite the large spread, the same trend is visible in the estimates for the spectral strength obtained from the inversion. Considering the variation of the spectral strength per mean grain size, the upper plot of Fig. 4.16 indicates a decreasing reflection coefficient as a function of increasing spectral strength. This is expected, since increased roughness results in an increased amount of scattering away from normal incidence and, consequently, a lower signal strength received by the SBES. The spread in R can thus, at least partly, be related to a spread in w_2 . The largest deviation of the spectral strengths from their empirical values is found for coarse sediments. On the other hand, deviations in the volume scattering parameter from their empirical values (lower graphic of Fig. 4.16) mainly contribute to the softer sediments, represented by larger M_z values. At smaller M_z values, thus larger grains, the influence of volume scattering is very low, in general. The values for the volume scattering parameter, as obtained from the inversions, are higher than those predicted by the empirical relations for the higher M_z values, resulting in increased signal energies and consequently increased estimates for the reflection coefficient, compared to the theoretically expected values.

An application to the MREA/BP'07 area seems not suitable due to the prevailing grain sizes of 7ϕ to 11ϕ and the insensitivity of the reflection coefficient at this range.

4.5 Conclusions

In this chapter, we compare an empirical method and two model-based approaches of different complexity for acoustic sediment classification with SBES signals.

The empirical method is based on echo shape parameters. It uses a principal component analysis for decorrelating these parameters and k -means clustering for dividing the

so found parameter space into classes. This method allows for fast computation. However, as groundtruth is required, field work becomes more extensive. Four different classes emerged from this analysis for the MREA/BP'07 area. A comparison with grab samples shows promising results. Overall, different classes emerge at locations with different grain sizes. However, minor differences in the classification results are found for the frequencies considered. These are assumed to result from different penetration depths.

For model-based approaches, computation time mainly depends on the complexity of the model, since no independent measurements are needed. The first model-based approach bases the classification upon matching the complete echo envelope and inverting for three parameters, which are the mean grain size M_z , spectral strength w_2 , and volume scattering parameter σ_2 , whereas the second model-based approach merely considers energy from the received signal to estimate M_z only. Since their application is limited to moderate grain sizes, the model-based approaches have been investigated primarily for the CBBC'04 area.

An application of the first model-based approach to the CBBC'04 data indicates its feasibility to estimate sediment parameters for a range of different sediment types. The estimates of the mean grain size are confirmed by the distribution of Folk classes, as determined from sediment samples taken in the area. No independent measurements are available for the roughness and volume scattering parameters. However, all three maps (Figs. 4.8-4.10) reveal a similar pattern of sediment distribution, as expected from the existence of empirical expressions relating these parameters. Whereas many applications mainly require information about the sediment mean grain sizes, information regarding the roughness and volume scattering parameters are of high relevance for application such as sonar performance prediction. The search for three parameters, however, makes this approach computationally demanding. Using a standard PC and MATLAB as the programming language, real-time processing is not feasible, but on-line applications are expected to become feasible in the near future. A less computational demanding approach is to reduce the inverted parameters to M_z only. This approach was found to reveal a similar pattern for the sediment distribution. However, discrepancies between the inverted M_z values and the values of M_z from the grab samples are enlarged.

Classification based on a direct relation between echo energy and mean grain size, to eliminate the need for inversions completely, was found to be hampered by the limited beamwidth of the SBES. Coarse grained sediments were found to result in the same estimates for mean grain size as finer grained sediments. The use of an SBES system with a larger beamwidth would allow for increased discriminating performance. Still, also the variation of the volume scattering parameter and the spectral strength around their empirical values prevents the coupling between echo energy and mean grain size; the unknown spectral strength and volume scattering parameter might then result in M_z estimates that deviate from their true values.

Overall, it can be concluded that for model-based SBES classification, in practice, an approach based on the full echo envelope and accounting for M_z , w_2 , and σ_2 is recommended. However, inverting for M_z only or considering the echo energy, instead of using the full echo envelope, are approaches that are extremely useful for a first quick assessment of an area, on which for example decisions for further surveying can be based.

In all cases, the validity of the model for the prevailing grain sizes needs to be guaranteed. Most of the models currently available require extension in the field of fine and very rough grain sizes. In cases of very fine grained sediments, empirical approaches have proven to be a good alternative.

Bayesian classification of MBES data

MBES systems have proven to allow for characterization of the seafloor sediments. Many approaches deal with the classification based on MBES backscatter strength data by modeling the backscatter curves along a swath, thereby accounting for scattering at the rough water–sediment interface and volume scattering of the sediment body [44, 45]. When modeling backscatter strengths under different beam angles, the occurrence of nonuniform sediment types within a single swath has to be accounted for. In addition, the MBES needs to be well calibrated, which is not always the case [46]. Therefore, the approach towards sediment classification employing MBES backscatter strength data chosen for this paper employs the backscatter data per beam. It has been developed on the basis of a Bayesian approach as proposed by [8]. To optimize the method for the current application, characterized by water depths ranging from a few meters only to over one hundred meters, modifications to the original method were required.

For characterizing the seafloor sediments, we use the backscatter strengths derived from the intensity of the backscattered acoustic signal. The approach selected for the current research utilizes the average backscatter strength per beam. An advantage of this approach is its insensitivity to variations of seafloor type along the swath. In addition, imperfect calibration of the MBES system does not hamper the classification. The approach is presented in [8], where it is employed to a single angle of the CBBC'04 data. For the current research, it is extended, to be capable of dealing with a large range of beam angles, and is applied to the MREA/BP'07 area. Due to the relatively large distances between the tracks covered by the MBES in this area, the method is modified such that a large number of beams can be accounted for in the classification, thereby exploiting the high coverage capacity of the MBES. In addition, the MREA/BP'07 area exhibits large variations in depths. This results in more variation (over the area) in the statistical properties of the averaged beam backscatter strengths. To properly account for these variations, a further extension is required as described in the following.

This chapter is based on the following publications, with minor changes.

K. Siemes, M. Snellen, A.R. Amiri-Simkooei, D.G. Simons, and J.-P. Hermand: "Predicting spatial variability of sediment properties from hydrographic data for geo-acoustic inversion," *IEEE J. Ocean. Eng.*, 35(4), 2010. [DOI:10.1109/JOE.2010.2066711] ©2010 IEEE. Parts are reprinted, with permission.

K. Siemes, M. Snellen, D. G. Simons, J.-P. Hermand, M. Meyer, and J.-C. Le Gac: "High-frequency multi-beam echosounder classification for rapid environmental assessment," in *Proceedings of the European Conference of Underwater Acoustics (ECUA)*, Paris, 2008.

K. Siemes, M. Snellen, D. G. Simons, and J.-P. Hermand: "Using MBES backscatter strength measurements for assessing a shallow water soft sediment environment," in *Proceedings of the Oceans IEEE conference*, Bremen, 2009.

5.1 The Bayesian approach

The geoacoustic classification method that we present in this chapter is based on the Bayesian approach as applied by [8]. It assumes that the filtered backscatter value BS_θ , as provided by the MBES system at beam angle θ , is the average of N_θ backscatter strength values $BS_{\theta,n}$ obtained from $n = 1, \dots, N_\theta$ scatter pixels within the beam footprint at θ .

$$BS_\theta = \frac{1}{N_\theta} \sum_{n=1}^{N_\theta} BS_{\theta,n} \quad (5.1)$$

Theoretically, the available number of scatter pixels N_θ can be determined from the beam geometry (Fig. 5.1) as the fraction of the size of the beam footprint dA and the size of a scatter pixel da , which varies with the water depth H , the beam angle θ , and the beam opening angle θ_T , which also depends on θ .

$$\begin{aligned} N_\theta &= \frac{dA}{da} \\ &= \frac{H \cdot \theta_T}{\cos^2(\theta)} \cdot \frac{2 \sin(\theta)}{c\tau} \end{aligned} \quad (5.2)$$

The variables c and τ denote the water-column sound speed and the pulse length, respectively. While Eq. 5.2 is valid for beams away from nadir, $N_{\theta=0} = 1$ holds at nadir.

If the number of scatter pixels for averaging per beam footprint is large enough, the central limit theorem holds, resulting in BS_θ being normally distributed. When a single seafloor type is present, this allows one to fit a single Gaussian probability density function (PDF) to the histogram of observed backscatter strength at that angle. If more than one seafloor type is present, the backscatter histogram can be modeled by a sum of m scaled Gaussians, with m representing the number of seafloor types.

$$\begin{aligned} f(BS_\theta|x) &= \sum_{k=1}^m f(BS_\theta|x_k) \\ &= \sum_{k=1}^m c_k \exp\left(-\frac{(BS_\theta - \mu_k)^2}{2\sigma_k^2}\right) \end{aligned} \quad (5.3)$$

The histogram and the fitted Gaussians are depicted in Fig. 5.2. Here, for each Gaussian PDF $f(BS_\theta|x_k)$, $x_k = [c_k, \mu_k, \sigma_k]^T$ holds, with c_k the scaling factor, μ_k the mean, and σ_k the standard deviation of the k th PDF. The unknown parameter vector $x = [x_1, x_2, \dots, x_m]^T$ can be estimated using the least-squares technique. The nonlinear least squares, subject to bounds on variables as in [47], is used to obtain the μ_k s and σ_k s, and the nonnegative least squares method, see e.g. [48], is used to obtain the contributions of the individual PDFs by constraining the coefficients c_k s to be positive. For further explanation of the method and the steps involved we refer to [8].

This approach is well suited for regions with a uniform and moderate depth. However, the assumption of a normal distribution for the averaged backscatter strength does not hold, if the number of scatter pixels is small. Especially in very shallow water and at low

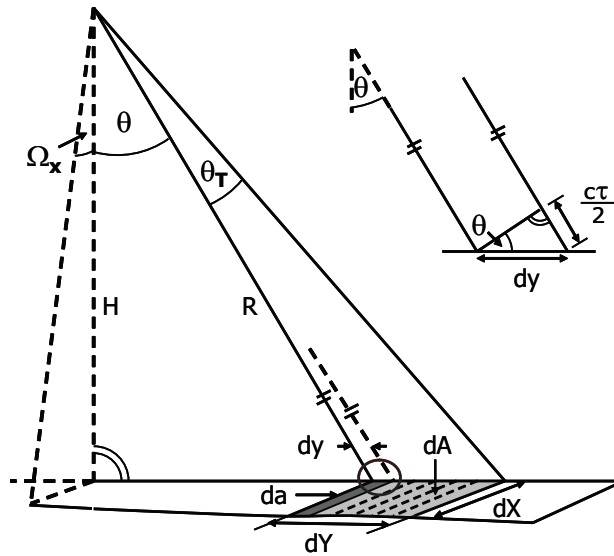


Figure 5.1: Schematic of the beam- and signal footprint of an MBES as obtained by the receiver array. The beam footprint $dA = dX \cdot dY$ and the footprint of scatter pixel $da = dX \cdot dy$ are indicated in lighter and darker gray, respectively. They depend on the beam angle θ , the beam opening angle in across-track direction θ_T (related to θ), the beam opening angle in along-track direction Ω_x and depth H (or alternatively range R). The upper right plot zooms into a single scatter pixel. Here, c is the watercolumn sound speed and τ is the pulse length.

beam angles θ , beam footprints contain too few scatter pixels. Therefore, a modification is applied to the above described classification method which involves an averaging over both beams and pings, to create regions with comparable large numbers of independent scatter pixels. The averaging over beams involves a number of $b = b(\theta)$ beams, which again depends on the beam angle. Close to nadir, a small number of scatter pixels per beam footprint demands averaging over a large number of beams. At the outer beams, where beam footprints are large, b has to be chosen smaller. This ensures employing a similar number of scatter pixels both at low and high incident angles.

In [49], this approach has been applied to MBES data taken in a very shallow (< 5 m) river environment. It was demonstrated that averaging indeed restored Gaussianity of the beam backscatter values.

Table 5.1: Partition of beam angles and related tolerance angle (θ_{tol}) for averaging over beams

angular range [°]	θ_{tol} [°]
$\theta \geq 38$	2.5
$38 > \theta > 24$	4.4
$24 \geq \theta \geq 20$	6.4

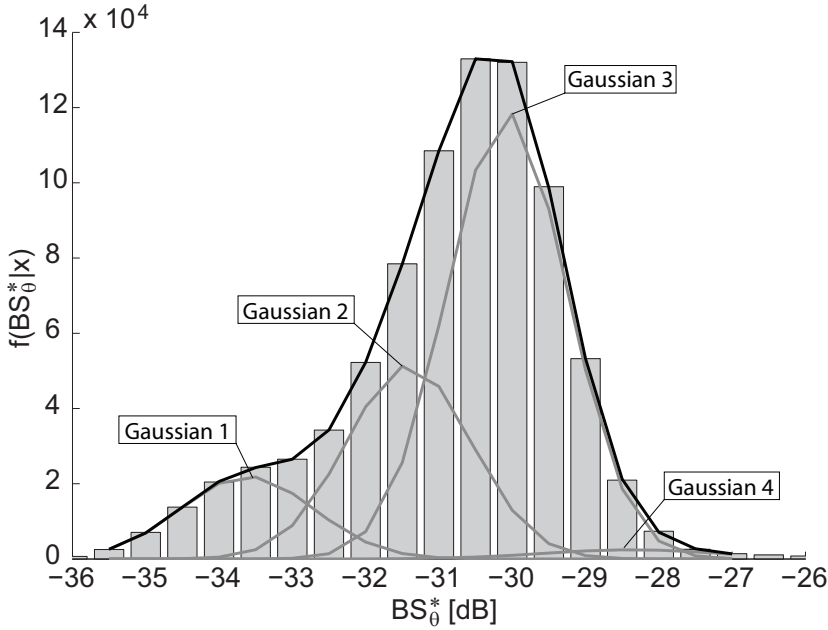


Figure 5.2: Fitting four Gaussians (gray curves) to the histogram of all MREA/BP'07 backscatter strengths at the 46° beam angle. The black curve gives the sum of the four Gaussians.

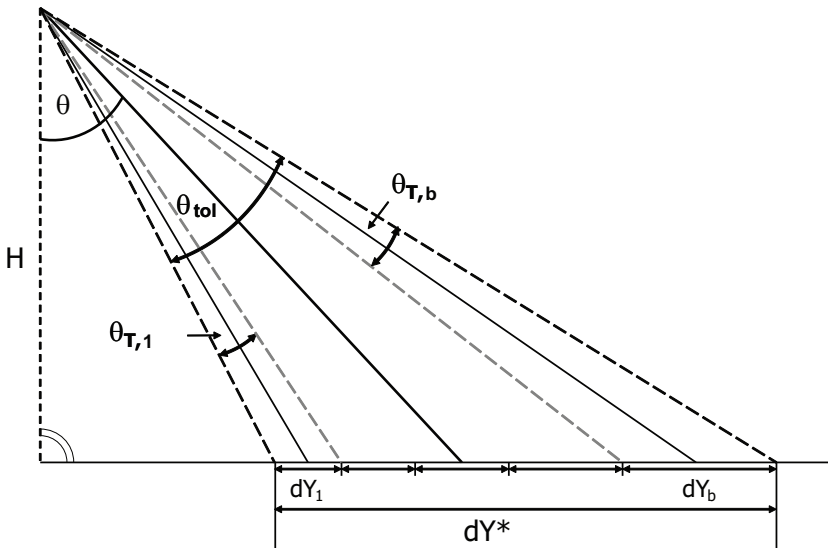


Figure 5.3: Angle of tolerance θ_{tol} . Within this angle all scatter pixels from all beams $\theta_{T,1}, \dots, \theta_{T,b}$ are taken into account for averaging. Here, dY_k , $k = 1, \dots, b$ denote the across-track size of the b footprints, respectively, and dY^* is the across-track size of the footprint dedicated to θ_{tol} .

Table 5.2: Partition of depth values and related number of pings for averaging (p)

depth range [m]	p [-]
<10	12
10-15	8
15-20	6
20-25	4
25-35	3
35-80	2
>80	1

For a given depth H , (5.2) gives a rough estimation for the number of beams used in the averaging as

$$b = \frac{\cos^2 \theta}{\sin \theta}. \quad (5.4)$$

Taking the b beams into account, they span an angular range of θ_{tol} as shown in Fig. 5.3. More precisely, one has to include all beam angles around the central beam angle θ as $\theta - \theta_{tol}/2 \leq \theta \leq \theta + \theta_{tol}/2$. The values of these angular ranges θ_{tol} are determined from Eq. (5.4) and used as tolerances. Typical values used in this contribution are listed in Table 5.1. Based on the fact that the number of scatter pixels at angles smaller than 20° is too small to result in reasonable tolerance angles, these angles are not considered for classification.

After having decreased the angular dependence, we expect that the number of scatter pixels per beam footprint still varies with depth. Therefore, an averaging over $p = p(H)$ pings is proposed in the next step as discussed in [50]. The number of pings involved in this averaging process depends on the water depth H and is determined empirically by comparison of number of scatter pixels at different water depths. The values used in this contribution are presented in Table 5.2.

Averaging over b beams and p pings results in the following backscatter strength values.

$$BS_\theta^* = \frac{1}{p} \cdot \frac{1}{b} \sum_{l=1}^p \sum_{\theta \in \theta_{tol}} BS_{\theta,l} \quad (5.5)$$

The averaged backscatter strengths BS_θ^* are now assumed to have a normal distribution since large numbers of scatter pixels contribute to BS_θ^* . They are employed for classification, using the Bayesian approach for single beams, with beam angles in the range of $\theta_1, \dots, \theta_r$.

From the classification at low grazing angles (which correspond to large beam angles, being reference angles $\theta_1 = 46^\circ$, $\theta_2 = 44^\circ$, and $\theta_3 = 42^\circ$ for the MREA/BP'07 dataset) the number of classes m is determined since a better discriminating performance is expected at these angles. In principle, we expect the backscatter values measured at other angles to feature the same number of classes. Therefore, we assume m to be constant for the considered range of beam angles: $\theta_1, \dots, \theta_r$.

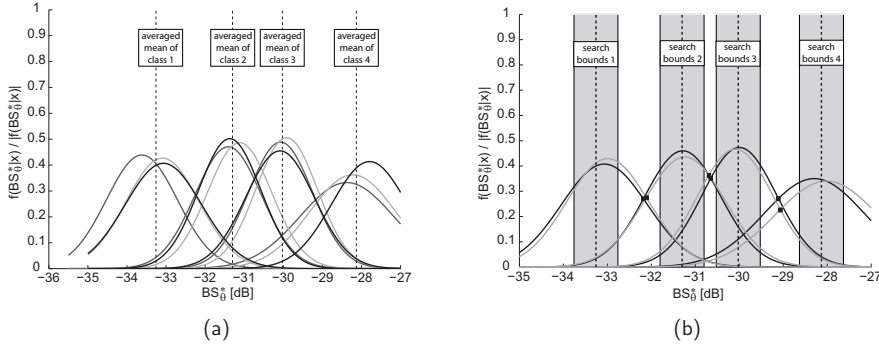


Figure 5.4: Normalized Gaussians at the reference angles (a) and at arbitrary angles (b). In (a), reference angles are chosen as 46° (light gray), 44° (black), and 42° (medium gray). Per angle, the four Gaussians are plotted as estimated by the Bayesian approach for single beam angles. For each class, the average of the Gaussian means is indicated by a vertical dashed line. According to the reference angles, a shift in backscatter strength is applied for all beam angles. Then, the Gaussian mean values at an arbitrary angle are restricted to a boundary of ± 0.5 [dB] around the averaged means obtained at the reference angles. These boundaries are shown in (b) as gray rectangles. Here, classification has been applied to shifted backscatter strength at beam angles of 40° and 38° , indicated by the black and gray curve, respectively. Class boundaries are given by the intersection points (black squares) of the normalized Gaussians.

Additionally, the three initial classifications provide us with the μ_k 's, σ_k 's, and c_k 's for the three reference angles. The mean values (over all reference angles) of the Gaussian PDF parameters $\bar{\mu}_k$, $\bar{\sigma}_k$, and \bar{c}_k ($k = 1, \dots, m$) can then be obtained as shown in Fig. 5.4(a).

For application of the classification method to an arbitrary angle under study (θ), we use the fixed number of classes that has been obtained from the classification at the reference angles. First, the entire histogram of the averaged backscatter strengths BS_θ^* of the angle under study is shifted such that the mean of BS_θ^* becomes identical to the mean of the averaged backscatter strengths at reference angles (θ_1 , θ_2 , and θ_3). As an initial guess for the mean values of the Gaussian PDFs we use $\bar{\mu}_k$ ($k = 1, \dots, m$) of the reference angles. Then, more restricted bounds on the mean parameters are used in the least squares process. Here, these are $\mu_k^l = \bar{\mu}_k - 0.5$ dB for the lower bound and $\mu_k^u = \bar{\mu}_k + 0.5$ dB for the upper bound. Results for beam angles of 40° and 38° are depicted in Fig. 5.4(b).

5.2 Application of the Bayesian approach to the MREA/BP'07 data

The application of the Bayesian approach to the MBES data results in four classes for the considered angular range of $\theta_1 = 46^\circ$ to $\theta_r = 26^\circ$ beam angle. Larger beam angles could not be accounted for, since for these angles the backscatter signals were too weak to be detected in the deeper parts of the trial area. Also, beams near normal incidence are not considered for classification, since they contain too few scatter pixels to assume normally distributed backscatter strength.

Figure 5.5 presents the results. We can identify clearly separable areas, each belonging to a single class. The highest backscatter strengths are found in the shallowest part, close to the Italian coast. Lowest backscatter strengths occur in the area with water depths of approximately 40–60 m. Then, with increasing depth also backscatter strength increases again. However, a somewhat asymmetric distribution between the northern and southern part can be observed at similar depths. In several areas a coexistence of two classes can be observed. Some of these areas coincide with areas identified by particular slope patterns. For example, this holds for the region close to the Ombrone estuary in the eastern part where a regular structure is found in both the slope map (Fig. 3.5) and the map of backscatter strength classes (Fig. 5.5). Also for the irregular structure in the deeper southwestern part, the influence of a second backscatter strength class is revealed to some degree, by showing an additional increase in backscatter strength at the outer beam angles at several locations. Since this behavior is not clearly visible in the other areas, it is hypothesized that the backscatter behavior can be related to geomorphologic features which are already visible in the slope map. Additionally, small scale structures can be recognized in the center of the MREA/BP'07 area, which could not be resolved in the slope map.

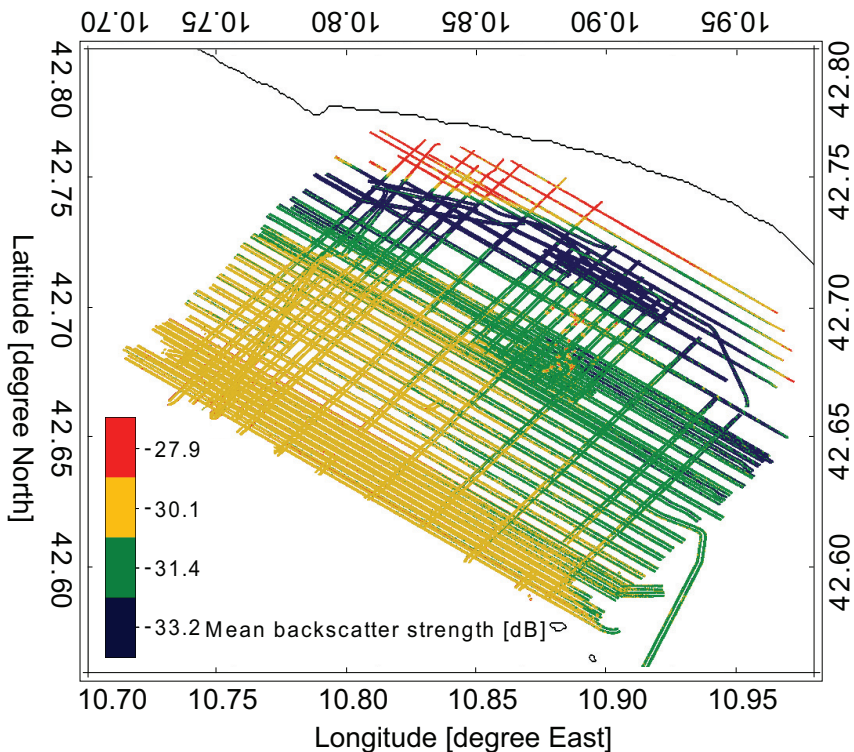


Figure 5.5: Map of the four MBES backscatter strength classes derived for the MREA/BP'07 area.

5.3 Conclusions

The Bayesian approach presented in this chapter enables the detection of classes of backscatter strength per beam. Treating the beams separately is beneficial, since it accounts for across-track variations of the sea bottom. On the other hand, angular dependence of the backscatter strength leads to different classification results for different beams. Making these results comparable based on the introduction of a reference angle has been suggested and proven to work well for a shallow water environment composed of soft sediments.

Still, introducing a reference angle does not account for the difference in scatter pixels contributing to the results at a single angle. Moreover, at angles close to nadir the limited amount of scatter pixels was found to violate the assumption of normal distribution, which is essential for the Bayesian approach. In order to overcome this problem, averaging over beams has successfully been introduced, which not only restores normal distribution but also increases the comparability of the classification results at different beam angles. An additional increase in comparability could be accomplished by an appropriate averaging over a sequence of pings, whose quantity is related to the prevailing water depth.

For the MREA/BP'07 data set it has been shown that the Bayesian approach, extended for a range of beams, provides beamwise results that are in good agreement at the angles considered. Combining the results at the different beams, a map mainly consisting of clearly separable classes could be obtained. On the other hand, few regions with non-uniform classification results exist that are found to coincide with particular slope patterns. The classes obtained have been investigated for possible correlations with the sea bottom type. Indeed, the distribution of the acoustic classes follows the one of the sediment mean grain size obtained from independent bottom grab samples (see Ch. 3.1.3). However, some backscatter strength values cannot be explained solely by the mean grain size. A trend towards a larger backscatter strength for soft sediments is evident from the results. It is assumed that this behavior is induced by the presence of gas in the bottom and/or water column and is enforced by a dominating volume scattering at the very soft sediments. Gas is visible in the seismic profiles (see Ch. 3.1.3) for regions with increased backscatter strength.

Overall, it can be concluded that the presented method provides acoustic classes that are closely related to environmental characteristics. However, interpreting the classes as purely grain size dependent can give erroneous results for specific environments with soft sediments. It is, therefore, advised to involve other environmental parameters in the interpretation of the MBES classification results. This will be the focus of Ch. 8.1.

Efficient geoacoustic inversion strategies

Geoacoustic inversion is an attractive means for estimating physical properties of the environment. With frequencies typically in the range of several hundred hertz, also properties of deeper sediment layers can be estimated.

For inverting environmental parameters from the monitored acoustic field, matched field processing (MFP) is widely accepted [51, 52]. In the simplest version, this technique employs a linear processor to spatially dense acoustic data at a single frequency, in order to find the best match between the measured and modeled acoustic field. For shallow water with turbulences due to waves and tidal currents, however, employing a single frequency is often not sensitive enough. The broad-band version of the MFP (BMFP) allows for applying a set of discrete frequencies [18]. Taking into account a large number of frequencies especially becomes attractive in cases where less spatial information is available, as applies to sparse arrays. Moreover, it has been demonstrated by [25] that employing frequency modulated waveforms and using their frequency coherent information instead of tones at discrete frequencies, is beneficial for sparse arrays down to a single hydrophone. The inversion of modulated waveforms in the frequency domain is summarized under the term model-based matched field processing (MBMF). Accounting for a large number of frequencies, however, comes at the price of large computational demands, requiring efficient optimization techniques as described in [53]. Using the frequency coherent information within the MBMF approach even enlarges the computational effort. In addition, MBMF requires the knowledge of the source spectrum.

In the scope of MREA, rapid application is important. Therefore, the above mentioned geoacoustic inversion methods are investigated regarding their efficiency and an optimal inversion strategy is established. This includes both an adjustment of the settings for the optimization method and an adequate choice of the frequencies inverted for. In order to find such an optimal setting, synthetic data resembling a part of the MREA/BP'07 area are employed.

Based on hydrographic studies in the first part of this thesis (Chs. 3-5), the MREA/BP'07 environment is further described by a three-layer model, consisting of the water column and a stratified sediment layer on top of a subbottom half-space. Environmental parameters considered are the sound speed, attenuation, and density of the sediment and subbottom, as well as the water depth and sediment thickness.

This chapter is partly based on the following publications.

K. Siemes, M. Snellen, D.G. Simons, and J.-P. Hermand: "Feasibility of geo-acoustic inversion using a sparse array of hydrophones at short range," in *Proceedings of the European Conference on Underwater Acoustics (ECUA)*, 5-9 July, 2010, Istanbul, Turkey, 2010.

K. Siemes, J.-P. Hermand, M. Snellen, and D.G. Simons: "Frequency and signal type dependence of the performance of broad-band geoacoustic inversion in a shallow water environment with soft sediments," in *Proceedings of the Underwater Acoustic Measurements (UAM) conference*, 2011.

6.1 Multi-frequency geoacoustic inversion approaches

Geoacoustic inversion is based on finding an optimal match between the measured and the modeled acoustic field, resulting in a parameter combination that is descriptive for the environment. Often, large numbers of parameters are needed to describe both the source-receiver geometry and the environmental features that influence the sound propagation. Since most relations between these parameters and the acoustic field are non-linear, and parameter values, in general, can cover large ranges, the search space is likely to contain local optima. Therefore, global optimization methods are commonly used to search a predefined parameter space for the best set of parameters. An overview of the global optimization methods commonly employed is given in Appendix E.

In order to determine the goodness of fit between the modeled acoustic field for a given parameter combination and the measurements at sparse locations within the acoustic field, these optimization methods employ an objective function, also referred to as energy- or cost function C . Several objective functions are suggested in literature [54–56], correlating the modeled and measured pressure fields either coherent in the spatial or frequency domain, or in a few cases coherent in both. Most of these functions associate a better fit with lower costs or lower energy.

Spatial coherent inversion: A standard spatial coherent processor is the linear Bartlett processor, as given for example in [54]. It can be expressed as

$$B_H = \frac{1}{N_F} \sum_{j=1}^{N_F} \phi_{H_j}, \quad (6.1)$$

with

$$\phi_{H_j} = \frac{\|\sum_{i=1}^{N_H} p_{ij} q_{ij}^*\|^2}{\sum_{i=1}^{N_H} \|p_{ij}\|^2 \sum_{i=1}^{N_H} \|q_{ij}\|^2} \quad (6.2)$$

denoting the spatial coherent summation. Here, p_{ij} is the measured acoustic field at hydrophone i and frequency j and q_{ij} the corresponding model output. The summation is coherent over N_H hydrophones in the spatial domain and incoherent over N_F frequencies. The function B_H reaches its maximum value ($B_H = 1$) in case of total agreement between measurements and model output while it becomes zero if model and measurements are completely uncorrelated. A suitable cost function C_H in the spatial coherent case is therefore

$$C_H = 1 - B_H. \quad (6.3)$$

Frequency coherent inversion: Different ways of incoherent combination of the different hydrophones can be found in literature. The first one presented is simply derived from Eq. 6.1 by changing the order of summation, first coherent over frequency and then incoherent over space [54]. This can be expressed as

$$B_F = \frac{1}{N_H} \sum_{i=1}^{N_H} \phi_{F_i} \quad (6.4)$$

with

$$\phi_{F_i} = \frac{\|\sum_{j=1}^{N_F} \bar{p}_{ij} q_{ij}^*\|^2}{\sum_{j=1}^{N_F} \|\bar{p}_{ij}\|^2 \sum_{j=1}^{N_F} \|q_{ij}\|^2} \quad (6.5)$$

being the frequency coherent summation. Here, the measured acoustic field has been corrected for the source spectrum, resulting in \bar{p} . The corresponding cost function is then analogous to Eq. 6.3

$$C_{F1} = 1 - B_F. \quad (6.6)$$

A different cost function is described in [56], employing a spatial incoherent product of $(1 - \phi_{F_i})$ in the following form.

$$C_{F2} = \left[\prod_i^{N_H} (1 - \phi_{F_i}) \right]^{\frac{1}{N_H}} \quad (6.7)$$

Of the two presented frequency coherent approaches, Eq. 6.7 is found to work well with the MREA/BP'07 data by [26]. In the following, we therefore either use Eq. 6.3 for spatial coherent inversions or Eq. 6.7 for frequency coherent inversions.

6.2 Establishing an optimal inversion strategy

Since broad-band geoacoustic inversion of large parameter sets, which are typically associated with descriptions of the shallow water acoustic field, is computational expensive, efficient processing is important. Computational speed generally depends on the convergence rate of the chosen global optimization approach, on the properties of the underlying model of the acoustic field, and on the dimensions of the parameter space. Here, we use a standard normal modes model to solve the wave equation of the acoustic field (see Appendix D.2) in combination with differential evolution (DE), which is known to be a highly efficient global optimization method (see Appendix E.2). The model accounts for, both, geometrical parameters (defining the source and receiver depth, their range, and the array tilt) and environmental parameters of the water column, sediment layer, and subbottom. Since the geometrical parameters will be known in general, the search ranges for these parameters can be restricted, resulting in increased efficiency. This also restrains the geometrical parameters in dominating the inversion results, a characteristic that was observed by [57]. Beyond this, computational speed can be gained by reducing the number of forward model calculations. This number, however, will also determine the accuracy of the results. An inversion strategy is considered being optimal, when it provides the relevant parameter resolution within a minimal number of forward calculations. This can be achieved by an appropriate choice for the following criteria:

1. the setting of the global optimization method under consideration,
2. the number and height of frequencies involved, and
3. complexity of the environmental model.

While the complexity of the environmental model is merely determined by the preliminary knowledge gained from the hydrographic survey, which is described in the previous chapters, the first two criteria are easily adaptable. Finding appropriate values for these, however, requires an iterative process, which is not presented here. We instead investigate different DE settings under the assumption of a given optimal frequency setting, before we investigate different frequency settings for a fixed optimal setting of the DE.

6.2.1 Criteria for comparing inversion strategies

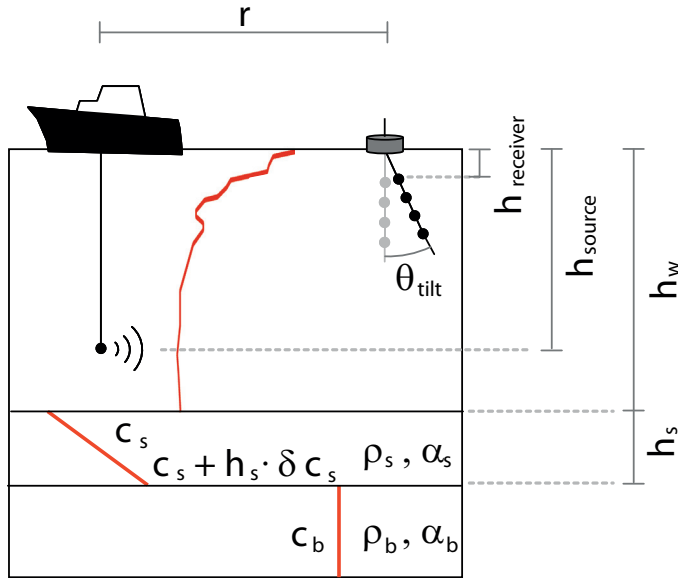
In the process of finding an optimal inversion strategy, assessing the inversion results obtained under the different strategies plays an important role. In order to obtain assessable results, inversions have to be carried out in a well-known environment. For this purpose, synthetic data have been created, closely resembling measurements of a reference run in the MREA/BP'07 area (RUN 2 in Ch 3.1.1), which is the same as in [26]. Synthetic data have the advantage that the true parameter values are known exactly.

The parameter values applied for the current investigation are provided in Fig. 6.1. This figure also shows a schematic of the environment, which is assumed to be range independent. It consists of a subbottom half-space of constant sound speed, covered by a soft sediment layer of constant thickness with a sound speed gradient, and a water column for which the full sound speed profile is measured. Here, the source is located at a range of 0 m. The source depth was set to 88.7 m. Further, four receiving elements (hydrophones) are placed in the water column in form of a vertical array. The hydrophones are equally 5-m spaced with the upper hydrophone at 20.2 m depth. The source–receiver range is considered at 200-m spaced steps between 600 m and 1800 m.

Using the parameters given in Fig. 6.1, acoustic fields have been created for the same frequencies as considered in the MREA/BP'07 experiment by employing normal mode modeling (see App. D.2). Both discrete tones (multi-tones) and frequency modulated waveforms (chirps) are considered, thereby employing 32 frequencies in the entire low-(LF) to mid-frequency (MF) band (250–1600 Hz) for the multi-tones and 1-Hz sampling in the LF band (300–800 Hz) or MF band (800–1600 Hz) for the chirp signals. Then, the acoustic pressure at the hydrophone positions is inverted using the same normal mode model as employed for generating these data. In the inversion step, also sampling rates larger than 1 Hz are investigated.

In the following, an example is given on how to assess the inversion results. It incorporates LF chirp signals obtained at 1400 m range and sampled at 10-Hz steps. Accordingly, the cost function is taken conform Eq. 6.7. The choice of the signal type and sampling rate is based on the computational efficiency. The choice of the range is based on the model properties, which are described in App. D.2.2. Criteria for assessing the inversion results are the convergency of the cost function and the accuracy and precision of the parameter estimates, which describe the degree of agreement between the inversion results and the true environment. In the following, different ways of representing these criteria are introduced.

Using noiseless data, the cost function is expected to converge to zero. As an example, Figure 6.2 displays the development of the cost function when applying DE over 400 generations with an initial population of 32 members. It is clearly seen that the costs decrease rapidly within the first few generations. This is due to the settings of the crossover rate of 0.55 and the multiplication factor of 0.6, which have been chosen such that a balance



Parameter	Symbol	Units	Value ^a	Lower bound	Upper bound
Water depth	h_w	m	110	105	114
Source depth	h_{source}	m	88.7	75	94
Upper receiver depth	h_{receiver}	m	20.2	14	24
Tilt	θ_{tilt}	°	5	-20	20
Source-Receiver range	r	m	600–1800	Value -10	Value + 10
Sediment thickness	h_s	m	8	1	15
Sediment density	ρ_s	g/cm ³	1.5	1	2
Sediment attenuation	α_s	dB/λ	0.06	0	1
Sediment sound speed	c_s	m/s	1470	1450	1525
Sound speed gradient	δc_s	1/s	3	0	5
Subbottom density	ρ_b	g/cm ³	1.8	1	2
Subbottom attenuation	α_b	dB/λ	0.15	0	1
Subbottom sound speed	c_b	m/s	1530	$c_s + \delta c_s \cdot h_s + 1$	$c_s + \delta c_s \cdot h_s + 250$

^aused for creating the data

Figure 6.1: Schematic of the environment and measurement configuration.

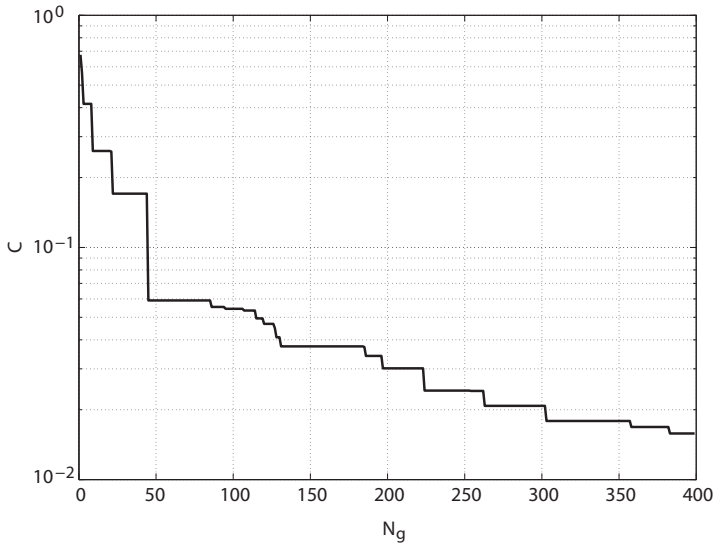


Figure 6.2: Convergency of the cost function.

between a global and local search is established. Converging toward an optimal solution (zero costs), however, requires a much larger set of generations. On the other hand, a too large number of generations is not desirable for efficiency reasons. The optimal choice of the number of generations will be based on its effect on the accuracy and precision of the inverted parameters.

Information on the accuracy and precision of a parameter estimate can be obtained from plotting the costs as a function of parameter value. As an illustration, the upper part of Fig. 6.3 gives such a cost surface for the estimates of the source depth. Also shown in this figure are the true value as a red line and the estimate with the lowest energy as a green line. It can be seen that the solution with the lowest energy can differ from the true solution. Causes for such deviations are for example the presence of multiple optima, a flat cost surface with a range of parameter values resulting in low cost values, or the optimization method not exploring the entire search space.

Therefore, taking the value with the lowest energy as final result might not always be the best choice. Alternatives for selecting an optimal solution can be based on averaging. The different strategies include repeated inversions of the same dataset or averaging over inversion results at neighbored locations (spatial averaging). Repeated inversions are rather computational expensive. Averaging over space, on the other hand, might affect the resolution. Alternatively, one can exploit the fact that processing DE, at least partially, provides insight into the cost surface as shown in the upper part of Fig. 6.3. Averaging can then be based upon these available estimates. The lower part of Fig. 6.3 shows a histogram of the parameter estimates weighted by their cost value, emphasizing solutions with low costs. Here, the green line gives the maximum of the histogram and the red line again gives the true value. Of course, such histograms and thus the interpretation of the results are dependent on the weighing factor.

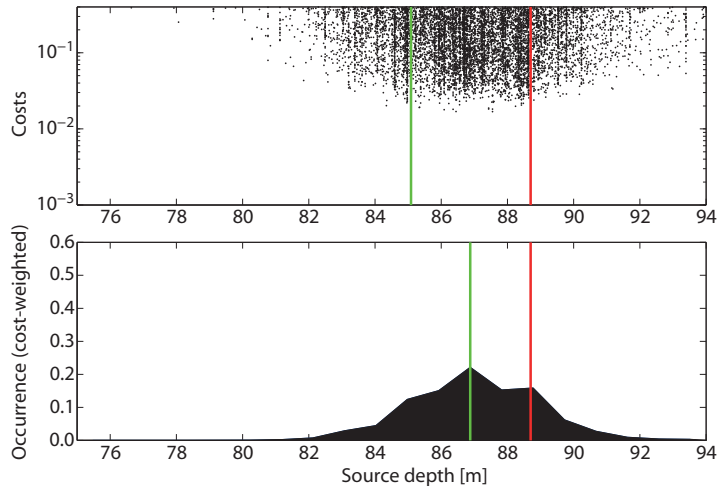


Figure 6.3: Cost surface (upper plot) and histogram (lower plot) of the estimated source depth.

6.2.2 Settings of the global optimization method

The global optimization method chosen for optimizing the match between the modeled and measured acoustic field is DE. This method is further described in Appendix E.2. In the current section, we focus on those properties of DE that affect its computational speed. DE starts with an initial population of randomly chosen parameter value combinations, which are then improved by adding the difference of two randomly chosen parameter vectors (scaled by a factor F), followed by crossover (with crossover rate p_c) during N_g successive generations of constant size Q . The choices of F and p_c mainly affect the rate at which new features are admitted in a new generation. Therefore, they determine the speed at which the entire parameter space is searched and the extent of this search. However, these two parameters are merely determined by a compromise between a fast search of the parameter space and the convergency toward the optimal solution. The number of forward model calculations $N_g \cdot Q$ determines both the computational costs and the quality of the results. For the DE setting it is, therefore, important to find an appropriate setting of these variables. An optimal setting of DE for a 6-parameter model has been discussed in [58]. For creating a new generation, it considers a crossover rate of $p_c = 0.55$ and a scaling factor of $F = 0.6$. Furthermore, a population size of $Q = 16$ and $N_g = 150$ generations are proposed. This setting is taken as a basis for the current inversion effort. Here, however, more parameters have to be inverted for. Therefore, DE has also been applied for larger Q and N_g value combinations. In total, five combinations of Q and N_g are compared for the synthetic data sets described in Ch. 6.2.1. The chosen settings are listed in Table 6.1.

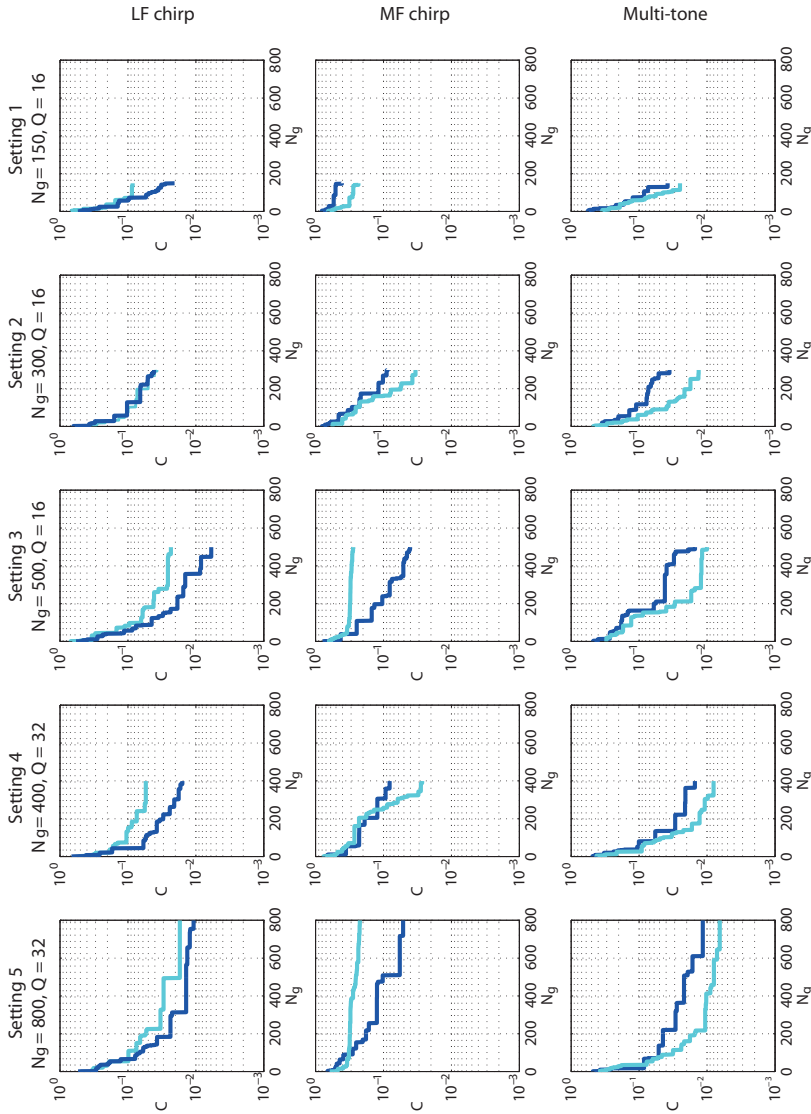


Figure 6.4: Convergence behavior of the cost function for settings 1-5 (see Table 6.1) for LF chirps, MF chirps, and multi-tones. The light and dark blue lines give the costs for settings with a source-receiver range of 800 m and 1400 m, respectively.

Table 6.1: Settings of the DE global optimization tested with synthetic data

Setting	Q	N_g	$N_g \cdot Q$
1	16	150	2400
2	16	300	4800
3	16	500	8000
4	32	400	12800
5	32	800	25600

The use of a specific energy function is mainly motivated by the type of signal transmitted. For discrete multi-tone signals, in general, no information about the relative magnitudes and phases of the different frequencies is available. Consequently, signals at the different frequencies are combined incoherently. The information contained in the signals is their spatial behavior, expressed in the phase and magnitude variation over depth. To account for this, the frequency incoherent broadband Bartlett processor is used, as described in Eq. (6.3). For chirp signals, on the other hand, the relative magnitudes and phases of the different frequencies are generally known. In order to incorporate this information in the inversion process, a frequency coherent processing is applied according to Eq. (6.7).

Assuming that the selection of an optimal number of frequencies has already been made², in the following, 32 frequencies are accounted for in the inversions of the synthetic multi-tones and the synthetic chirp signals are sampled at 10 Hz each, corresponding to 50 frequencies in the LF band and 80 in the MF band.

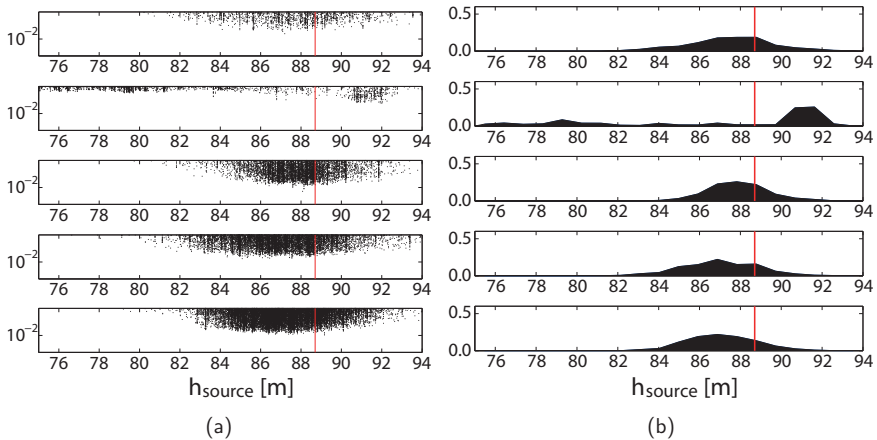


Figure 6.5: Comparison of the estimates of the source depth for settings 1-5 (see Table 6.1). In (a) the cost surface is shown and in (b) the related cost-weighted histograms are given. Red lines indicate the true value.

²The choice of different frequencies is discussed in Ch. 6.2.3.

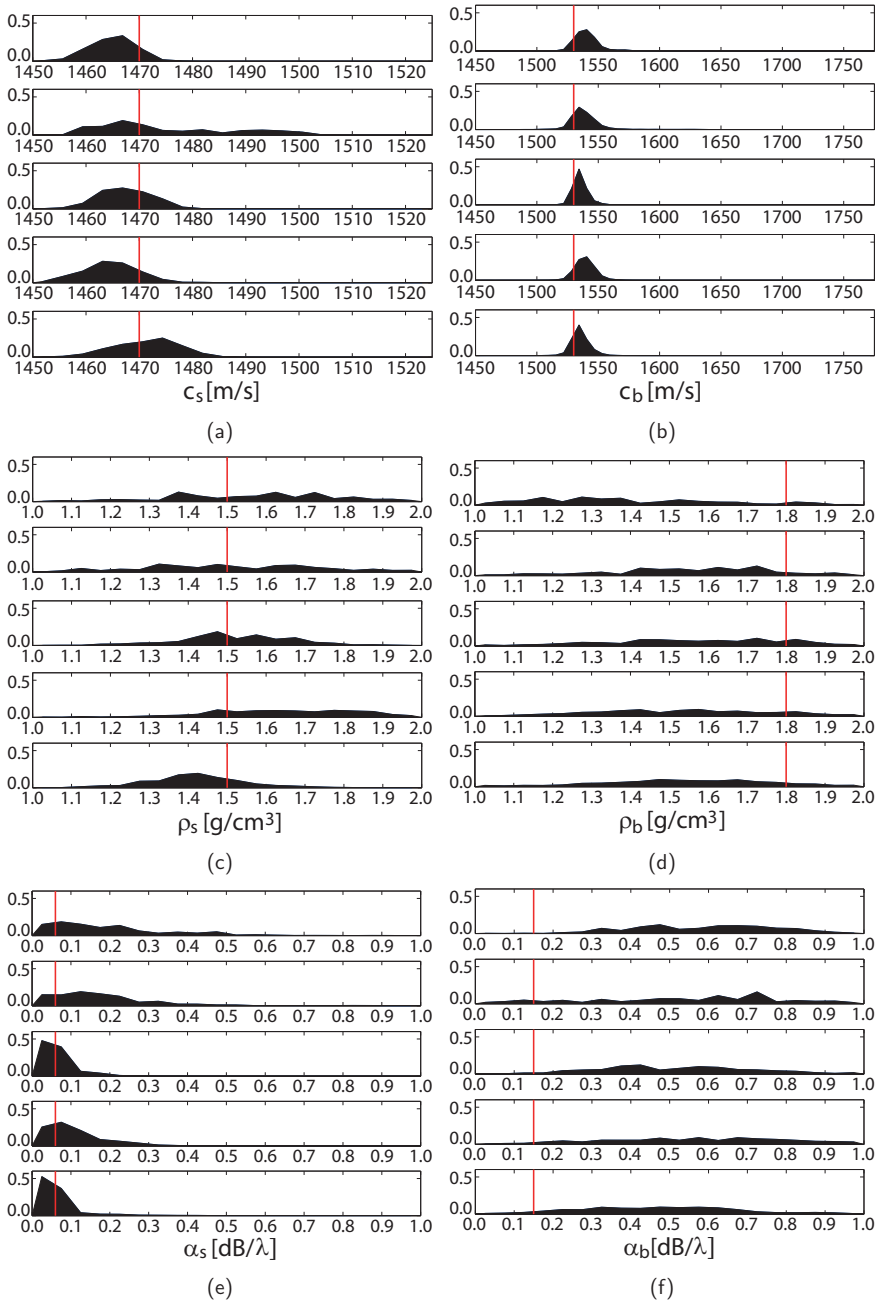


Figure 6.6: Histograms of the environmental parameters: (a) sediment sound speed, (b) subbottom sound speed, (c) sediment density, (d) subbottom density, (e) sediment attenuation, and (f) subbottom attenuation. Comparison of the estimates for settings 1-5 (top top to bottom) of Table 6.1.

A function of the lowest cost per generation is shown in Fig. 6.4 for inversions at 800 m and 1400 m source–receiver range, for all settings and signal types. Clearly, the setting with the smallest number of forward calculations (setting 1) has not fully converged. As expected, a better convergence is obtained for settings with an increased number of forward calculations (settings 3–5, in particular). Also evident from Fig. 6.4 is that both the inversion of the LF chirp signals and multi-tones, which incorporate LF signals as well as MF signals, show a better convergence behavior than the inversion of the MF chirp signals.

Further investigations of the LF inversion results show that the cost level decreases for settings with a larger number of population members and a larger number of generations. This is documented in Fig. 6.5, which is an extension of Fig. 6.3, showing the cost surfaces and cost-weighted histograms for the five settings, which are listed in Table 6.1. Also a better exploration of the search space is evident for the settings with a large number of forward calculations.

Similar histograms are provided for the environmental parameters of the sediment layer and subbottom in Fig. 6.6 to point out the accuracy and precision of the distinct parameter estimates for the different settings. From these histograms, we again observe that settings 1 and 2 generally contain too few forward calculations to converge to the true value. Beyond this, Fig. 6.6 helps to identify those parameters which can be estimated well. In general, the environmental parameters are found to be separable into two groups regarding their accuracy and precision. One group of parameters is approximating the true value with reasonable accuracy and parameter-dependent precision. This group includes the sound speed of both layers and the attenuation in the sediment. Estimates of other parameters, under which the density in both layers and the attenuation in the subbottom, show a low precision and often as well a low accuracy, resulting in larger deviation from the true parameter values. We will show later for real data (Ch. 7) that these deviations in the estimates can be overcome at least partly by applying spatial averaging.

With the knowledge of the accuracy and precision of the distinct parameter estimates, we now extend the comparison of the inversion strategies to different source–receiver ranges and different types of signals. The focus is on those settings which promise to provide the best estimates according to the former analysis. These are settings 3–5. The results of inverting the synthetic signals using these settings are presented in Figures 6.7–6.9 for the LF chirps, MF chirps, and multi-tones, respectively. For each range r_0 considered, the parameter combination corresponding to the lowest energy function value is shown.

Comparing the results, we observe a similar trend regarding the possibility of estimating distinct parameters from these signal types. Only a few parameter estimates match the true value for all settings, ranges, and signal types. This holds for the tilt θ_{tilt} , the source–receiver range r , and with exceptions for the sound speed in the subbottom c_b . Parameters that often do not reflect the true value are the density of the sediment ρ_s , the density of the subbottom ρ_b , and the attenuation in the subbottom α_b , as already observed from Fig. 6.6. For the other parameters, a benefit of an increased number of forward calculations and, especially, an increased population size (settings 4–5) is visible for the frequency coherent inversions of the chirp data. However, the additional benefit of these settings is less evident for the spatial coherent inversions of the multi-tones. In general, at least 8000 forward calculations are needed, to obtain reasonable results. Although there is not much difference, a further increase in the population size tends to give slightly better results. Differences in the quality of the results are observed among the three datasets.

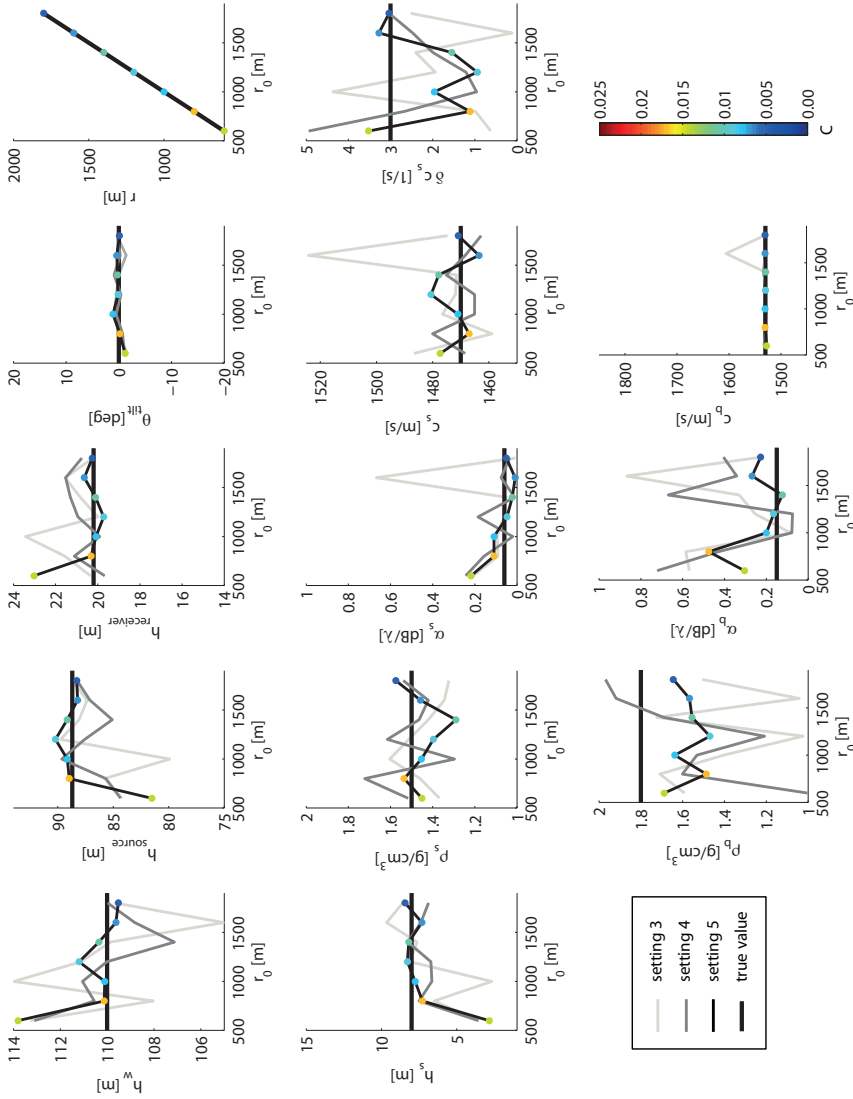


Figure 6.7: Optimal parameter values for three DE settings: 3) 8000, 4) 12800, and 5) 25600 forward calculations using LF chirps. The horizontal black lines indicate the true parameter values.

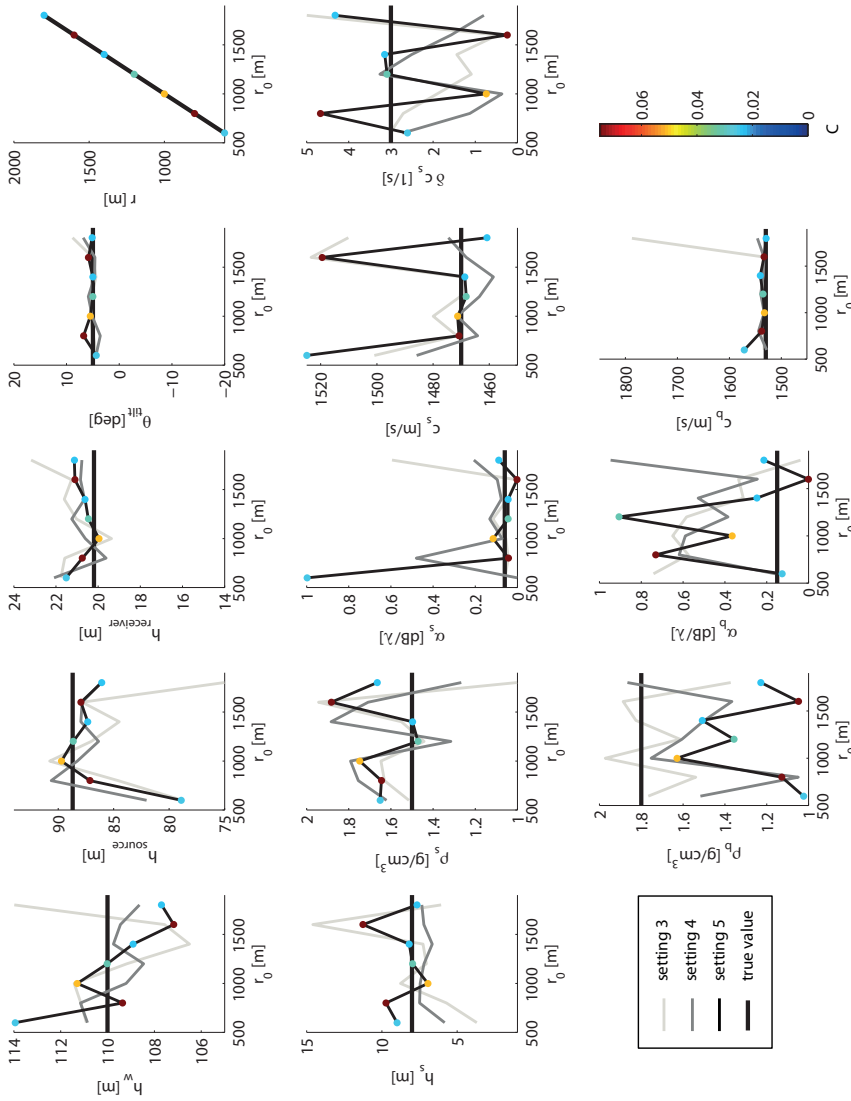


Figure 6.8: Optimal parameter values for three DE settings: 3) 8000, 4) 12800, and 5) 25600 forward calculations using MF chirps. The horizontal black lines indicate the true parameter values.

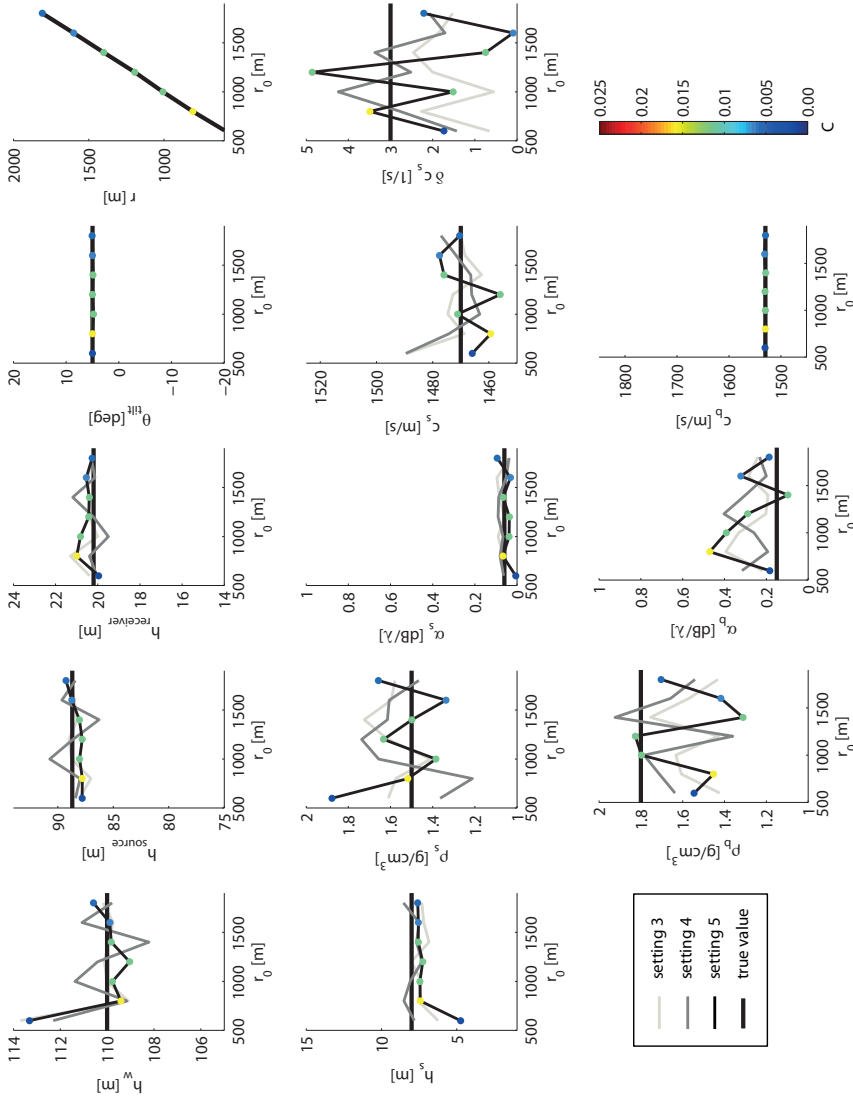


Figure 6.9: Optimal parameter values for three DE settings: 3) 8000, 4) 12800, and 5) 25600 forward calculations using multi-tones. The horizontal black lines indicate the true parameter values.

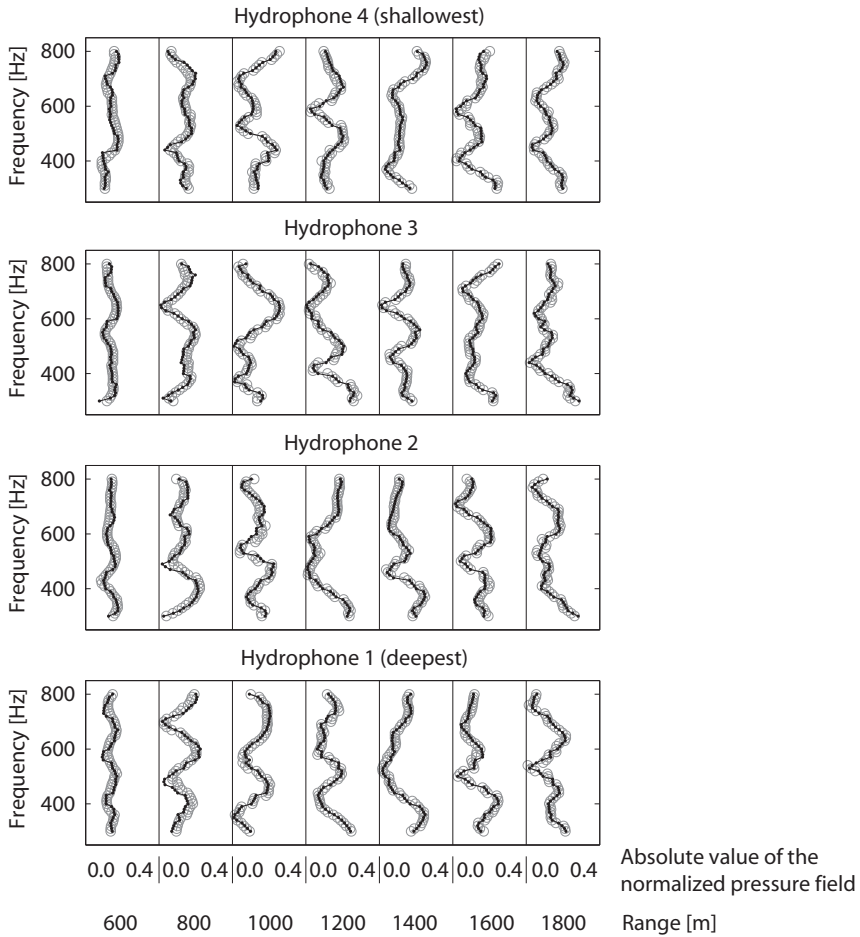


Figure 6.10: Absolute values of the normalized acoustic pressure field at the four hydrophone positions at ranges between 600 and 1800 m, calculated for the true parameter values (black dots) and for the parameter estimates that are obtained according to setting 4 after 12800 forward calculations (gray circles).

In general, low-frequency inversions (Fig. 6.7) are found to provide better results than the mid-frequency inversions (Fig. 6.8), using the same setting. For some parameters, however, a combination of both frequency ranges is beneficial, as observed from the multi-tone inversions (Fig. 6.9). Further, a range dependence of the inversion quality is evident for several parameters. These include the water depth h_w , sediment thickness h_s , and source depth h_{source} . Estimates of these parameters are improved for larger ranges, as expected from considerations in App. D.2.2.

Regardless the extent to which a parameter can be estimated, we show in Fig. 6.10 that the estimates for setting 4 provide a realistic match of the acoustic field at the four hydrophone positions for all ranges considered. The following analysis is, therefore, based

on setting 4 (with $Q = 32$, $N_g = 400$), keeping in mind that even for a good agreement between the true and estimated acoustic field deviations in the accuracy and precision can occur among the parameters. Here, the synthetic inversions can also be employed to identify those parameters that are well-determined.

6.2.3 Frequency dependence of the inversion results

The number and height of frequencies are directly related to computational speed. As holds for the setting of the optimization algorithm, the choice of frequencies also influences the quality of the inversion results. Since for each frequency the wave equation needs to be solved, the number of forward calculations is directly proportional to the number of frequencies. Furthermore, the time required for solving the wave equation decreases with decreasing frequency height. Thus both, a lower frequency range and a lower number of frequencies are computationally favorable. These, on the other hand, might result in a less accurate model or incorrect parameter value estimates. Both choices are application related and might be different for sonar performance tests or coastal engineering projects.

The number of modes N_m is related to the frequency and the environmental conditions, as described in [59].

$$N_m = \frac{2(h_w + h_s)f \ln(\sqrt{1 - \frac{\bar{c}}{c_b}} + 1)}{\bar{c} \ln 2} + \frac{1}{2} \quad (6.8)$$

Here, h_w and h_s are the water depth and sediment thickness, respectively. Further, \bar{c} is the sound speed averaged over the water column and sediment layer, and c_b is the sound speed of the subbottom. Since a range independent environment is assumed, variations in N_m will be dominated by frequency changes. For the frequency bands considered, the number of modes ranges between 9 and 26 for the low-frequencies and can reach up to 114 for the mid-frequencies. Inversions of the LF signals are, therefore, more efficient and consequently preferred when dealing with large sets of environmental parameters. However, efficiency is not the only criterion. The capability of the low number of modes, associated with the LF signals, to resolve differences in the acoustic field due to environmental variations needs further investigation. Especially, the results are expected to be sensitive with respect to the number of frequencies accounted for.

For studying the effect of reducing the number of frequencies, inversions of the LF chirps sampled at 1 Hz, 2 Hz, 10 Hz, and 20 Hz intervals have been carried out. These are thus accounting for 500, 250, 50 and 25 frequencies for establishing the acoustic field, respectively. The setting of DE is taken according to Ch. 6.2.2 as setting 4 ($p_c = 0.55$, $F = 0.6$, $Q = 32$, and $N_g = 400$). Histograms of the estimated environmental parameters are presented in Fig. 6.11. From these histograms only little difference in both the accuracy and the precision of the estimates is seen for the different sample rates. There is also no evidence that parameters which are not estimated well in the inversions with 10 Hz sampling (Fig. 6.6) benefit from smaller frequency steps. The computational extensive inversions of the 1 Hz sampled signals are, therefore, no longer considered. In the following, the remaining sampling rates are compared for a larger set of ranges. Figure 6.12 gives the best estimates per range for the LF chirp signals sampled at 2 Hz, 10 Hz, and 20 Hz. From this comparison, it can be concluded that estimates of those parameters which can be inverted are reasonable for frequency steps up to 10 Hz. A 10-Hz sampling is thus appropriate for both quality and computational speed.

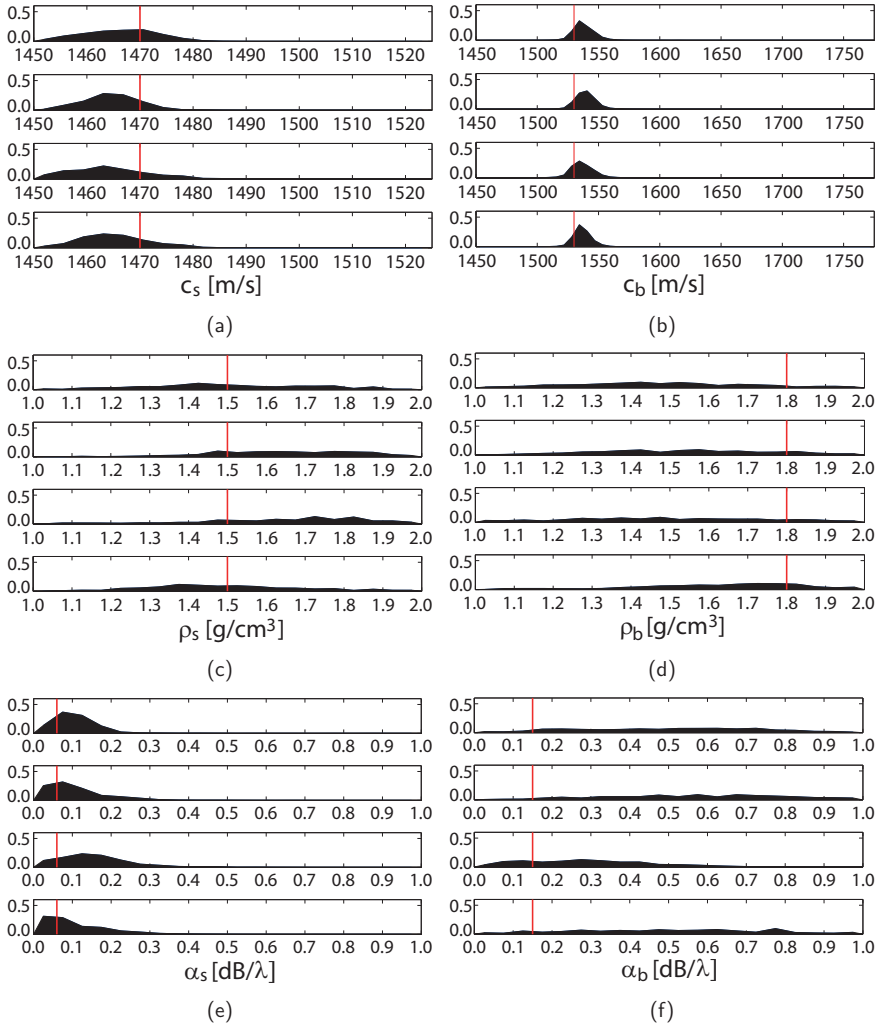


Figure 6.11: Histograms of the environmental parameters: (a) sediment sound speed, (b) subbottom sound speed, (c) sediment density, (d) subbottom density, (e) sediment attenuation, and (f) subbottom attenuation. Comparison of the estimates for frequency steps of (from top to bottom) 20 Hz, 10 Hz, 2 Hz, and 1 Hz for the low-frequency chirp data.

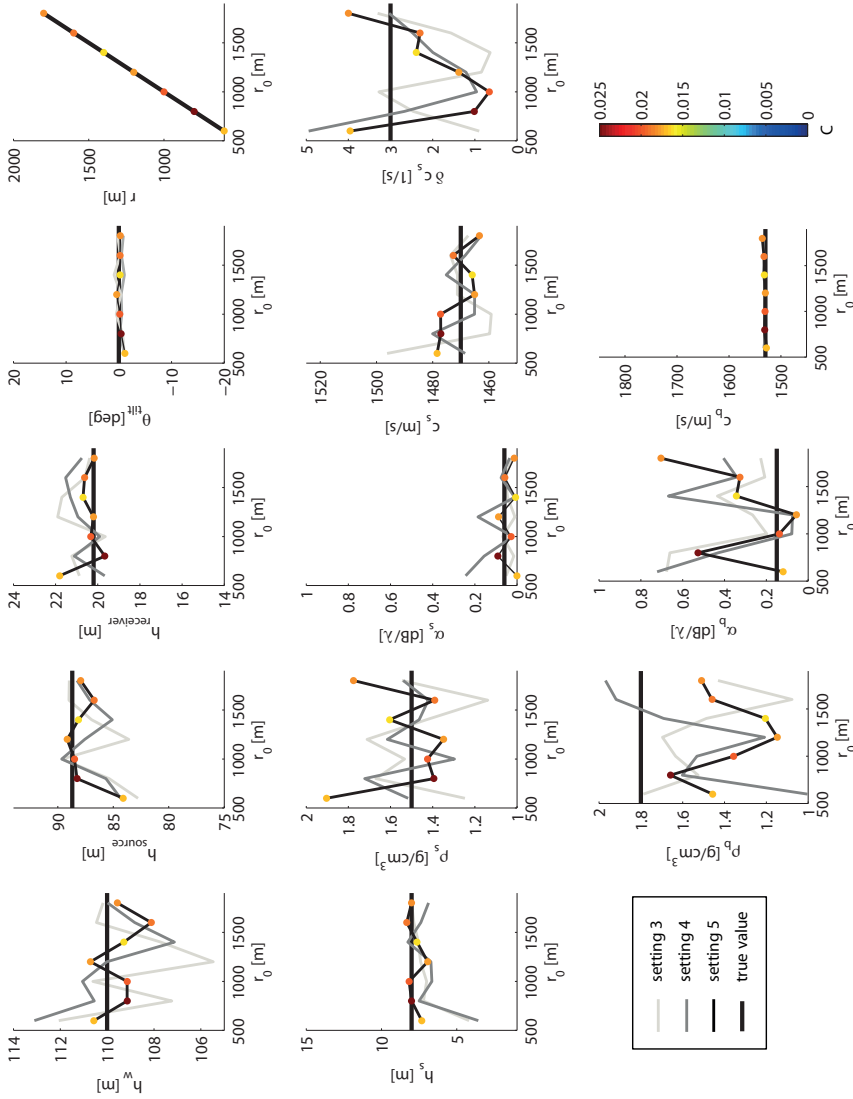


Figure 6.12: Optimal parameter values for three frequency steps: 2 Hz, 10 Hz, and 20 Hz using LF chirps. The horizontal black lines indicate the true parameter values.

6.3 Conclusions

The inversion of synthetic data has provided a strategy that is both computationally favorable and providing realistic estimates of the acoustic field. This strategy incorporates normal modes modeling together with differential evolution over 400 generations of a 32-member strong population, using a cross-over rate of 0.55 and a multiplication factor of 0.6.

One should notice that, even for a good agreement between the true and estimated acoustic field, not all parameters estimates have the same accuracy and precision. Here, the investigation of synthetic data also helps to identify those parameters that are well-determined.

It is shown that the inversions of low-frequency signals are highly efficient and, beyond that, provide better parameter estimates than the inversions of mid-frequency signals alone. Some parameters, however, benefit from a combined inversion of low- and mid-frequency signals. In general, accounting for a large number of frequencies increases the accuracy and the precision of the inversions. The required precision, however, depends on the application. The following conclusions are based on the aim of mapping sediment classes. For the low-frequency chirps it is found that the number of frequencies could at least be reduced by a factor of 10, compared to the original sampling of 1 Hz. Still, this sampling rate corresponds to 50 times 12800 forward calculations of the acoustic field during the optimization process, with each employing 9 to 26 normal modes.

Geoacoustic inversion in practice

In the previous chapter, investigations of synthetic acoustic fields have provided an efficient strategy for inverting parameters of the underwater environment. The aim of the current chapter is to show the ability of geoacoustic inversion, performed under this strategy using real data, to distinguish between environments with different properties of the sediment and subbottom. Primarily, two environmental aspects and their influence on the inversion results are discussed. These are the presence of gas in the sediment and the effect of an increased layer thickness.

First, the optimal inversion strategy found for the synthetic data in Ch. 6 is confirmed to be also suitable for real data in a similar environment. Then, geoacoustic inversion is performed at two additional locations in order to show its ability to distinguish between different environments.

Data applied in the current chapter are obtained during the MREA/BP'07 trial, which is described in Ch. 3.1. Available are measurements of discrete tones (multi-tones) in the band of 250–1600 Hz and frequency modulated waveforms (chirps) in either the 300–800 Hz LF band or 800–1600 Hz MF band. These are the same signals as investigated for the synthetic data.

7.1 Confirmation of the optimal inversion strategy

The inversion strategy introduced in Ch. 6 is based on normal mode modeling (Appendix D.2) of the acoustic field and differential evolution (DE, Appendix E.2) for finding the best parameter representation of this field. The settings for DE were then chosen as given in Table 7.1. Further, a 10-Hz sampling of the LF chirp signals was found to be sufficient for the current purpose of environmental classification.

For real data, other than for the synthetic data, additional uncertainty will be caused at least by the presence of noise and slight variations in the ocean environment. This might require a refinement of the optimal inversion strategy found for the synthetic data.

Table 7.1: Optimal setting of the DE optimization approach.

DE parameter	symbol	parameter value
cross-over rate	p_c	0.55
multiplication factor	F	0.6
population size	Q	32
number of generations	N_g	400

In order to confirm that the settings for DE and the optimal frequency steps, found in Chs. 6.2.2 and 6.2.3, are also valid for real data, they have been applied to the RUN 2 data of the MREA/BP'07 experiment³, which formed the basis for creating the synthetic data. Then, the results are compared to one another and to independent data obtained from the hydrographic survey (Ch. 3.1), containing depth measurements by echosounding and measurements of the hydrophone depths by pressure sensors.

7.1.1 Inversion of synthetic vs. real data

For reasons of comparability, the synthetic and the real data inversion are performed in the exact same manner. This includes the use of the same environmental model, which is composed of three layers: the water column, a sediment layer, and the subbottom. Also, the parametrical description of the environment and of the receiving geometry are the same for the synthetic and real data inversions, as documented in Fig. 6.1. The two main differences between the synthetic and real scenario are the presence of noise in the real data and slight deviations of the real environment from the ideal range independent model. Both aspects have given reason to the actual comparison of synthetic and real parameter estimates. First, the same steps are taken as with the synthetic data in Ch. 6, covering an investigation of three different signal types, which are the LF and MF chirp signals and the multi-tones, and different sample rates. This is to confirm that the selection of the inversion strategy can be based on the synthetic inversions. Then, a detailed comparison of the results, obtained from the synthetic and real data inversion, is given.

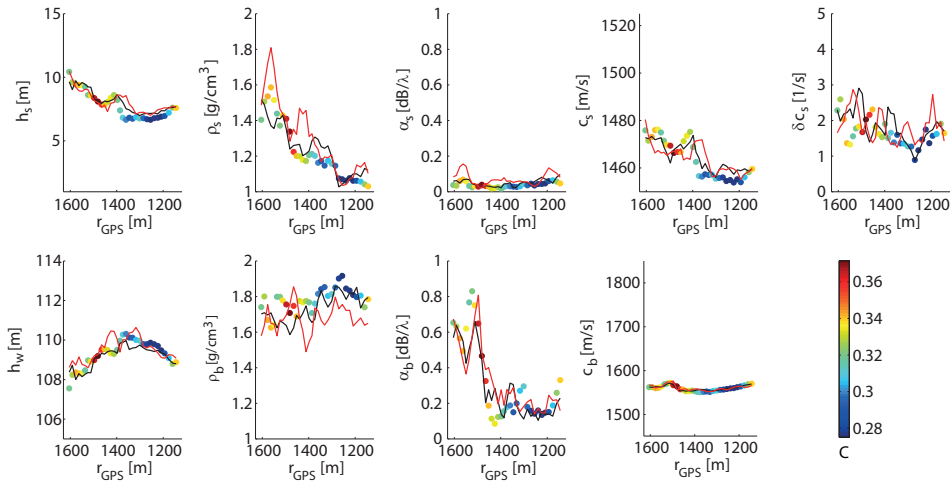


Figure 7.1: Averaged environmental parameters between locations ST3 and ST7 estimated by geoacoustic inversion of the 300–800 Hz LF chirp signals, sampled at 2 Hz (colored dots, with color indicating the costs C), 10 Hz (black line), and 20 Hz (red line).

³see Tables 3.2, 3.3, and Fig. 3.2 of Ch. 3.1

As with the synthetic data, we start with the low-frequency inversions. Figure 7.1 shows the inversion results of the environmental parameters for LF chirps, sampled at different frequencies (2 Hz, 10 Hz, and 20 Hz). We focus on those source–receiver ranges for which the discrete modes are known to contain sufficient information about the acoustic field, as discussed in Appendix D.2.2. These are ranges larger than 1 km (see Fig. D.4 in Appendix D.2.2).

Spatial averaging has been applied to the parameter estimates over approximately 30 m, accounting for six inversion results, which are the parameter estimates with the lowest cost, at subsequent receiver locations. This is a compromise between accuracy and the reduction of noise. Here, the averaged results of the 2-Hz sampling are considered as reference. They are plotted as colored dots, with the color indicating the cost C of the best fit. Results of the inversion with a 10- and 20-Hz sampling are given as black and red lines, respectively.

From the comparison of the three sampling rates, it is seen that the results are in good agreement for most of the estimated parameters. However, less sensitive parameters, such as densities, benefit from a larger number of frequencies.

The influence of the amount of frequencies accounted for is also visible in Fig. 7.2. This figure compares the acoustic pressure fields estimated in the RUN 2 environment with the measured ones. Measurements are available with a 1-Hz sampling, while the estimates either use a 10-Hz or 2-Hz sampling. In both cases, the pressure fields modeled by the inverted data show patterns closely approximating those observed in the measured data. However, the data show finer structures than the estimates can represent. These differences in the resolution between the modeled and measured pressure fields appear to be only marginally dependent on the sample rate, since similar patterns are found for the 10- and 2-Hz sampling. Rather, limitations of the model at short ranges are expected to cause this slightly coarser resolution. From these results, no clear decision in favor of the 10-Hz or 2-Hz sampling can be made. Finally, the 10-Hz sampling is chosen as a compromise between efficiency and accuracy.

The following comparison of the low-frequency results to mid-frequency results is meant to provide information on the additional value of the mid-frequency inversions, either in form of chirps or multi-tones. The 800-1600 Hz mid-frequency chirps have been sampled at 10-Hz intervals, thus employing 80 frequencies. The results, which have also been spatially averaged over approximately 30 m, are presented by the black lines in Fig. 7.3. Again, the results of the inverted 2-Hz sampled low-frequency chirps, which are the colored dots taken from Fig. 7.1, are given as reference. Clearly, deviations between the low- and mid-frequency results are observed in all parameters. Especially noticeable are the values estimated for the densities of the sediment ρ_s and of the subbottom ρ_b . Densities of the subbottom, in general, should be higher than those of the sediments. However, this is not the case in the inversions applying the mid-frequency data. This might be due to unknown source characteristics such as directivity at the mid-frequencies. A further comparison with the multi-tone inversions (Fig. 7.3, red lines), which contain both low- and mid-frequency information, confirms deviations in the inversion results, when employing mid-frequency signals. From these results an additional contribution of the mid-frequency inversions can neither be confirmed nor rejected. In the following, we therefore focus on the inversion of LF chirps, using the same inversion strategy as favored for the synthetic data (see Table 7.1).

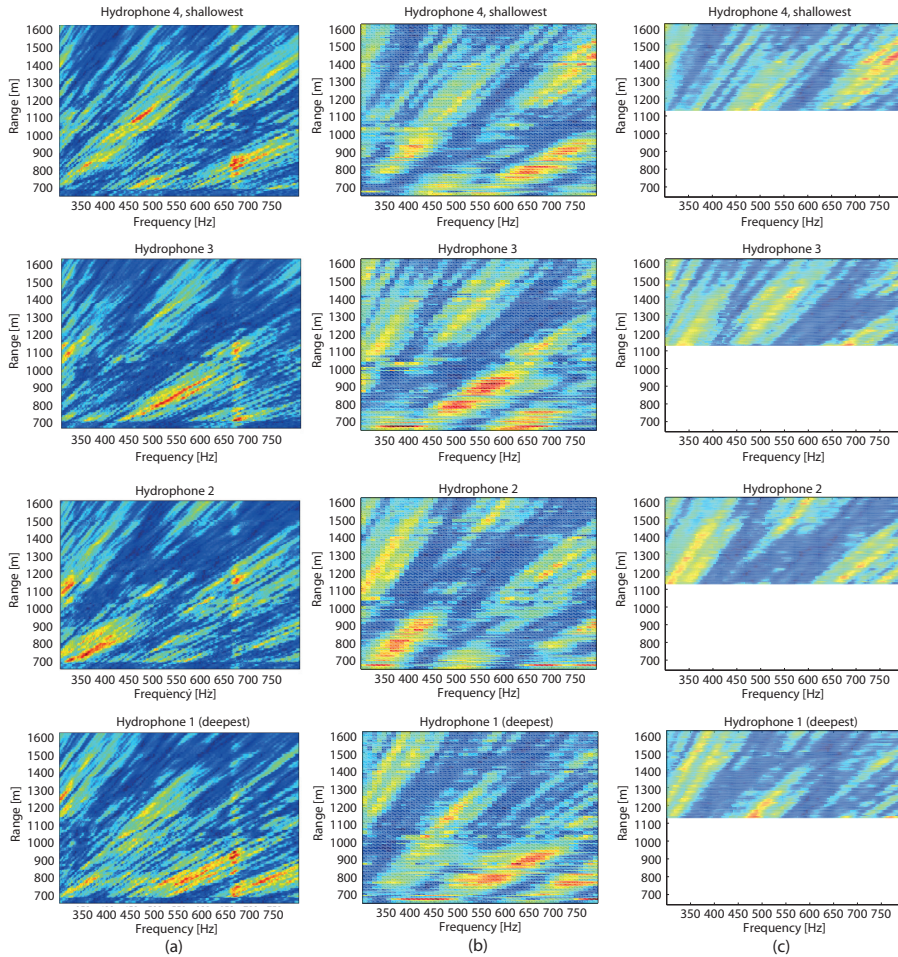


Figure 7.2: Measured (a) and inverted (b and c) pressure fields of RUN 2. Measurements in (a) have a 1-Hz step in frequency. The pressure fields in (b) and (c) are based on a 10-Hz and a 2-Hz sampling, respectively. Due to high computational efforts associated with the 2-Hz sampling, a smaller dataset has been considered.

The results of the real LF data inversion at the RUN 2 location under application of the setting in Table 7.1 and 10-Hz sampling are shown in Figs. 7.4 and 7.5. They are compared to the corresponding results of the synthetic data inversion, provided in Figs. 6.2 and 6.7.

Figure 7.4 displays the lowest costs per generation when the setting described in Table 7.1 is applied. As a result of the presence of noise, the level of costs appears to be higher for the real data (red) than for the synthetic data (black). However, the cost function already converges at 400 generations and additional generations will contribute to a minor decrease in the costs only. This is an aspect in favor of using the setting given in Table 7.1. To further decide on this, the inversion results of the environmental parameters are investigated with regard to their quality. An interpretation of the inverted sediment parameter values follows in Ch. 7.2.

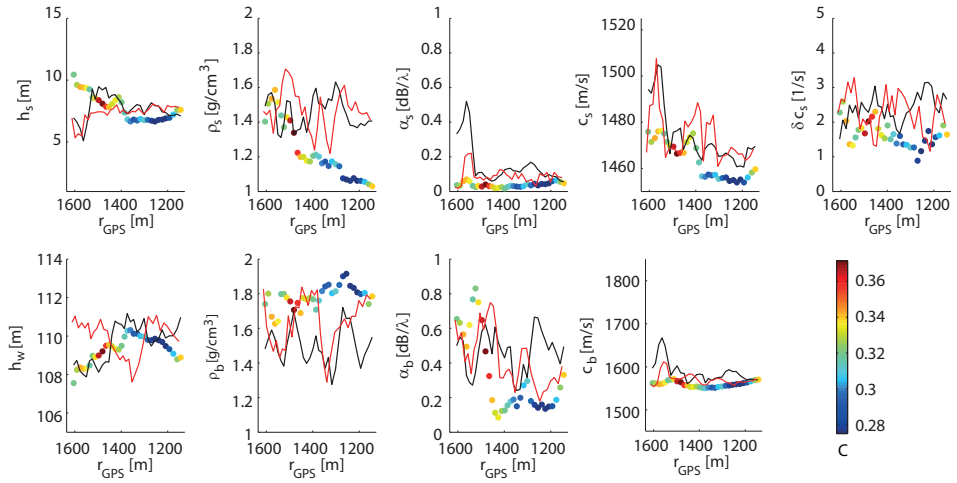


Figure 7.3: Comparison between averaged geoacoustic inversion results from low-frequency chirps, sampled at 2 Hz (colored dots, with color indicating the costs C) to those obtained from either mid-frequency chirps, sampled at 10 Hz (black line) or 32-frequency multi-tones (red line).

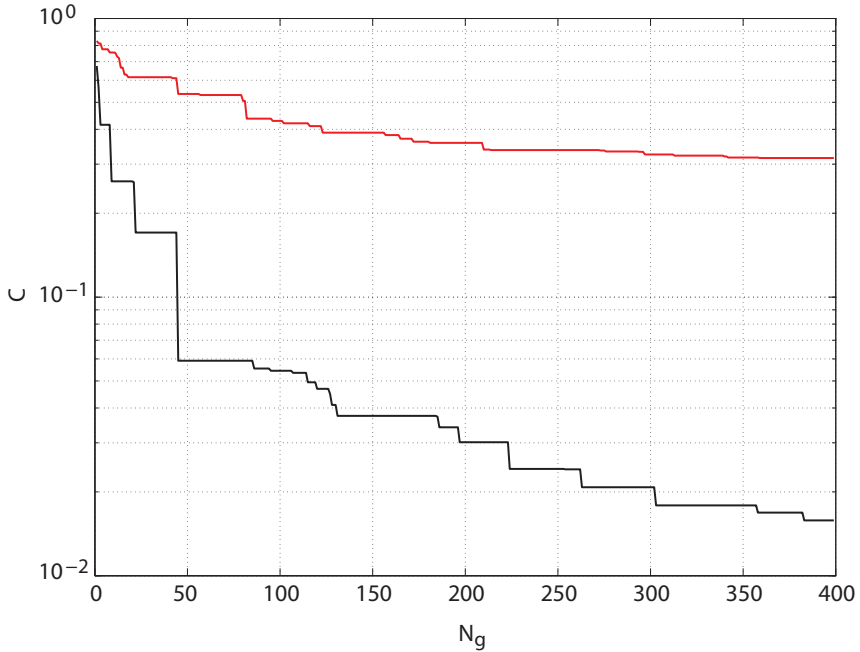


Figure 7.4: Convergence behavior of the cost function of RUN 2 for inversions of synthetic data (black line, repeated from Fig. 6.2) and real data (red line). Both results correspond to a source-receiver range of 1400 m.

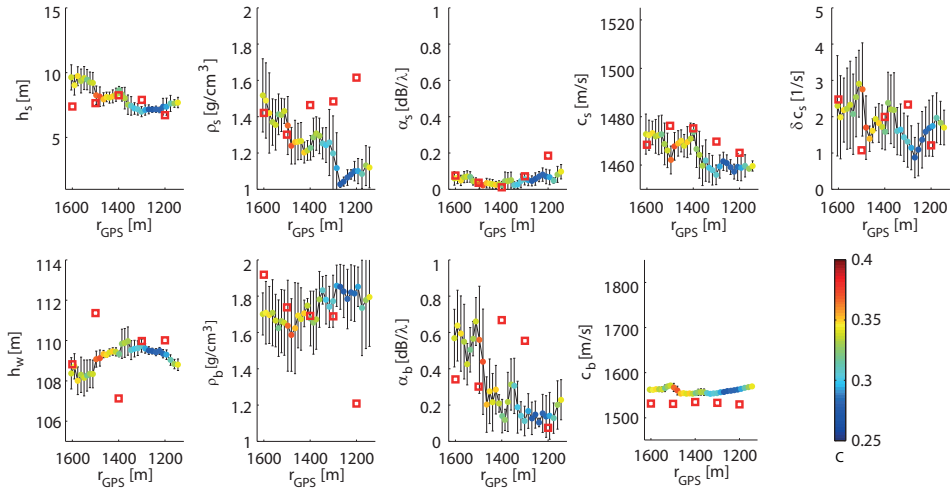


Figure 7.5: Averaged environmental parameters between locations ST3 and ST7 estimated by geoacoustic inversion of the 300–800 Hz LF synthetic (red squares) and real (colored dots, with color indicating the costs C) chirp signals, sampled at 10 Hz. Errorbars showing a single standard deviation are also given for real LF inversions.

Figure 7.5 shows the inverted environmental parameters of the 10-Hz sampled LF data for both the real scenario (colored dots) and the synthetic one (red squares).⁴ It is evident from this figure that the magnitude of agreement between a real estimate and the corresponding synthetic estimate varies per parameter. A possible cause could be the sensitivity of the environmental model to particular parameters. A lower sensitivity regarding the sediment density ρ_s , the subbottom density ρ_b , and the attenuation in the subbottom α_b has already been indicated by the synthetic inversion. The errorbars plotted for the real data, which represent a single standard deviation, confirm the large variation in the inversion results of these three parameters.

However, not all of the estimates of the synthetic inversion fall into this margin of a single standard deviation. The sediment density decreases in the real scenario with decreasing range and reaches a value far lower than that estimated in the synthetic inversion at 1200-m range. Nevertheless, such a decrease in ρ_s is expected according to [60] since the sound speed in the sediment c_s is also decreasing. Furthermore, according to Table A.2 in Appendix A, which is derived from [60–62], this large span of sediment densities for fine grained sediments ($M_z \leq 9\phi$) has also been observed at other sites.

Parameters for which the model is more sensitive, such as the water depth h_w , the sediment thickness h_s , the attenuation α_s and sound speed c_s of the sediment layer, and especially the sound speed c_b of the subbottom, show smaller standard deviations. For these parameters, also the differences between the real and the synthetic estimates often lie within a single standard deviation and larger deviations are limited to single locations. An exception forms the subbottom sound speed c_b , whose real and synthetic estimates differ by approximately twice the standard deviation. Still, these differences are small for c_b , compared to all other parameter estimates.

⁴Note that the colored dots in Fig. 7.5 represent the same inversion results as the black line in Fig. 7.1.

Differences between the synthetic and real data inversion results might be related to the assumptions made for creating the synthetic data, including the choice of the initial values as listed in Fig. 6.1. The synthetic environment is an approximation to the real environment at the location where the receiving unit starts to drift, which corresponds to about 1600 m source–receiver range. This environmental description, under the assumption of range independence, is kept the same at all locations at which synthetic data are created. Whereas in reality, the receiving unit drifts off the straight path between its initial position and the stationary source (Fig. 7.6), resulting in the environment to change slightly for each scenario to be inverted. In the following, such changes in the environment are confirmed by independent hydrographic data.

7.1.2 Confirmation by hydrographic data

For some of the parameters describing the acoustic field, independent measurements exist from a hydrographic survey (Ch. 3.1). These data mainly concern the measurement geometry rather than environmental parameters, which are the focus of the current chapter. Still, the hydrographic survey provides valuable information on the quality of the inversion strategy and its results.

The independent measurements available include depth information of the seafloor as well as depth values of the source and receiver. In the following, depth measurements from

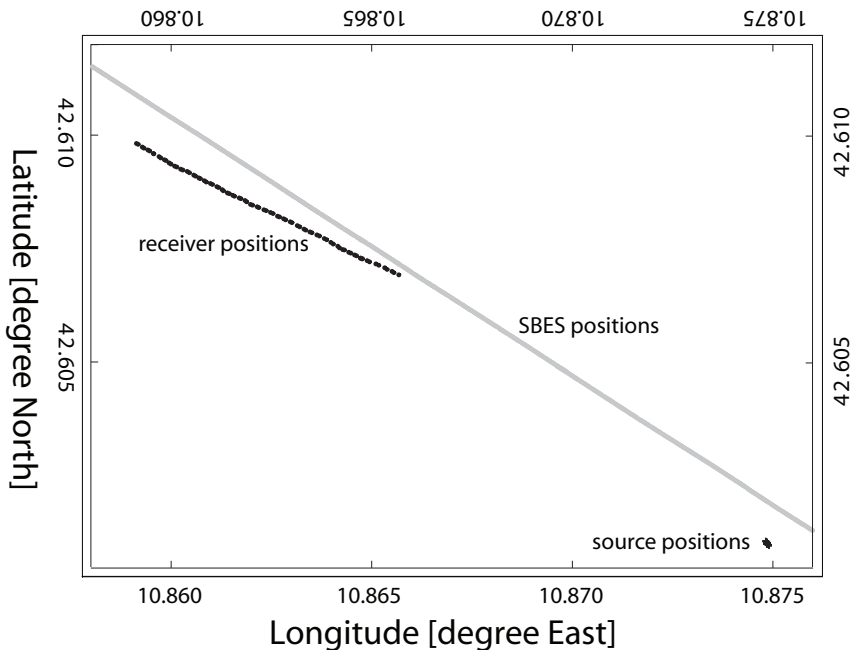


Figure 7.6: Map of the available positions with 12 kHz SBES depth measurements (gray) at the RUN 2 location. The positions of the source and receiver used for geoacoustic inversion are indicated as black crosses and black dots, respectively.

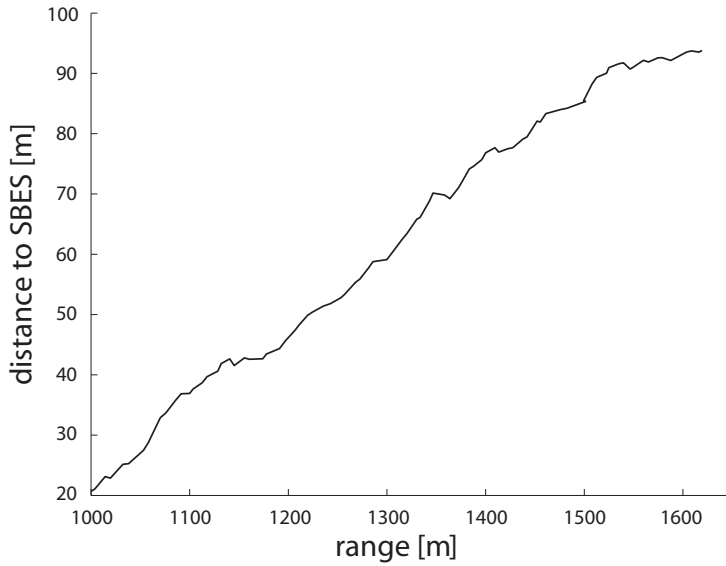


Figure 7.7: Shortest distance between each hydrophone position and available SBES locations.

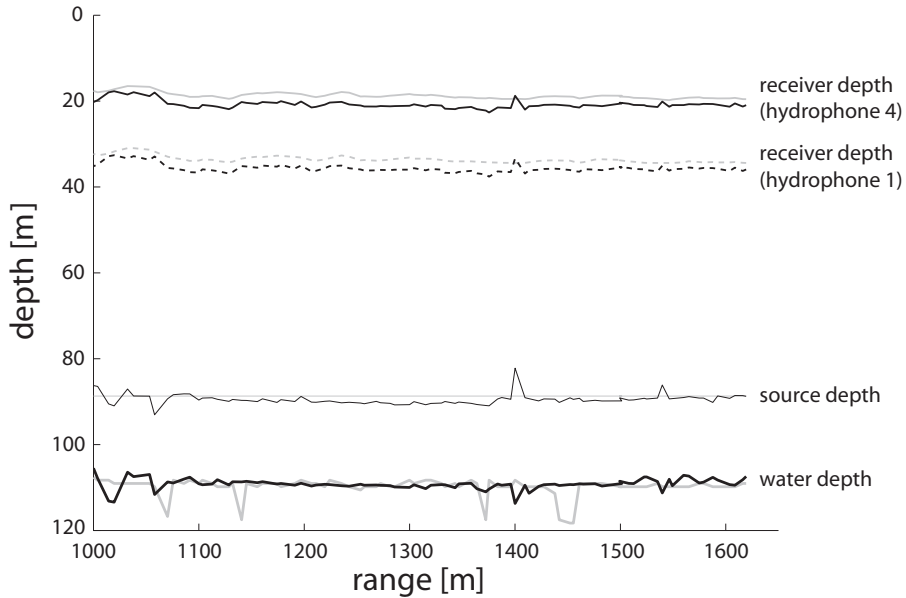


Figure 7.8: Comparison of inverted data (black) and independent hydrographic data (gray). From top to bottom the graphs give the upper and lower receiver depth, the source depth, and the water depth. While the source–receiver geometry is obtained in situ, measurements of the water depth by the 12 kHz SBES device are taken at slightly different locations.

the 12 kHz SBES survey and the source and receiver geometry from pressure sensors are considered for comparison with the inverted data. Pressure measurements at the receiver location have been performed for hydrophone 1 and 4, each about 1 m above the actual hydrophone depth. These measurements are in situ measurements, whereas the pressure at the source location is measured at a single time at the beginning of RUN 2, only. Here, the pressure sensor is located in between the MF-source and the LF-source.

Figure 7.6 shows the locations at which hydrographic information is available. The positions of the source and receiver are given as black crosses and black dots, respectively, and the locations of the SBES depth measurements are given as gray dots. Depth measurements considered here are those which lie closest to the RUN 2 location. It is clearly seen that the distance between the SBES and the receiver increases with the source–receiver range. Figure 7.7, which displays the actual distance between the receiving array and the closest depth measurement, shows that these distances reach values up to 95 m. This has to be considered when comparing the inversion results and the hydrographic data.

Figure 7.8 shows the actual comparison between the inverted values and the hydrographic data. From top to bottom, these lines give the depths of the upper receiver (hydrophone 4), the lowest receiver (hydrophone 1), the source, and the seafloor. While the black lines indicate the inversion results at the lowest costs, the gray lines give the corresponding data obtained from the hydrographic survey. For both receivers, a displacement is seen in the receiver depth. It appears to be nearly constant at source–receiver ranges larger than 1075 m, matching the approximate 1-m offset between hydrophone and pressure sensor. Considering this offset between the hydrophones and pressure sensors, outliers at 1400 m and 1540 m are indicated in the inversion results. What seems to be a better fit in the receiver depths of both hydrophones between 1000 m and 1075 m range, in reality does not match this offset of the pressure sensors. Deviations at these short ranges might be related to an issue discussed in Appendix D.2.2. In Appendix D.2.2 it is shown that measurements at short ranges suffer from only little interaction of the acoustic signal with the sea bottom when using the current measurement configuration. Especially ranges below 1000 m are affected and to a smaller extent also ranges up to 1075 m. Parameter estimates at these ranges are expected to differ from the real values. This is confirmed by the estimates of the source depth and water depth being more noisy at these short ranges.

Estimates of the source depth obtained from the LF data are slightly lower than the value obtained from the pressure sensor. Again, this is expected due to the arrangement of components within the array, being from top to bottom the MF source, the pressure sensor, and the LF source. Here, no clear offset between the estimates and the hydrographic data is seen since for the pressure sensor only a single measurement exists.

For ranges larger than 1075 m, the estimated water depths and the corresponding data are in good agreement. Other than for the receiver depth, however, the pattern of the estimated water depth and of the related SBES measurements differ slightly at all ranges, especially at large ranges. This might be due to the different locations at which the measurements are obtained, as shown in Figs. 7.6 and 7.7. In addition, differences in penetration depth of both the SBES signals and chirps used for geoacoustic inversion have to be considered. This might lead to different structures being revealed from both systems.

Considering all these aspects, a good agreement between the independent hydrographic measurements and the inversion results has been obtained, which confirms the chosen inversion strategy to be appropriate.

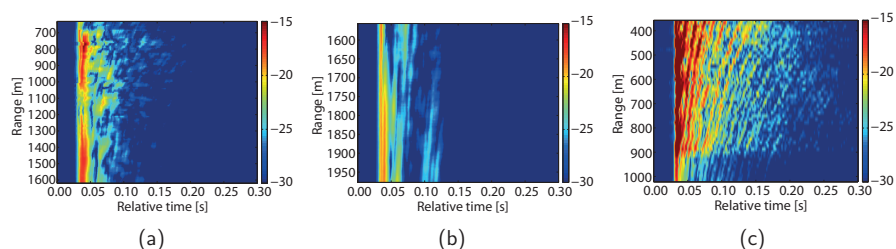


Figure 7.9: Matched filtered signals, from left to right, of RUN 2 (a), RUN 3 (b), and RUN 5 (c).

7.2 The effect of environmental variability on the inversion results

The sediment type is known to be related to environmental parameters such as the sediment sound speed, density, and attenuation [1, 60], which form the basis of the environmental model employed for geoacoustic inversion. Variations in the environmental parameters, however, are not necessarily forced by changes in the sediment type. Other causes might be the presence of gas in the sediment or a variable layer thickness. Their effect on the estimates need to be fully understood when deducing sediment type from the inverted parameters.

Both, the sediment type related effects on the inversion results and those effects related to other environmental properties are investigated in this chapter. For this purpose, geoacoustic inversion of real data is performed at different locations in the MREA/BP'07 area, representing different environmental conditions. In total, three locations are considered for the current analysis. The related runs are listed in Tables 3.2 and 3.3 of Ch. 3.1. They are RUN 2 and RUN 3, both located in the deeper part of the MREA/BP'07 area at approximately 100 m water depth, as well as RUN 5, representing a shallower part of the environment at approximately 50 m water depth. In all cases, the source is staying stationary and the receiving array is drifting toward the source. A first indication of the variability of the acoustic signals is given in Fig. 7.9, which shows the matched filtered received signals of the three runs versus range. However, it should be noticed that beside environmental differences also differences in the source–receiver range occur.

The inversion strategy is taken conform Table 7.1. The parameters to be inverted are the same as for the synthetic inversions, including both geometrical parameters and environmental parameters of the water column, sediment layer, and subbottom.

7.2.1 Very soft sediments and the presence of gas

Throughout the entire MREA/BP'07 area, soft sediments are present. However, grain sizes of 10ϕ and more, as present in the deeper part of the area, are of special interest since they are often not accounted for in environmental models.

In Ch. 7.1, it is already shown that the inversion strategy found for synthetic data is applicable to the very soft sediments associated with RUN 2. Here, a second transect, RUN 3, is considered for comparison. It is taken at a nearby location with similar depth and sediment composition. Results of the inverted environmental parameters at the RUN 2 transect, which have been presented in Fig. 7.5, are repeated in Fig. 7.10. Those of RUN 3

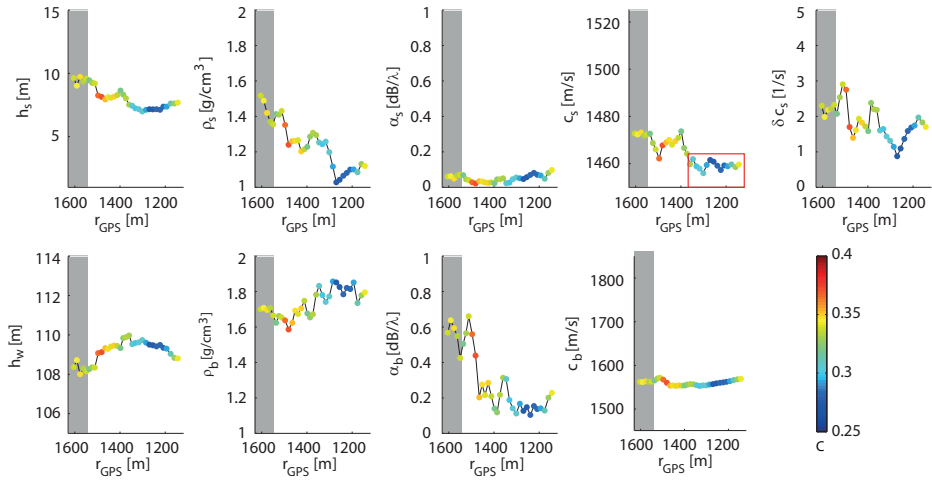


Figure 7.10: Results of the LF chirp inversions for RUN 2, averaged over approximately 30 m. From left to right, the parameters of the first row are the thickness, density, attenuation, sound speed and sound speed gradient of the sediment layer. In the second row, water depth and density, attenuation, and sound speed of the subbottom are given. Colors indicate the costs C of the best inversion result. Gray boxes refer to source–receiver ranges of 1550–1620 m, for which estimates are also available from RUN 3 (see Fig. 7.11). A red frame indicates low values of sediment sound speed, which are associated with the occurrence of gas.

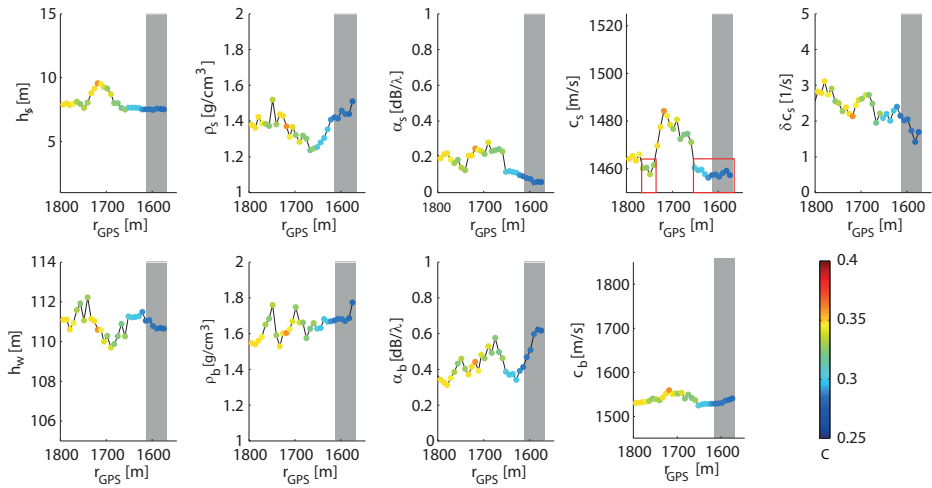


Figure 7.11: Results of the LF chirp inversions for RUN 3, averaged over approximately 30 m. The same parameters as in Fig. 7.10 are presented. Colors indicate the costs C of the best inversion result. Gray boxes refer to source–receiver ranges of 1550–1620 m, for which estimates are also available from RUN 2 (see Fig. 7.10). A red frame indicates low values of sediment sound speed, which are associated with the occurrence of gas.

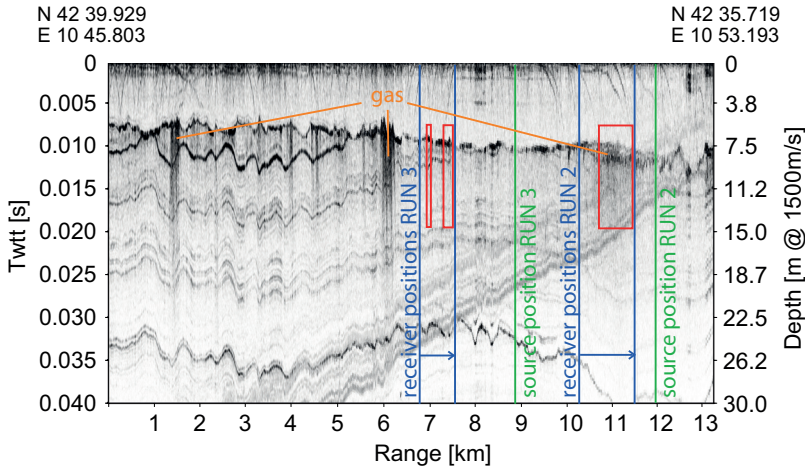


Figure 7.12: Locations of the geoacoustic inversion runs on top of the seismic profile of the AB transect as reproduced from Fig. 3.7(a). The red frames indicate regions with decreased sound speed estimates obtained from the geoacoustic inversion in Figs. 7.10 and 7.11.

are presented in Fig. 7.11. It should be noted that both runs cover different ranges r_{GPS} between the source and receiver⁵, leaving only a small window of 1550–1620 m for the actual comparison. Parameters estimated within this window are underlaid with gray boxes.

In both cases, the water depth, the sediment thickness, and both sound speeds show a consistent behavior, as already expected from the synthetic inversions (Ch. 6.2.2). Other parameters, such as densities and attenuations show a larger variation among adjacent positions and a trend could only be observed after averaging over approximately 30 m.

In general, inversion results for the two similar environments are in agreement. However, estimates differ in detail. Slight differences in the sediment thickness h_s and in the water depth h_w represent variations in the structure of the sea bottom that are also visible in the hydrographic data. Furthermore, sediment sound speed estimates reach two distinct levels, one at approximately 1460 m/s and the other around 1475 m/s. These values are obtained at both sites. However, the source–receiver range at which they appear differs. In the RUN 2 environment, low sediment sound speeds are observed at locations close to the source and high values are seen at ranges around 1600 m. For RUN 3 sediment sound speeds around 1600 m range are low, instead. They increase in the center part of RUN 3 and again reach the lower level around 1740 m range. Such a decrease in sound speed might be related to the presence of gas in the sediment. To further investigate this, a seismic profile, representative for the two locations, is considered for comparison. It is given in Fig. 7.12. In this figure, the particular source and receiver positions projected on the seismic transect are indicated and the regions for which low sediment sound speeds around 1460 m/s are found are highlighted by red frames. From the extended reflections in this seismic profile, large parts of the sea bottom at the site of RUN 2 are known to contain

⁵The source–receiver ranges are available from the two GPS antennas available at the NRV Leonardo, carrying the source, and the RHIB, carrying the receiver. Locations of the GPS antennas differ from those of the source and receiver. However, ranges r_{GPS} obtained from the GPS measurements are close to the exact ranges.

gas. These coincide with the low estimates of the sediment sound speed, marked by the red frames. This is not the case for RUN 3. No gas is seen in the seismic profile, while the sound speed is low at two different parts of the transect. However, while RUN 2 was performed on almost the same transect as covered by the seismic measurements, RUN 3 touches this transect only at its largest range. For shorter source–receiver ranges of RUN 3, the receiving array drifts further away from the seismic profile. Therefore, no evidence of the presence or absence of gas is available in the seismic profile for the RUN 3 location. Still, Fig. 7.12 shows that gas is present at several surrounding locations. Based on this and on the observations for RUN 2, it is concluded that also RUN 3 shows evidence of gas.

7.2.2 Environments with a thick sediment layer

The upper sediment layer of the MREA/BP'07 area shows a large variation in thickness, ranging from a few meters to several tens of meters. Environments treated so far have a considerably thin layer of soft sediments on top of an even finer subbottom. The current section is dedicated to the sediment layers with thicknesses of over 40 m, which are found in the shallow part of the trial area. Opposite to the high variability in sediment thickness, the variation of the sediment type throughout the trial area is rather small and both thin sediment layers as well as thick sediment layers are composed of fine grained sediments. Regardless of the prevailing grain size, the presence of a thick sediment layer poses an additional challenge to the inversions and might require an adaptation of both the environmental model and inversion strategy. Its influence on the inversion results is investigated in the following, employing data associated with RUN 5 and comparing the results to those of the RUN 2 and RUN 3 inversions as described in Ch. 7.2.1.

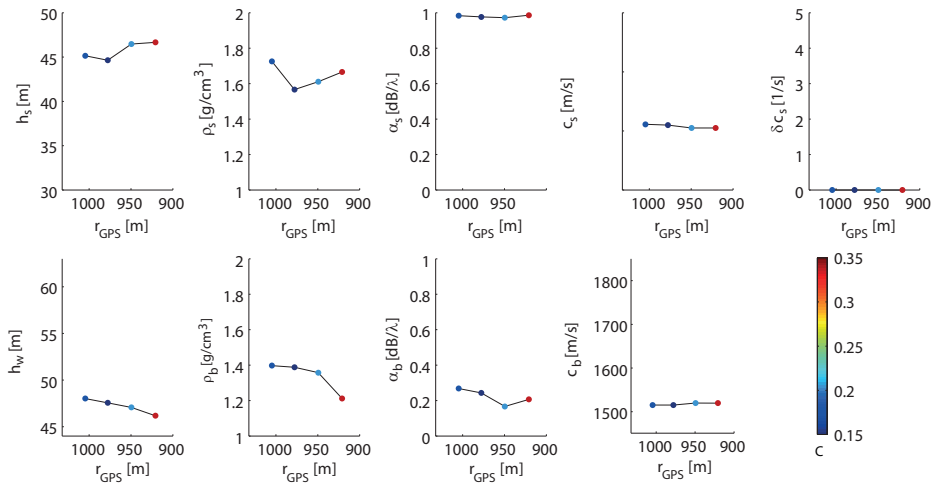


Figure 7.13: Results of the LF chirp inversions for RUN 5, using a constant sound speed in the sediment layer. The same parameters as in Fig. 7.10 are given, with the sound speed gradient set to zero. Colors indicate the costs of the best inversion result.

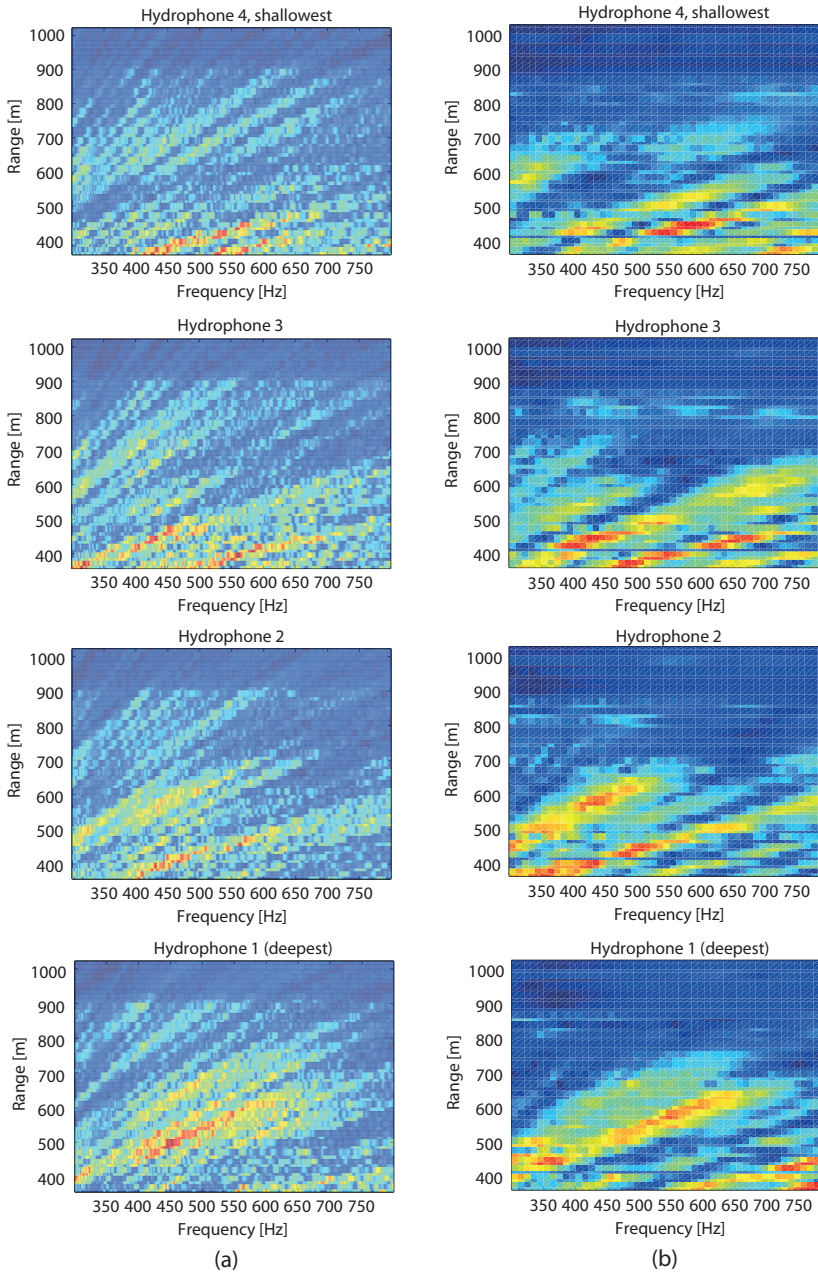


Figure 7.14: Measured (a) and inverted (b) pressure fields of RUN 5. In (b) the pressure field is modeled using the high values for the sediment attenuation as obtained from geoacoustic inversion ($\alpha_s \approx 1 \text{ dB}/\lambda$).

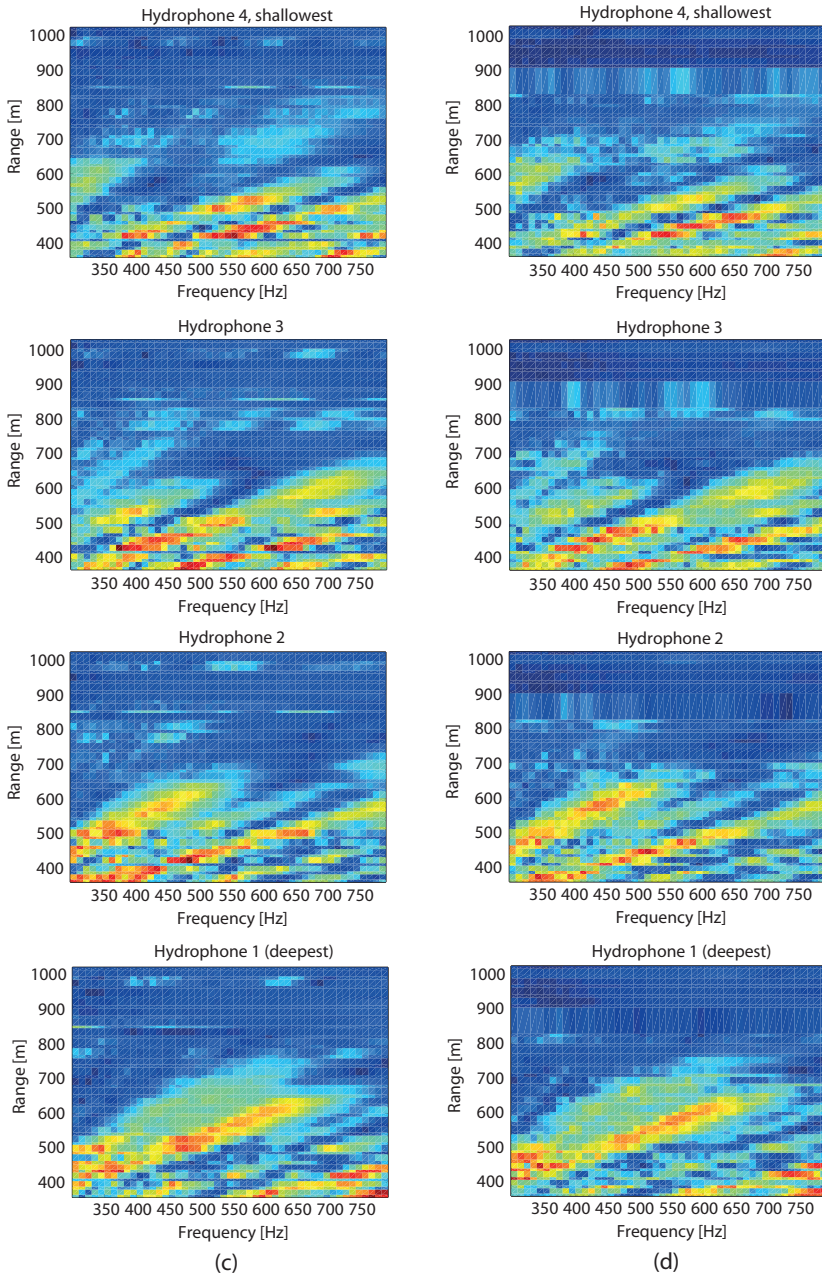


Figure 7.15: Inverted pressure fields of RUN 5. The pressure fields shown in (c) are modeled similarly to those in Fig 7.14(b), however with the attenuation kept constant at $\alpha_s = 0.2$. The basis for (d) forms an environmental model containing an additional virtual layer.

Due to the similarity in grain size⁶, results of RUN 2, 3, and 5 are expected to be similar at least for the parameters related to the sediment type, which are the density, attenuation, and sound speed. However, we have to note that the source–receiver ranges at the three sites differ. Especially, the RUN 5 data are obtained at very short ranges of less than 1000 m. This leaves us with another challenge since sufficient interaction with the sea bottom at these ranges is available at a small angular range, only. Subject to considerations in Appendix D.2.2 regarding these limitations, we finally decided to focus on the ranges larger than 900 m. Still, several issues were experienced in the inversion of the thick sediment layer at these ranges. They have been tackled from different directions, however, could not be fully solved, yet. In the following, the steps taken up to now are described. Further investigation and possible adjustment of the environmental model is needed.

The environmental model at locations with a thick sediment layer is adapted in terms of modeling the sediment sound speed. For environments with a thin layer of sediment, a gradient in the sediment sound speed is used. Such a gradient might be realistic for the upper part of a thick sediment layer as well. However, it might result in unrealistic high values, when continued throughout the entire sediment body. In the first instance, a constant sound speed is chosen for the entire sediment layer. The results of the inversion using a single constant sound speed are presented in Fig. 7.13. In order to still being able to account for depth dependent changes in the sound speed, a stepwise constant sound speed profile, consisting of two or more sound speed estimates, might be appropriate. Investigations toward this, however, could not reveal any benefits of such an extended model for the current dataset. Therefore, we concentrate on a single constant sound speed in the sediment layer.

Despite the short ranges, realistic estimates of the depth h_w and sediment thickness h_s are obtained from the inversions. Estimates of these two parameters, as given in Fig. 7.13, are similar to values observed from the hydrographic survey. Parameter estimates of the subbottom also show good results as can be seen in a comparison with the values obtained for RUN 2 and RUN 3 in Figs. 7.10 and 7.11. Other than the estimates at the two locations with a thin sediment layer, the estimates of the sediment sound speed c_s for the environment with a thick sediment layer lie just above the sound speed of water. According to [60], these are common values for silty clay environments as present at this location. Two other parameters of the sediment layer are particularly noticeable: the density ρ_s and the attenuation α_s . Density estimates of the sediment layer exceed those of the subbottom, indicating that further adaptations of the model are needed. Furthermore, the attenuation in the sediment layer reaches unnatural high values. These suggest only little interaction of the acoustic signals with the subbottom. However, this is not evident from the received matched-filtered signals in Fig. 7.9(c), which rather show strong late arrivals. Also the estimates at ranges above 700 m are affected by this high attenuation as can be seen from a comparison of the measured and modeled acoustic field in Fig. 7.14(a–b). Both, a lower attenuation and a higher sound speed are known to provide stronger returns. In an attempt to obtain a better match between the acoustic fields, the model has been recalculated using a more realistic attenuation in the sediment layer of $\alpha_s = 0.2$ dB/ λ . However, only little improvement of the modeled acoustic field could be obtained, as can be seen in Fig. 7.15(c).

⁶Grain sizes at these three locations range from 9ϕ to 11ϕ , only.

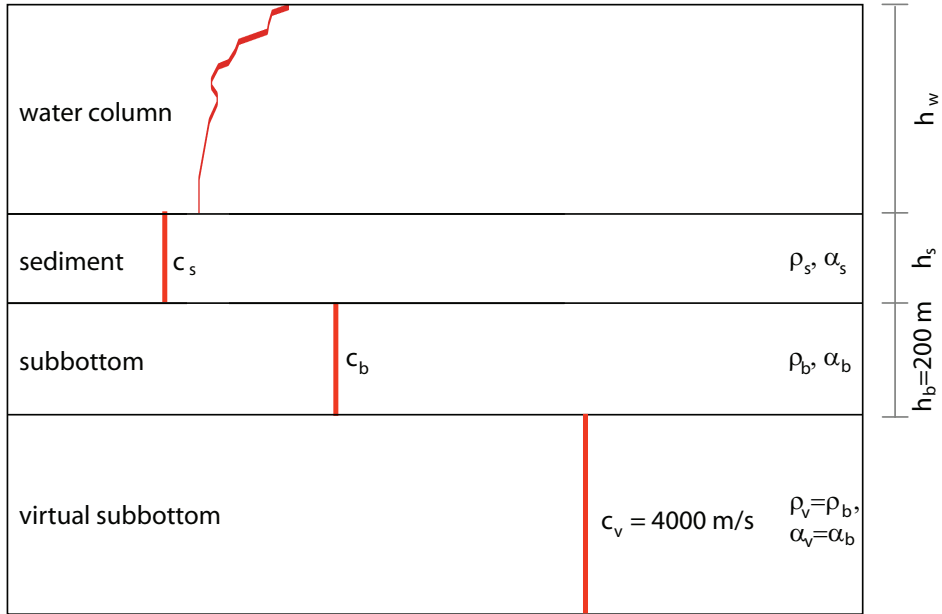


Figure 7.16: Schematic of the environmental model employing a virtual subbottom.

A better fit between the measured and modeled acoustic field might be obtained when a larger angular range at the source is accounted for. The angular range accounted for in the model is actually determined by the critical angle between the sediment layer and the subbottom, as described in Appendix D.2.2. For the current environment, this critical angle lies between 20° and 30° incident angle. Only angles below these values are considered in the model. Limitations in the angular range can be overcome by the introduction of a virtual subbottom with a large sound speed at a large depth. The actual subbottom is then treated as an additional layer, as schematized in Fig. 7.16. This, however, comes at the price of higher computational costs. The modeled acoustic field employing such a virtual subbottom is presented in Fig. 7.15(d). Again, only little improvement is seen. This might be due to the fact that, even when a virtual subbottom is applied, the estimates of the sediment attenuation are close to the upper search boundary of $1 \text{ dB}/\lambda$. Here, further research is required.

7.3 Conclusions

Despite the assumed additional uncertainty that is associated with real data, the inversion strategy chosen based on the synthetic results turned out to be valid for real data as well. Both, the amount of forward model calculations and the number of frequencies needed could be determined by fast synthetic inversions. However, when applying the same strategy to the real data, for most parameters averaging over a few subsequent estimates is needed to indicate a clear trend.

The optimal inversion strategy together with a 10-Hz sampling has then been applied to three environments. It is shown that a large number of parameters can be inverted for environments with a thin layer ($h_s < 10$ m) of soft sediments. The model employed, which is valid for grain sizes up to 9ϕ could be extended to grain sizes up to 11ϕ . Furthermore, differences in the sound speed estimates of only 15 m/s could be distinguished, which are assumed to be related to the presence of gas in the otherwise similar environments.

For environments with a thick sediment layer ($h_s > 45$ m), both the environmental description and the inversion strategy require adaptation. Here, the estimated parameter values apparently describe only a minor part of the full signal return since estimates of the attenuation are unrealistically high. Adaptations employed to the model so far could not solve this problem. Due to the short source–receiver ranges available for this specific situation, the application of a different model of the acoustic field such as a parabolic equation model might be helpful. Hence, further research is needed.

An integrated environmental picture – conclusions and perspectives

8

The objective of this thesis was to establish a three dimensional environmental picture that would improve the understanding of the influence of sediment properties on acoustic signals in shallow water. So far, various surveying and classification techniques have been analyzed, each performing well in a specific domain. The current chapter is meant to provide conclusions and recommendations on a possible combination of these techniques, yielding more information than the separate approaches.

8.1 A combined survey

The analysis of various methods for classifying sea bottom sediments, as presented in Chs. 4–7, has already indicated possible complementary aspects. Integrating their results into a three dimensional environmental picture of the sea bottom will not only give a better understanding of the acoustic behavior in certain environments, it will also allow concluding on how the different environmental descriptions can support each other. For efficiency reasons, an appropriate selection of the techniques to be combined is important. In the following, we highlight some aspects that are advisable to be considered in the selection process.

Hydrographic surveys performed by standard single- and multibeam echosounders, generally, employ frequencies in the range of a few tens to a few hundreds of kilohertz. These are highly attenuated by the sediment layer and, therefore, allow for sensing the upper few tens of centimeters of the sea bottom only. For the investigation of this upper part of the sea bottom, in a first instance, MBES data were chosen above SBES data. This decision was based on the larger coverage of the MBES and the fact that most of the variation in signal strength that is due to changes in sediment type is observed at grazing angles. Still, we have shown that signals from an SBES orientated in nadir direction are capable for classifying a variety of different sediment types, by focusing on their shape rather than on their amplitude. Moreover, the analysis of the SBES shape parameters and the MBES backscatter strength independently indicated the existence of the same number of acoustic classes. Although these acoustic classes cannot be linked directly, their distribution is in good agreement. This is confirmed by a correlation analysis, providing a correlation coefficient of 0.74, as documented in [63]. From this we can conclude that the classification results based on these two different echosounder systems are interchangeable, dependent on the data available. However, the classification results of the surficial part of the sediment layer are found to require supplementary information for interpretation. Taking sediment samples as ground truth is standardly applied. Here, we have shown that information on the occurrence of gas is equally important.

Seismic systems operating at a few kilohertz penetrate the sediment much further than

high-frequency echosounders. They provide information on the impedance contrast. This reveals interfaces between sediment layers, from which the layer thickness can be inferred. Also gas content, which decreases the sediment sound speed, can thus be extracted. While often used independently and for different purposes, we have shown that echosounders and seismic systems can complement each other. This is due to the fact that gas, which apparently affects the acoustic signals of both systems, is only indirectly visible in the echosounder signals. Basing the interpretation solely on the echosounder classification, the existence of gas might be mistaken for larger grain sizes. Combining both techniques could be realized under the same level of surveying efforts since low-frequency seismics and high-frequency echosounding can be performed simultaneously along the same tracks.

Beside standard hydrographic systems, also dedicated source–receiver systems for observing the acoustic pressure field have been employed. Geoacoustic inversion of the acoustic pressure field is a feasible means for providing detailed information on environmental parameters. Parameters that can be obtained in high quality are the water depth, sediment thickness, and the sound speed in both the sediment and subbottom. While geoacoustic inversion techniques are well suited for moderate sediment thicknesses, further research is needed on absorbing properties of large sediment deposits. In order to allow for a fast application at sea, sparse drifting arrays have been employed. In an attempt to compensate their lack in spatial information, a large number of frequencies has been considered. This, however, further increases the computational costs of the already demanding inversion techniques. To gain practical applicability, we aimed at reducing these costs, while still keeping an acceptable level of quality. It is shown that the efficiency of geoacoustic inversion methods can be improved by selecting an optimal inversion strategy and defining an optimal frequency range. Also employing an environmental picture for selecting areas with a similar acoustic behavior would be beneficial.

The environmental picture obtained is provided in Fig. 8.1. The colored areas represent the acoustic classes according to high-frequency systems (mainly MBES), interpolated over the area under study. The highest backscatter strength is given in red, followed by yellow, green, and blue for the lowest. The two- and three-colored regions indicate areas in which two or three types of acoustic classes occur next to each other on a small scale. Information obtained from grab samples is provided as a reference. The grabs are plotted as squares of different sizes and colors. While the size reflects the mean grain size, the color represents the sediment type according to Shepard (Fig. A.1). Also shown is the information extracted from the seismic profiles, which are the lines of equal sediment thickness and shaded areas indicating the presence of gas in both the sediment layer and/or subbottom. Due to sparse sampling, regions in which no gas is shown have to be assessed with caution. The three sites selected for geoacoustic inversion, here marked in red, are chosen such that they cover different aspects of the environment.

8.2 Interpretation of the environmental picture

An investigation of the environmental picture in Fig. 8.1 reveals no direct link between the acoustic classes and the bottom type or mean grain size, although the echosounder signals are known to contain information on the grain size. Instead, it is revealed that the echosounder signals contain more complex information on the environment. Figure 8.1 indicates an analogy between the presence of gas in the sediment and an increased MBES

backscatter strength, as already assumed in Ch. 5. Furthermore, information on structures of the seafloor are contained in the echosounder signals. We have shown the ability of the Bayesian approach (see Ch. 5), when applied to the MBES backscatter strength, to reveal these structures. In the environmental picture they form separate classes, indicating a distinct acoustic behavior. These classes are marked by two- or three-colored areas. For example, a regular structure, possibly related to the ocean current in the Ombrone estuary, is present in two-colored blue-green area of Fig. 8.1. It is revealed in both the slope map (Fig. 3.5) and the MBES backscatter classes (Fig. 5.5).

The consistency between the environmental characterization obtained from the MBES, SBES, and seismic measurements is such that we conclude that a combined map as presented in Fig. 8.1 can serve as a basis for subseafloor sediment classification techniques such as geoaoustic inversion. The inversion results are shown to be consistent for similar hydrographic classes at the single sites and, at the same time, variable with changes in the environment observed by the hydrographic survey. Especially, sediment sound speed estimates showed a high correlation with the gas found in the sediment body. Gas patches could be resolved with about the same order of detail as in the seismic profiles. However, due to limitations in time and resources, an agreement between the classification based on the hydrographic survey and the inversion results could be confirmed only for a small part of the MREA/BP'07 area. Here, a similar investigation for additional locations is needed.

So far the following can be concluded: the variability of the inversion results (Figs. 7.10, 7.11, and 7.13) within a single acoustic class (Fig. 8.1), found from the hydrographic survey, is mainly due to variations in the gas content, the water depth, and the sediment thickness. All three have to be accounted for when choosing locations for geoaoustic inversion based on a hydrographic survey.

8.3 Perspective

The combined approach presented for environmental classification and mapping is in principle directly applicable. However, some issues need to be addressed in future work. Model-based classification approaches need to be extended for both very small and very large grain sizes by establishing empirical relations between these grain sizes and acoustic propagation effects. Furthermore, including empirical relations for the acoustic behavior in gaseous environments is highly recommendable. Additional investigations of other non-standard environments are also needed. Especially, the effect of thick sediment layers on the geoaoustic inversion results requires further research.

The classification approaches presented in this thesis are mainly based on standard sediment classes as defined, for example, in the nomenclature of Wentworth (see App. A). However, offshore industry has a major interest in particular grain sizes. For this purpose, analyzing the possible refinement of the standard sediment classes would be of interest. In principle, a refinement of the acoustic classes is possible. Whether these sub-classes indeed can be related to refined sediment grain sizes needs further investigation. For this purpose, it is recommendable to support the SBES or MBES data with additional information on the sediment, as obtained from the seismics. This would allow for a correct interpretation of the acoustic signal and consequently for a correct derivation of mean grain size.

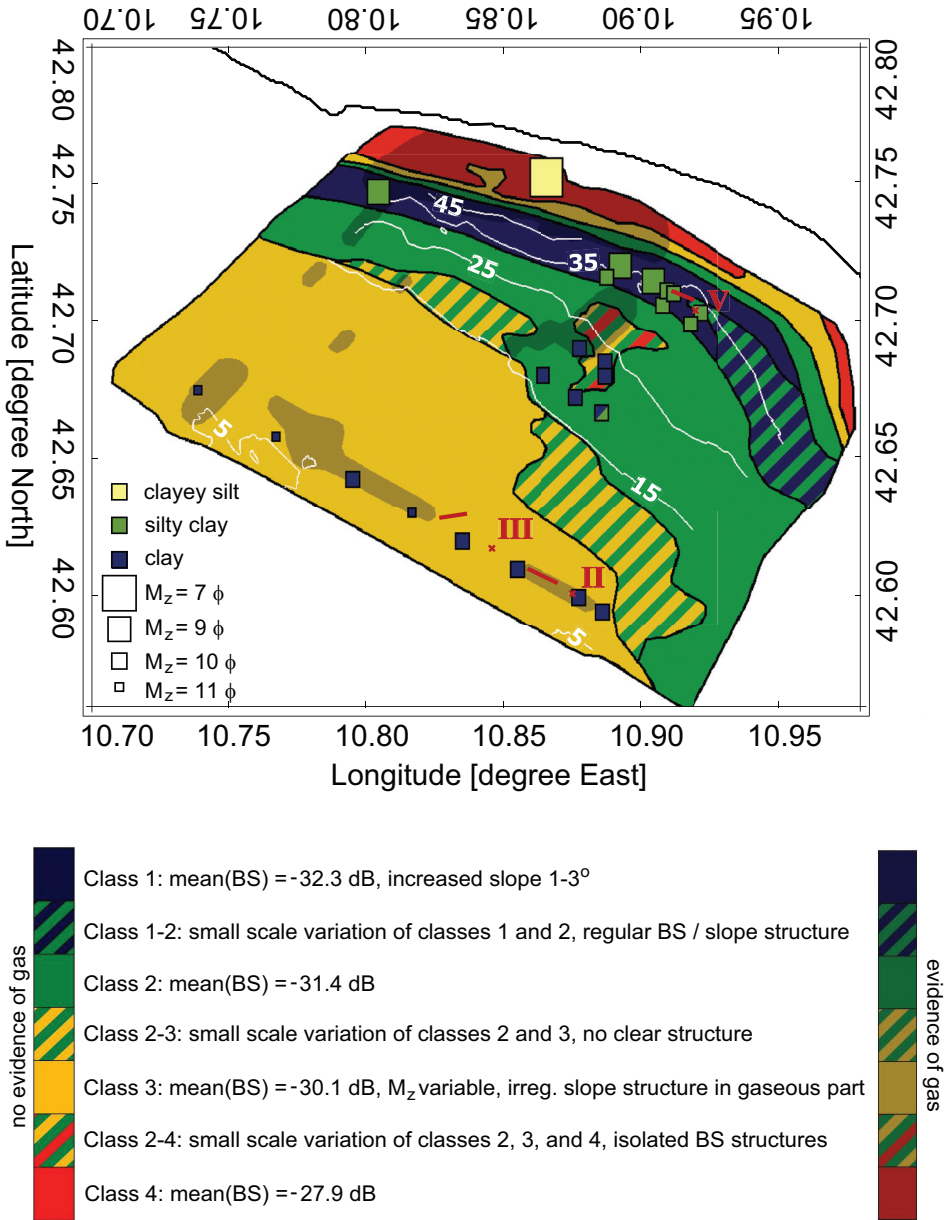


Figure 8.1: Environmental picture of the MREA/BP07 area obtained by merging the results from different devices (MBES, SBES, and seismic). Colors indicate the high-frequency acoustic classes. Shaded regions indicate the presence of gas, as deduced from seismic profiles. The sediment thickness, also obtained from the seismics, is given as lines of equal thickness (white lines) in steps of 10 m, starting at 5 m. Furthermore, the sites at which geoacoustic inversion is applied are marked in red. Squares represent the grab samples, providing the mean grain size (size) and sediment type (color).

A

Sediment characteristics

Sediment properties are commonly determined by analyzing samples. In classic sediment classification, sediment types are distinguished by a large quantity of versatile criteria, describing both the properties of single grains and their grain-to-grain relation within the sediment body [64]. Most of these criteria are optically differentiable, such as texture and color of the sediment matrix. However, some of these parameters are also captured by sound and are therefore relevant for acoustic sediment classification. Basically, the parameters of interest are the particle size and composition. In case of sound penetrating deeper than a few centimeters into the sediment body also bulk properties become important.

A.1 Sampling and analysis

Sea bottom sediments are either collected in form of grab or core samples. Whereas grab samples, for example taken by a Hamon or Van der Veen grabber, collect sediments from the upper few tens of centimeters only, core samples provide insight into the deeper sediment body. Cores, contrary to grab samples, preserve the structure of the sea bottom. This enables the identification of sediment layers and the determination of bulk properties. The standard property obtained from both grab and core samples, however, is the sediment composition.

For obtaining the sediment composition, the laboratory analysis of the bottom material, in general, comprises the following steps. First, the samples are dried. Then, they are sieved in order to separate the gravel and shells from the finer material. Both the gravel and shell weight percentage are subsequently determined. For the remaining material, the precise grain size distribution, as further described in A.2, is determined by optical microscopy. From these, sediment types can be determined.

A.2 Sediment type definitions

A standard criterion to discriminate between different types of sediments is their grain size. Grain size is either given in millimeter or ϕ units, which are related according to

$$d = -\log_2 D. \quad (\text{A.1})$$

Here, D denotes the grain diameter in millimeters and d is the corresponding value in ϕ units. For the description of the different grain sizes, we follow the nomenclature of [65], as given in Table A.1.

In general, sea bottom sediment material is a composite. Hence, different grain diameters are present, even at a single location. Therefore, often a mean grain size (M_z),

Table A.1: Sediment grain sizes according to Wentworth [65].

d [ϕ]	maximum diameter [mm]	sediment
-1-0	2	very coarse sand
0-1	1	coarse sand
1-2	1/2	medium sand
2-3	1/4	fine sand
3-4	1/8	very fine sand
4-8	1/16	silt
8-10	1/256	clay
>10	1/1000	colloid

derived from the grain size distribution, is referred to. Different definitions of mean grain sizes exist, relating M_z to one or more thresholds d_p for grain diameters. A threshold d_p indicates the grain size in ϕ -value at which $p\%$ of the grains are smaller by weight.

The simplest definition of M_z is given by the d_{50} value of the sediment composition, which is the median diameter. Other conventional definitions average over different values d_p , weighted by factors a_p where appropriate.

$$M_z = \frac{\sum_p a_p d_p}{\sum_p a_p} \quad (\text{A.2})$$

Folk [66], for example, suggested the unweighted average of the d_{16} , d_{50} , and d_{84} thresholds, as given in Eq. A.3.

$$M_z = \frac{d_{16} + d_{50} + d_{84}}{3} \quad (\text{A.3})$$

Similar definitions are given in [67] or are applied by [16].

For describing sediment compositions, Folk also introduced a nomenclature based on the ratios of gravel, sand, and mud. They are presented in the ternary diagram of Fig. A.1(a), reproduced from [68]. Several extensions for the small grain sizes exist [64, 69], based on the ratios of sand, silt, and clay. We follow the one recommended by [69], as documented in the ternary diagram of Fig. A.1(b). These grain ratios can be related to M_z values by empirical relations, as given in [40].

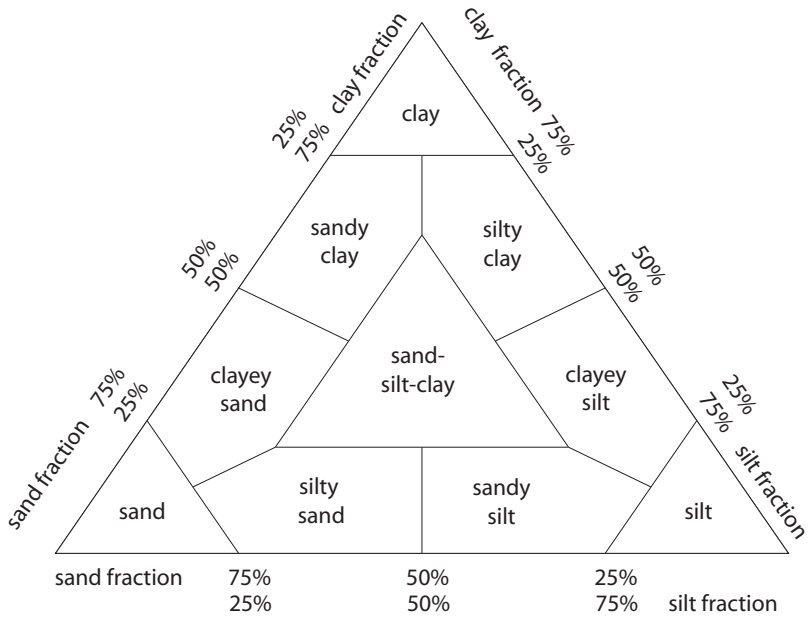
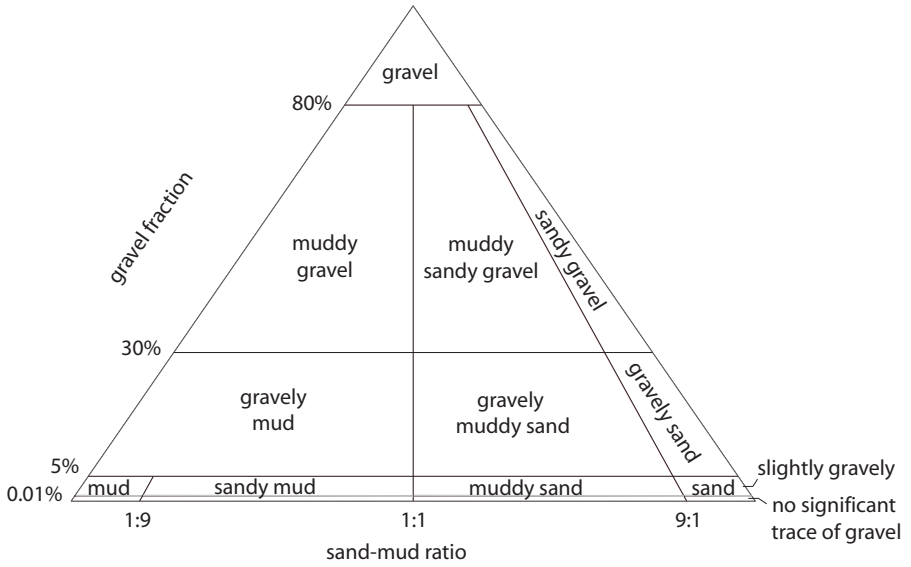


Figure A.1: Grain ratios. (a) Gravel-sand-mud ratio according to Folk.[68] (b) Sand-silt-clay ratio according to Shepard.[69]

A.3 Sediment properties affecting acoustic signals

Beside grain size, a large number of related parameters affect sound propagation. These parameters are either roughness-related properties or bulk properties, such as porosity, density, sound speed of the compressional and shear waves⁷, and the reflection coefficient, as listed in [1]. Following [1], the relation between mean grain size and other bulk properties is given in Table A.2. Here, we focus on those properties which are input to the acoustic models employed in this thesis: the density ρ_s , the compressional speed c_s , and the attenuation α_s . Instead of providing a single value for the expected order of magnitude as given in [1], we roughly indicate parameter ranges adopted from [60–62].

Table A.2: Relation between mean grain size and other bulk properties, derived from [60–62].

M_z [ϕ]	ρ_s [g/cm^3]	c_s [m/s]	α_s [dB/ λ]
1	1.95-2.15	1800-1880	0.468–1.090
2	1.90-2.15	1740-1840	0.487–1.104
3	1.70-2.05	1640-1820	0.607–1.310
4	1.65-2.00	1600-1750	0.896–1.453
5	1.50-1.95	1560-1720	0.312–1.376
6	1.35-1.90	1530-1650	0.138–0.561
7	1.30-1.75	1510-1600	0.076–0.320
8	1.25-1.70	1490-1560	0.060–0.265
9	1.15-1.65	1480-1540	0.044–0.231
10	1.15-1.55	1470-1530	0.044–0.229

⁷Shear waves are not accounted for since we treat the sediment layer as a fluid (see Appendix C).

Previous samples taken in the research areas

B

B.1 Sediments in the MREA/BP'07 area

The MREA/BP'07 area has already been in the focus of several former experiments. From these, a collection of core samples is available, supplementing the information on the sediment distributions obtained from the recently taken grab samples (Ch. 3.1.3). The core locations and according sediment profiles are displayed in Fig. B.1. Even if taken at different times and outside the MREA/BP'07 area, the cores are still seen to be representative for the entire area. In the upper part, the profiles show similar distributions as evident from the grab samples. Sediments mainly consist of portions silt and clay, with a tendency toward increased clay fractions in regions with a larger water depth, whereas silt dominates in the shallower parts. Cores in the vicinity of others show only slight variations in their content. Most profiles are consistent throughout the different heights in the sediment body. Only a few profiles show additional sand fractions in their lower parts.

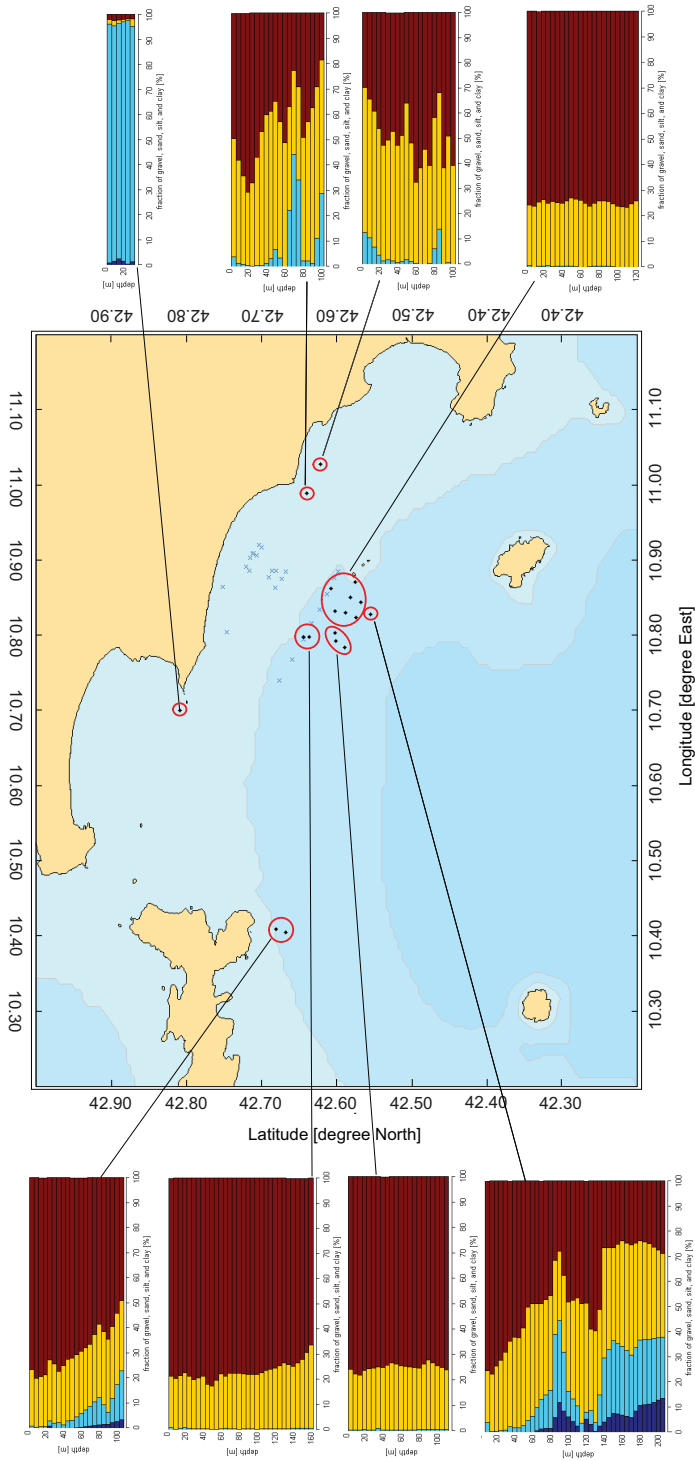


Figure B.1: Overview over historic cores in the MREA/BP'07 area. Historic core positions are depicted as black dots. Furthermore, blue crosses give the positions of grabs, taken during the MREA/BP'07 experiment as displayed in Fig. 3.6 of Ch. 3.1.3. Similar core samples have been grouped. Per region, a representative profile of gravel–sand–silt–clay ratios, obtained from core sampling, is presented. Corresponding colors of these profiles are dark blue, light blue, yellow, and red for the grain sizes gravel, sand, silt, and clay, respectively.

B.2 Sediments in the CBBC'04 area

No cores are available for the CBBC'04 area. Instead, a geological map is presented in Fig. B.2, which was taken from [34]. Currently available data from the CBBC'04 experiment comprise the legs 3–6 in Fig. B.2. The large variety of sediment types indicated by the grab samples taken in 2000 (Ch. 3.2.3) is confirmed by this map. Furthermore, it is seen that no large variations occurred in the area under investigation. It can thus be concluded that both the geological map and the grab samples are still representative for the experiment conducted in 2004.

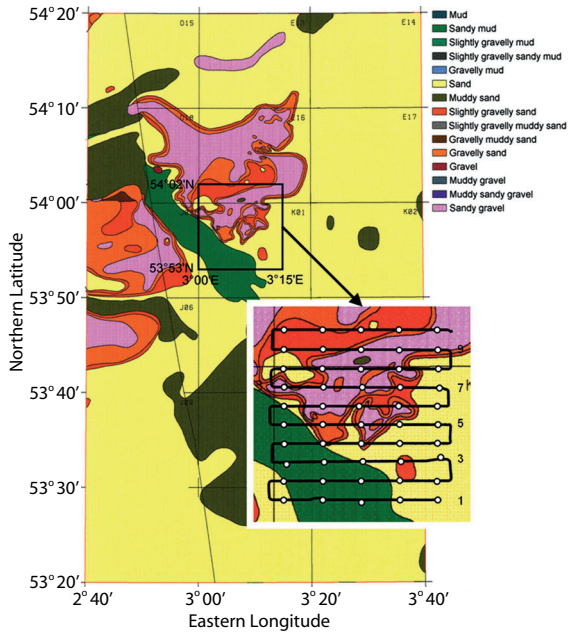


Figure B.2: Overview of the sediment Folk classes in the trial area, taken from [34].

Environmental models

Propagating sound is influenced by the properties and boundary conditions of the medium, also referred to as the acoustic waveguide, it is traveling through. Media relevant for underwater sound propagation are the water column⁸ and sediment body. For sea bottom classification, especially the sound interactions with the water–sediment interface and sediment body are important.

Numerous empirically derived environmental models exist that describe sound interaction with these parts of the underwater environment. These models mainly differ in the degree of detail accounted for. The choice of an adequate environmental description depends on the frequency employed, which is directly related to the resolution. A higher frequency entails a higher resolution, requiring a more detailed model.

Propagation concepts used throughout this thesis are briefly described in the following. They have been adopted from [1, 40, 70–72].

C.1 Sound propagation in the water column

The direction in which sound propagates is mainly influenced by the sound speed and, of course, the angle under which it is sent. Often, a standard value of 1500 m/s is used for describing the sound speed in sea water. However, this is not always sufficient for precise applications of underwater acoustics. Sound speed shows strong variations over depth. Additionally, regional and annual variations occur. Empirical relations of different complexity that couple water column sound speed to pressure (or depth h_w), temperature t_w , and salinity s_w are given for example by Medwin.

$$c_w = 1449.2 + 4.6t_w - 0.055t_w^2 + 0.00029t_w^3 + (1.34 - 0.01t_w)(s_w - 35) + 0.017h_w \quad (\text{C.1})$$

Changes in sound speed cause refraction. This principle is described by Snell's law for incoming sound under an angle θ_1 in a region with sound speed c_1 that changes direction into θ_2 when penetrating a layer with different sound speed c_2 .

$$\frac{\cos \theta_1}{c_1} = \frac{\cos \theta_2}{c_2} \quad (\text{C.2})$$

⁸The sound source is commonly placed in the water column. Exceptions, such as underwater acoustics based on aircraft noise or the use of buried sources is not treated here.

C.2 Sound interaction with the water–sediment interface and sediment body

Due to the saturation of the sediment with water, the sediment layer is treated as a fluid layer. This restricts acoustic propagation to primary (compressional) waves.

At the water–sediment interface the acoustic impedance changes, due to the differences in sound speed and density. Dependent on the frequency of the acoustic signal, part of it is transmitted into the sediment body whereas the remainder is either reflected or scattered at the water–sediment interface. This behavior is determined by the roughness of the seafloor. A smooth, flat bottom will cause part of the acoustic signal to reflect, whereas a rough bottom will cause scattering. In general, small-scale roughness with dimensions in the order of the acoustic wavelength $\lambda = \frac{c}{f}$ or less causes scattering. Objects larger than the wavelength, on the other hand, cause reflections. This means that at low frequencies scattering becomes less important and the sediment body is often modeled as a layered medium with an impedance contrast between two adjacent layers, whereas models accounting for scattering are dominant at high frequencies.

Reflection theory comprises the reflection of a part of the signal and the transmission of the remainder. How much of the signal is penetrating into the sediment is dependent on the frequency and the angle of incidence and is described by the reflection coefficient R and the transmission $1 + R$. In general, the reflection coefficient is determined by

$$R = \frac{\rho_2 c_2 \sin \theta_1 - \rho_1 c_1 \sin \theta_2}{\rho_2 c_2 \sin \theta_1 + \rho_1 c_1 \sin \theta_2}. \quad (\text{C.3})$$

Due to the presence of sound speed differences, the transmitted signal is refracted according to Snel's law (Eq. C.2). In cases where the sound speed of the underlying medium is higher, a critical angle of incidence θ_c exists up to which total reflection ($R = 1$) holds. This critical angle is defined by

$$\theta_c = \arccos \frac{c_1}{c_2}. \quad (\text{C.4})$$

In cases where the sound speed of the underlying medium is lower and where $\rho_2 c_2 > \rho_1 c_1$ holds, additionally, an angle of intromission θ_0 exists, at which no reflection occurs ($R=0$). The angle of intromission is defined by

$$\theta_0 = \arctan \sqrt{\frac{1 - \left(\frac{c_2}{c_1}\right)^2}{\left(\frac{\rho_2 c_2}{\rho_1 c_1}\right)^2 - 1}}. \quad (\text{C.5})$$

In cases where the assumption of an ideal flat bottom is no longer sufficient, the part of the signal not penetrating into the sediment layer is modeled as being scattered. A simple model for scattering is Lambert's law. According to Lambert's law, the strength of a scattered signal that was sent under a certain angle θ^* and is received under the same angle becomes

$$S_{b\text{Lambert}}(\theta^*) = 10 \log_{10} \mu + 10 \log_{10} \sin^2 \theta^*, \quad (\text{C.6})$$

with μ being the bottom scattering constant and $\theta^* = 90^\circ - \theta$ the grazing angle of incidence. S_b is also referred to as the backscatter strength.

C.2 Sound interaction with the water–sediment interface and sediment body 107

Table C.1: Model parameters of the backscatter cross section and their symbols.

Parameter	Symbol
Sediment - water ratio of mass density	ρ
Sediment - water ratio of sound speed	ν
Imaginary to real wave number ratio	δ
Exponent of the bottom relief spectrum	γ
Strength of the bottom relief spectrum [cm ⁴]	w_2
Sediment volume scattering cross section to attenuation coefficient ratio	σ_2

More detailed models account for variations in the backscatter strength dependent on the grain size and angle. The model described in [40], which is used throughout this thesis, additionally distinguishes between the backscatter cross section due to interface roughness scattering σ_r and the one due to volume scattering σ_v . The total scattering cross section σ_b is then expressed as

$$\sigma_b(\theta^*) = \sigma_r(\theta^*) + \sigma_v(\theta^*). \quad (\text{C.7})$$

The backscatter strength, which is the decibel equivalent of the scattering cross section, reads

$$S_{b\text{APL}}(\theta^*) = 10 \log_{10}(\sigma_b(\theta^*)). \quad (\text{C.8})$$

This model involves six environmental parameters to determine σ_r and σ_v , which are listed in Table C.1. The backscatter cross section due to interface roughness scattering σ_r is obtained by appropriate combination and interpolation of the three following approximations:

- (1) the Kirchhoff approximation σ_{kr} ,
- (2) the composite roughness approximation σ_{cr} , and
- (3) the large-roughness scattering with a scattering cross section σ_{lr} .

The Kirchhoff approximation and composite roughness approximation are both valid for smooth to moderately rough sediments up to sand-sized grains (< 2 mm, see Table A.1). However, they cover different angular ranges. Approximating the scattered field by perfect reflection restricts the validity of the Kirchhoff approximation to angles close to nadir. In praxis, σ_{kr} is set to zero for angles of incidence smaller than 40°. For these grazing angles, σ_{cr} is used instead. This composite roughness approximation incorporates a shadowing correction $S(\theta^*, s)$ and a slope averaging integral $F(\theta^*, \sigma_{pr}, s)$, with s being the root mean square slope and σ_{pr} a small-roughness perturbation approximation of the roughness scattering cross section. An interpolation of σ_{kr} and σ_{cr} describes the medium-roughness scattering, which is combined with the large-roughness scattering to determine σ_r . The cross section of the large-roughness scattering σ_{lr} is calculated from an empirical expression which is derived for rough sediments like gravel and rock (grain sizes > 2 mm).

The description of the backscatter cross section due to volume scattering σ_v , as given in [40], is factorized similar to the composite roughness approximation, containing a shadowing correction $S(\theta^*, s)$ and a slope averaging integral $F(\theta^*, \sigma_{pv}, s)$. Here, σ_{pv} describes the following approximation of the volume scattering cross section.

$$\sigma_{pv}(\theta^*) = \frac{5\delta\sigma_2 |1 - R^2(\theta^*)|^2 \sin^2(\theta^*)}{\nu \ln 10 |P(\theta^*)|^2 \text{Im}\{P(\theta^*)\}} \quad (\text{C.9})$$

The parameters comprised are listed in Table C.1. Here, Im denotes the imaginary part. Further, the reflection coefficient R is given in Eq. C.3 and P can be expressed as

$$P = \sqrt{\kappa^2 - \cos^2 \theta^*}, \text{ with} \quad (\text{C.10})$$

$$\kappa = \frac{1}{\nu}(1 + i\delta) \quad (\text{C.11})$$

For more details we refer to [40].

Typical empirical parameter values for grain sizes between -1ϕ and 9ϕ are given in Table C.2. Employing these values to determine σ_r and σ_v provides a distinct and angular dependent model description of the backscatter strength for these grain sizes (Eq. C.8). Figure C.1 gives an extraction of the model results.

In general, the backscatter strength decreases from nadir direction to grazing angles. This is also reflected in the model, as can be seen from Fig. C.1. Additionally, a variation of the backscatter strength related to the grain size is included in the model. As expected, smoother bottoms are modeled such that a large part of the intensity is reflected away from the incoming direction at grazing angles. For larger grains, which are generally associated with a rougher surface, the backscatter strength is larger than for soft sediments at these grazing angles. The opposite, however, does not hold for all grain sizes at angles close to nadir. Still, a rougher surface, results in larger roughness scattering, reducing the backscatter strength close to nadir for the larger grain sizes. For mean grain sizes $M_z = -1\phi$ to $M_z = 5\phi$, this is the dominating factor. Therefore, the backscatter strength close to nadir increases from $M_z = -1\phi$ to $M_z = 5\phi$. At smaller grains, the difference in roughness scattering is less pronounced. Instead, scattering of the compact volumes becomes more important, again, directing large parts of the energy away from nadir and resulting in lower backscatter strengths.

Table C.2: Empirical values of the model parameters.

$M_z [\phi]$	$\rho [-]$	$\nu [-]$	$\delta [-]$	$\gamma [-]$	$w_2 [\text{cm}^4]$	$\sigma_2 [-]$
-1.0	2.492	1.337	0.0171	3.25	0.0129	0.002
0.0	2.314	1.278	0.0163	3.25	0.0086	0.002
1.0	2.151	1.224	0.0165	3.25	0.0056	0.002
2.0	1.615	1.140	0.0161	3.25	0.0035	0.002
3.0	1.339	1.080	0.0173	3.25	0.0021	0.002
4.0	1.223	1.036	0.0202	3.25	0.0011	0.002
5.0	1.169	1.000	0.0126	3.25	0.0005	0.002
6.0	1.149	0.987	0.0039	3.25	0.0005	0.001
7.0	1.147	0.985	0.0024	3.25	0.0005	0.001
8.0	1.146	0.982	0.0016	3.25	0.0005	0.001
9.0	1.145	0.980	0.0015	3.25	0.0005	0.001

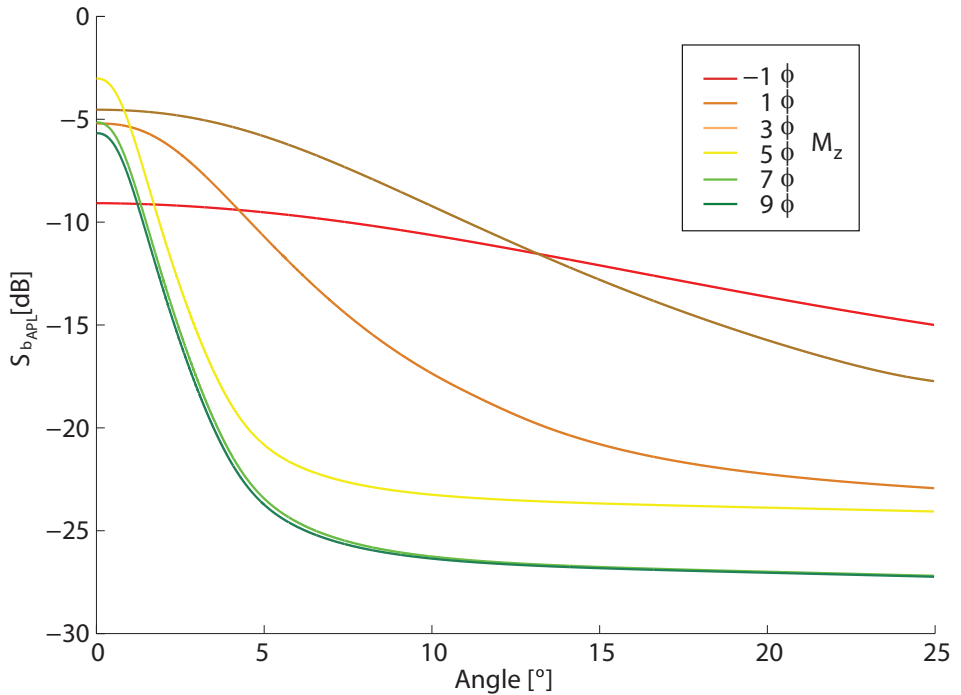


Figure C.1: Backscatter strength modeled according to [40], accounting for the interface roughness scattering and volume scattering.

D

Modeling the acoustic field

The propagation of sound within the acoustic field results in pressure changes, which are described by the acoustic wave equation. Environmental conditions under which this wave equation has to be solved are often described by empirical relations (see App. C) and are included in terms of boundary conditions. [73]

The acoustic wave equation is a second order partial differential equation which is derived from the basic equations of physics: the equations of continuity, motion, and state. [70] It is often expressed in its linear, homogeneous form as

$$\nabla^2 p(\vec{x}, t) - \frac{1}{c^2} \frac{\partial^2 p(\vec{x}, t)}{\partial t^2} = 0. \quad (\text{D.1})$$

Here, p is the unknown pressure in the acoustic field of a sound wave traveling at speed c , at a location \vec{x} and time t . Further, ∇ is the Nabla operator and ∂ describes the partial differential operator. Equation D.2 is the simplest form of the wave equation in an environment with constant density. In case of a spatially variable density ρ , which is common for a layered medium such as an underwater environment, the homogeneous wave equation rather becomes

$$\rho \nabla \cdot \left(\frac{1}{\rho} \nabla p(\vec{x}, t) \right) - \frac{1}{c^2} \frac{\partial^2 p(\vec{x}, t)}{\partial t^2} = 0. \quad (\text{D.2})$$

In active acoustics, additionally, a source term $f(\vec{x}, t)$ has to be accounted for, representing the mass injected by the source at a location \vec{x} . This leads to the inhomogeneous form of the wave equation.

$$\rho \nabla \cdot \left(\frac{1}{\rho} \nabla p(\vec{x}, t) \right) - \frac{1}{c^2} \frac{\partial^2 p(\vec{x}, t)}{\partial t^2} = f(\vec{x}, t) \quad (\text{D.3})$$

Several techniques exist for solving this differential equation to determine p , under which methods using ray tracing, parabolic equations, wave number integration, normal modes, or finite elements. Each of these techniques has its strengths and weak points, making it the most applicable within specific boundaries. Main selection criteria are the distance between source and receiver, the frequencies employed, and whether the environment is treated as range dependent or independent. Also efficiency is important.

In the following, a brief overview over these techniques and their field of application is given. This information is gathered from [71, 73]. Further, the normal modes model, used throughout this thesis, is described in more detail.

D.1 Solving the acoustic wave equation

Solving the wave equation (Eq. D.3) directly is only possible by discretization of either the wave equation (*Finite Difference Method*) or the environment (*Finite Element Method*). Both methods are most general; they can deal with inhomogeneous environments, complex geometries, and scattering. This, however, comes at the price of time-consuming calculations. To gain numerical efficiency, Eq. D.3 is often simplified through assumptions and approximations, thereby losing part of the generality. A common step is the Fourier transform to a time-independent Helmholtz equation. [71]

$$\rho \nabla \cdot \left(\frac{1}{\rho} \nabla p(\vec{x}, \omega) \right) + k^2 p(\vec{x}, \omega) = f(\vec{x}, \omega) \quad (\text{D.4})$$

Here, $k^2 = \frac{\omega^2}{c^2(\vec{x})}$ is the wave number and ω is the radial frequency.

Techniques for solving the Helmholtz equation either involve ray- or wave theory, dependent on the frequency employed. Ray theory is better suited for high frequencies, whereas wave theory is rather applied to low frequencies.

Models based on ray theory use *Ray Tracing* to determine the phase changes in the acoustic field. For this purpose, amplitude and phase components are separated in Eq. D.4. Ray tracing methods are fast and able to deal with range dependent environments. However, they have a lower accuracy and do not account for the source term.

Models based on wave theory include *Wavenumber Integration Techniques (Fast Field Programs)*, *Normal Modes*, and *Parabolic Equations*. *Wavenumber Integration Techniques* provide a numerical solution of the acoustic field integral, whereas *Normal Modes* further reduce the integral to a sum of residues. Both techniques are, in general, designed for range independent environments, however, can be extended to variable environments. *Parabolic Equations*, which provide an alternative approximation to the wave equation, also can cope with range dependent environments.

D.2 Normal mode modeling

Normal mode modeling is based on the assumption of a cylindrically symmetric acoustic field. Instead of using three-dimensional Cartesian coordinates, the acoustic pressure at each location can then be expressed as a function of depth z and range r , only.

$$p(\vec{x}) \rightarrow p(z, r) \quad (\text{D.5})$$

In the following, the source is assumed to be isotropic and located at $r_0 = 0$ and $z_0 = h_{\text{source}}$, with h_s being the source depth. Adding such a source to the cylindrically symmetric acoustic field and utilizing the fact that the acoustic field must have the same harmonic time dependence as the source, we obtain the following expression of the Helmholtz equation.

$$\frac{\partial^2 p}{\partial r^2} + \frac{1}{r} \frac{\partial p}{\partial r} + \frac{\partial^2 p}{\partial z^2} - \frac{1}{\rho} \frac{d\rho}{dz} \frac{\partial p}{\partial z} + k^2 p = -\frac{\delta(r)\delta(z-z_0)}{2\pi r} \quad (\text{D.6})$$

Using the concept of separation of variables, the pressure p is expressed as a product of the functions $\Phi(z)$ and $\Theta(r)$, describing the depth- and range dependency, respectively. [59]

$$p(r, z) = \Theta(r)\Phi(z) \quad (\text{D.7})$$

Replacing p in the homogeneous form of Eq. D.6 by this product, leads to the following two differential equations.

$$\frac{d^2\Theta}{dr^2} + \frac{1}{r} \frac{d\Theta}{dr} + a\Theta = 0 \quad (\text{range dependent}) \quad (\text{D.8})$$

$$\frac{d^2\Phi}{dz^2} - \frac{1}{\rho} \frac{d\rho}{dz} \frac{d\Phi}{dz} + (k^2(z) - a)\Phi = 0 \quad (\text{depth dependent}) \quad (\text{D.9})$$

Here, a denotes the unknown separation constant. The depth dependent equation (Eq. D.9) is also denoted as modal equation. It has an infinite number ($n = 1, \dots, \infty$) of solutions $\Phi = \Phi_n$ for distinct values $a = a_n$.

In order to determine these solutions for the specific case of an underwater environment as defined in Fig. D.1, we consider the following mixed Dirichlet-Neumann boundary conditions.

$$\Phi(0) = 0 \quad (\text{D.10})$$

$$\frac{d\Phi}{dz}(h_t) = 0 \quad (\text{D.11})$$

These boundary conditions describe a pressure release boundary at the sea surface ($z = 0$) and a perfect rigid boundary at sufficiently great depth $z = h_t$, respectively. The depth at which the lower boundary is placed is chosen as $h_t = h_w + h_s + h_b$, dependent on the water depth h_w , the sediment thickness h_s , and an assumed thickness of the subbottom h_b , as depicted in Fig D.1. The modal equation (Eq. D.9) together with the boundary conditions (Eqs. D.10 and D.11) poses a Sturm-Liouville eigenvalue problem. This can be seen by introducing the operator L as

$$L = \frac{d^2}{dz^2} - \frac{1}{\rho} \frac{d\rho}{dz} \frac{d}{dz} + k^2(z). \quad (\text{D.12})$$

Eq. D.9 then becomes

$$L\Phi(z) = a\Phi(z), \quad (\text{D.13})$$

with a containing the monotone sequence of eigenvalues $a_n = k_n^2$ and Φ containing the corresponding eigenfunctions Φ_n . Since the eigenfunctions form a complete orthonormal set, the solution of the modal equation can be expressed as

$$p(r, z) = \sum_{n=1}^{\infty} \Theta_n(z) \Phi_n(z). \quad (\text{D.14})$$

The solutions Θ_n are then determined analytically, dependent on the eigenfunctions Φ_n . By inserting Eq. D.14 into the inhomogeneous Eq. D.6, we obtain

$$\Theta_n(r) = \frac{i}{4\rho(z_0)} \Phi_n(z_0) H_0^{(1)}(k_n r), \quad (\text{D.15})$$

with $H_0^{(1)}$ the zeroth order Hankel function of the first kind.

Derived from Eqs. D.14 and D.15, the normal mode solution of the acoustic pressure field then becomes

$$p(r, z) = \frac{e^{\frac{i\pi}{4}}}{\rho(z_0)\sqrt{8\pi r}} \sum_{n=1}^{\infty} \Phi_n(z_0) \Phi_n(z) \frac{e^{ik_n r}}{\sqrt{k_n}}. \quad (\text{D.16})$$

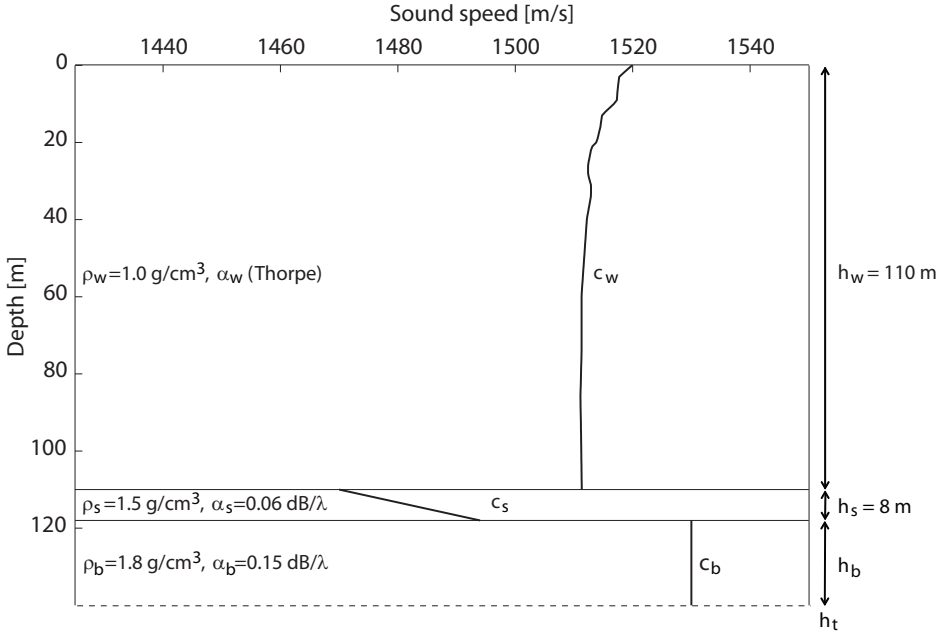


Figure D.1: The range-independent environment employed for normal modes modeling. The environment consists of three layer, the water column, the sediment layer, and the subbottom halfspace. For modeling purposes, a perfect rigid boundary at sufficiently great depth h_t is inserted. Further, the sound speed profile c , the density ρ , and the attenuation α are given for each of the three layers.

D.2.1 Normal modes in a lossy medium

Loss effects cause waves to abate. They are included in the model by adding a small complex number to the wavenumber describing the wave.

$$e^{ik_n r} \rightarrow e^{i(k_n + i\alpha_n)r} = e^{ik_n r - \alpha_n r} \quad (\text{D.17})$$

Here, α_n is the sum of attenuation in all media the sound is propagating through. A lossy pressure field is thus described by a combination of Eqs. D.18 and D.17.

$$p(r, z) = \frac{e^{\frac{i\pi}{4}}}{\rho(z_0)\sqrt{8\pi r}} \sum_{n=1}^{\infty} \Phi_n(z_0)\Phi_n(z) \frac{e^{ik_n r - \alpha_n r}}{\sqrt{k_n}}. \quad (\text{D.18})$$

D.2.2 The relevance of modes

The number of modes is infinite. For practical application, however, only a finite set of modes can be determined. The selection of such a set of modes is guided by the knowledge about their properties. These properties include monotonicity and completeness, which imply convergency of the model. Starting at the first eigenfunction and adding the next higher order mode will thus affect the accuracy of the model, only. Therefore, it is sufficient to select the first few lower order modes, dependent on the accuracy required.

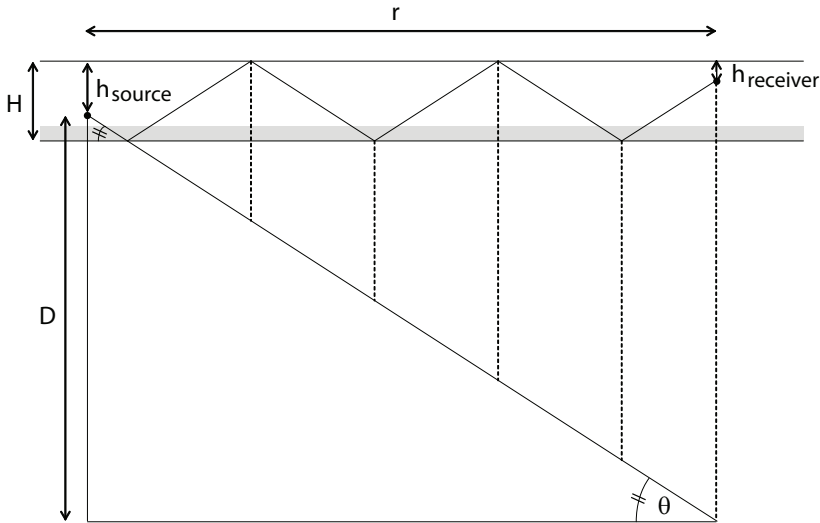


Figure D.3: Visualization of the number of interactions N_I of sound with the sediment–subbottom interface, assuming a simplified model of the environment with the water column and sediment layer treated as a single layer. Dependent on the angle of incidence θ and layer thickness H , N_I can be determined by equating $D = r \cdot \tan \theta$ with $D = 2 \cdot N_I \cdot H - h_{\text{source}} - h_{\text{receiver}}$. Here, h_{source} and h_{receiver} are the source and receiver depth respectively.

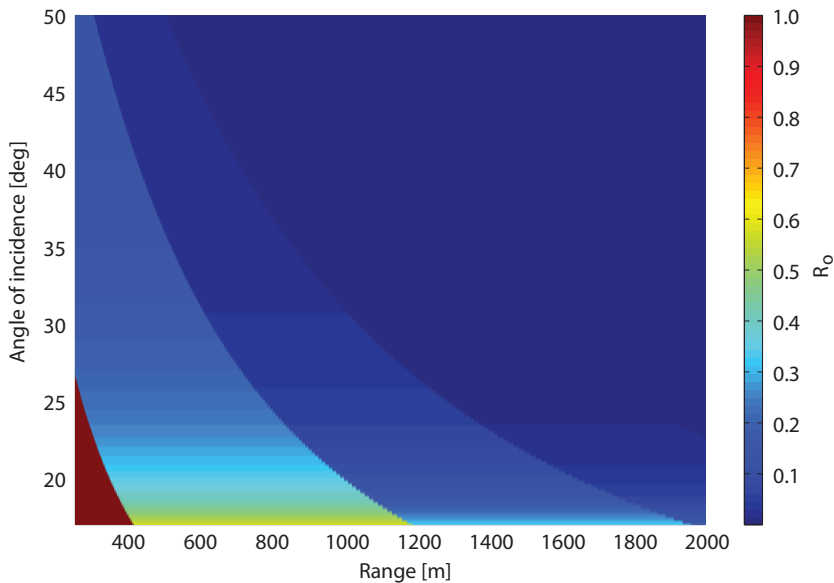


Figure D.4: Overall reflection per range and angle for continuous modes.

described in Fig. D.1. It can be seen that beyond 1200 m the continuous modes have hardly any effect on the acoustic field. At ranges between 400 m and 1200 m, however, the lowest order continuous modes still reflect 50% of the acoustic signal. At even smaller ranges, no interaction with the sea bottom is possible at grazing angles.

The first two data sets (RUN2 and RUN3) considered throughout this thesis feature a similar environment as considered here. Furthermore, their relevant source–receiver ranges are larger than 1000 m. The continuous modes can thus be neglected. This does not hold for the third data set (RUN5), whose ranges lie between 350 m and 800 m. However, environmental conditions are different at the site of RUN5 and calculations of R_o have to be based on a different geometry and sediment properties. Still, it is evident from analogous calculations of R_o that accounting for low order continuous modes might be beneficial for the accuracy of the model.

Accounting for additional continuous modes can be conducted by adding an additional virtual layer with high sound speed underneath the current 3-layer system. Increasing the sound speed in the virtual subbottom results in an increased critical angle and, therefore, a larger angular range containing the discrete modes. Additionally, the depth of the real subbottom needs to be large, to avoid interference of the virtual subbottom with the acoustic field. Large sound speed and a thick subbottom, however, are computationally demanding. Therefore, careful deliberations are required about whether these efforts are necessary at intermediate ranges.

D.2.3 Relations between the normal modes and the environment

By means of their phase velocity, normal modes can be assigned to sound waves passing through a specific regime (layer) of the environment. These phase velocities have been determined for a frequency of 500 Hz in the same environment as given in Fig. D.1, conditions which are typically encountered throughout this thesis. The phase velocities of the modes are provided in Fig. D.5 together with the sound speed in the environment. For this configuration, in total twelve discrete modes are obtained, which are displayed in Fig. D.6. As can be seen from Fig. D.5, only a single mode exists with a phase velocity between the minimum and maximum sound speed in the sediment layer. This mode describes the propagation within the sediment layer. The following 7 modes (modes 2-8) propagate in the water column, with phase velocities that do not exceed the maximum sound speed of the water column. They reflect at the water–sediment interface, but do not interact with the sea surface. Modes 9-12 reach the sediment–subbottom interface, where they reflect without penetrating into the subbottom.

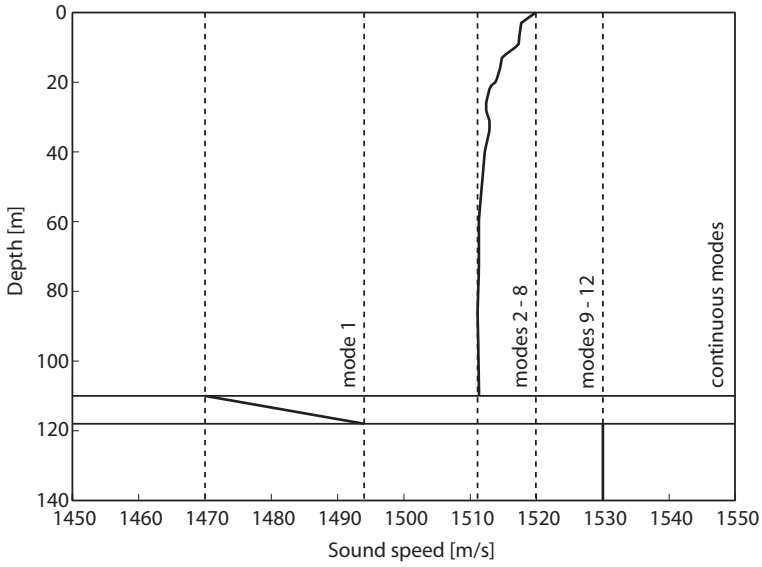


Figure D.5: Phase velocities $c_n = \frac{\omega}{k_n}$ of the normal modes at 500 Hz ($\omega = 500 \cdot 2 \cdot \pi$) of an underwater environment as defined in Fig. D.1. Also given is the sound speed profile of the environment.

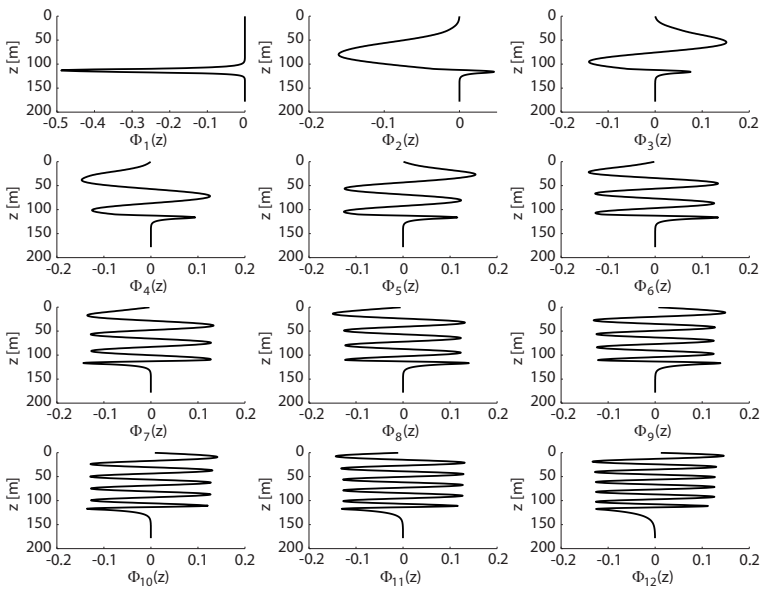


Figure D.6: Normal modes of an underwater environment as defined in Fig. D.1.

Global optimization

Model-based approaches for environmental classification require a physical description of the environment, often depending on a large set of parameters. The challenge is to find that parameter value combination from all possible ones that results in the optimal fit between measurements and model predictions. This aim can be achieved by a successive search of the parameter space by means of an optimization algorithm.

This Appendix is meant to give an overview over different types of optimization methods. Since the physical models employed for describing the underwater environment are often non-linear and local optima are likely, we focus on those optimization methods capable to find the global optimum.

E.1 Overview of global optimization strategies

Global optimization strategies can be either deterministic or heuristic [74]. Standard deterministic methods, like the brute force search, however, are highly computationally demanding. Probabilistic methods instead use smart strategies to direct the search. They can be roughly subdivided into Monte Carlo based algorithms, evolutionary algorithms, and such based on swarm intelligence.

An example of Monte Carlo based algorithms, which is common in underwater acoustics, is Simulated Annealing (SA), established by [75]. It was first employed to geoacoustic inversion by [76]. Starting at a single parameter value combination as solution candidate, it is based on an iterative random displacement and evaluation of energies. The random displacement is restricted to a small neighborhood. Decisions, whether a newly found point is accepted, are based on the Boltzman Equation. [75, 76] Acceptance of a higher-energetic solution is defined by a temperature (in analogy to the heating and cooling process of metal) and is more likely at the beginning of the search than at an advanced state. A disadvantage of SA, however, is its step size problem. [77]

Evolutionary algorithms, as described in [78], are also based on iteration. They employ strategies common to the evolutionary process in nature. A randomly chosen initial set of solution candidates or population members is altered according to processes like mutation, cross over, and survival of the fittest. Contrary to SA, a large number of solution candidates are investigated in a single step. An objective function, which describes the optimization goal, indicates the fitness of each candidate and is used for selection. Common evolutionary algorithms in underwater acoustics are the Genetic Algorithm (GA) and Evolutionary Strat-

This appendix is partly based on the following publication.

D. G. Simons, M. Snellen, and K. Siemes: "The potential of inverting geo-technical and geo-acoustic sediment parameters from single-beam echosounder returns," in *Proc. of the Underwater Acoustic Measurements (UAM) conference*, 2009.

egy (ES). Their main difference lies in the type of solution candidates they use. Whereas GA employs bit-string encoded parameters, ES employs numerical parameters, a strategy which is beneficial for finding the exact optimum.

A typical swarm intelligence algorithm is the Ant Colony Optimization (ACO) developed by [79], which is based on the behavior of ants. From an initial point, search directions are chosen randomly. The paths followed by the ants are marked (by pheromones in nature). These markings strengthen or weaken dependent on the amount of ants passing by. The probability that a specific path is chosen increases if it leads to a good solution (food) and if it already has a strong marking. The probability decreases, on the other hand, if the solution is not the best one anymore. Such algorithms are applicable, if the optimization problem can be reduced to finding an optimal path [74].

E.2 Differential Evolution (DE)

E.2.1 Optimization strategy

Differential evolution (DE), an efficient global optimization approach introduced by [80] and further described in [77], is used throughout this thesis. It has similarities with the GA, however, benefits from the advantages of an ES, operating on numerical, non-encoded values.

A schematic of the DE optimization strategy is given in Fig. E.1. As an evolutionary algorithm, DE is based on iteratively altering a population of parameter value combinations to create new generations of solutions that are fitter than their ancestors. Each generation g is a collection $P_{\vec{m},g}$ of Q members $\vec{m}_{i,g}$, $i = 1, \dots, Q$, which represent possible parameter value combinations.

$$P_{\vec{m},g} = (\vec{m}_{1,g}, \dots, \vec{m}_{Q,g}) \quad (\text{E.1})$$

In total, N_g generations are created in DE. The first generation $g = 0$ is initialized with randomly chosen values. A new generation evolves from their ancestors as follows. For the current population $P_{\vec{m},g}$, a partner population $P_{\vec{p},g}$ is created by mutation of three randomly chosen members $\vec{m}_{i_1,g}$, $\vec{m}_{i_2,g}$, and $\vec{m}_{i_3,g}$ of $P_{\vec{m},g}$.

$$\begin{aligned} P_{\vec{p},g} &= (\vec{p}_{1,g}, \dots, \vec{p}_{Q,g}) \text{ with} \\ \vec{p}_{i,g} &= \vec{m}_{i_1,g} + F(\vec{m}_{i_2,g} - \vec{m}_{i_3,g}) \end{aligned} \quad (\text{E.2})$$

Here, $F \in [0, 1]$ is a multiplication factor, responsible for regulating the difference between the original population and the partner population. Higher values for F result in an increasing difference between the two populations, whereas a smaller F results in slight differences only. [58] A descending generation $P_{\vec{d},g}$ is then determined by crossover of the original and partner population.

$$P_{\vec{d},g} = (\vec{d}_{1,g}, \dots, \vec{d}_{Q,g}) \quad (\text{E.3})$$

Each descendant $\vec{d}_{i,g}$ equals the original member $\vec{m}_{i,g}$ with p_c percent of its parameters being replaced by those of the partner population $\vec{p}_{i,g}$. The probability p_c at which a parameter is chosen from the partner population is often referred to as the crossover rate.

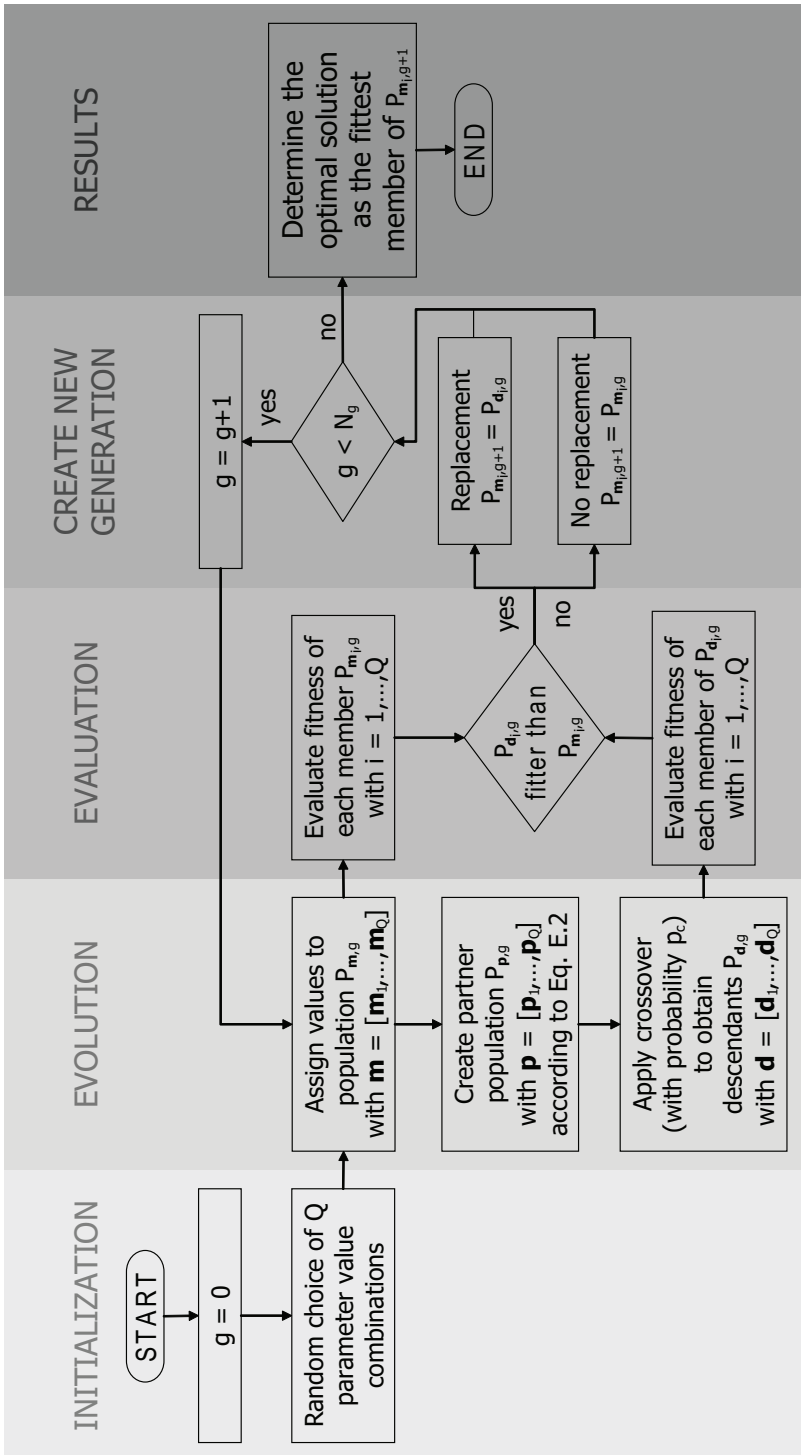


Figure E.1: Strategy of the DE optimization method.

At the end of each iteration step, an objective function determines the fitness⁹ of, both, the current members and their descendants. Then, those members which have a lower fitness than their descendants are replaced by their descendants. Often, instead of maximizing the fitness, the costs for each parameter value combination are minimized.

E.2.2 The performance of DE in inverting sediment properties

Global optimization methods, such as DE, have the potential to invert properties of the sea bottom even in complex environments. For efficiency reasons, DE has been applied throughout this thesis. In the following, we demonstrate the convergency behavior of DE by applying the approach to three sets of synthetic SBES data, created for a shallow-water environment with a constant water depth of 40 m. The data sets comprise three sediment types of different roughness and hardness. The first bottom contains sandy gravel, whereas no gravel is present in the other two bottoms, being composed of either muddy sand or sandy clay. For each environment, three parameters descriptive for the sediment type are estimated. These are the mean grain size M_z , the spectral strength w_2 , and the volume scattering parameter σ_2 .

For the performance analysis, a fixed setting of DE is chosen for all three environments. The multiplication factor and the crossover rate were set to $F = 0.6$ and $p_c = 0.55$, respectively. These values form a good compromise between the exploration of the entire search space and the convergency rate, as already observed by [58]. Furthermore, $N_g = 200$ generations are created iteratively, each containing $Q = 16$ parameter value combinations.

The results are shown in Figs. E.2-E.4. Each of these figures contains four different representations, indicating the performance of the DE.

In Figs. E.2-E.4(a), the development of the cost function over the 200 generations is given for 10 independent inversion runs. For each generation, the lowest costs are displayed. Also shown, as a red line, is the average of the 10 cost functions. The costs are ranging from one to zero, with zero costs representing the optimal fit when modeled parameter values equal the real ones. It can be seen that the graphs approach zero costs sufficiently (below an order of magnitude of 10^{-8}) after 150-200 generations for all sediment types considered. However, outliers might exist, such as in Fig. E.4(a). Results converging to such high states of costs have to be treated with caution since they do not represent the optimal fit.

Figures E.2-E.4(b) show the costs for the estimates of the three environmental parameters, separately. Here, the development of the costs is given for all population members throughout all generations, concentrating on a single inversion run. It is evident that parameter value combinations whose costs lie below 10^{-8} approach the true values well. However, this threshold has to be reconsidered for real data, for which a perfect fit is often prevented by the presence of noise. Another conclusion we can draw from Fig. E.2(b) is that σ_2 cannot be estimated well for sea bottoms with gravel content. This, however, is based on the sediment characteristics and not on the performance of the optimization method.

⁹The fitness describes the goodness of fit between a model calculation, incorporating the current parameter value combination, and the measurements.

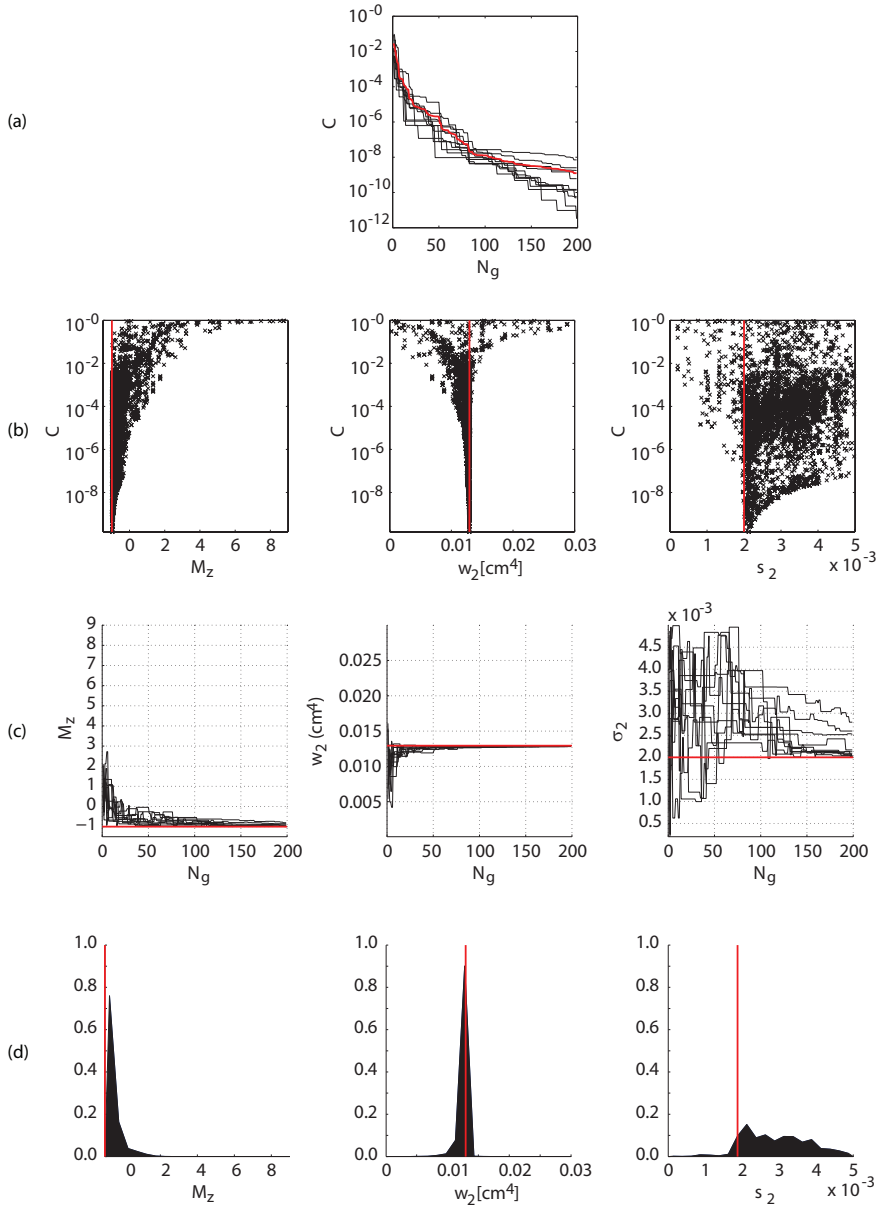


Figure E.2: Convergence behavior of DE when inverting M_z , w_2 , and σ_2 for a seafloor containing sandy gravel. Shown are: (a) values of the cost function per generation, (b) values of the cost function related to the specific parameters, (c) the convergence rate of the estimated parameters, and (d) the normalized histograms of the parameter estimates weighted by their costs. Red lines indicate in (a) the average energy and in (b)-(d) the true parameter values.

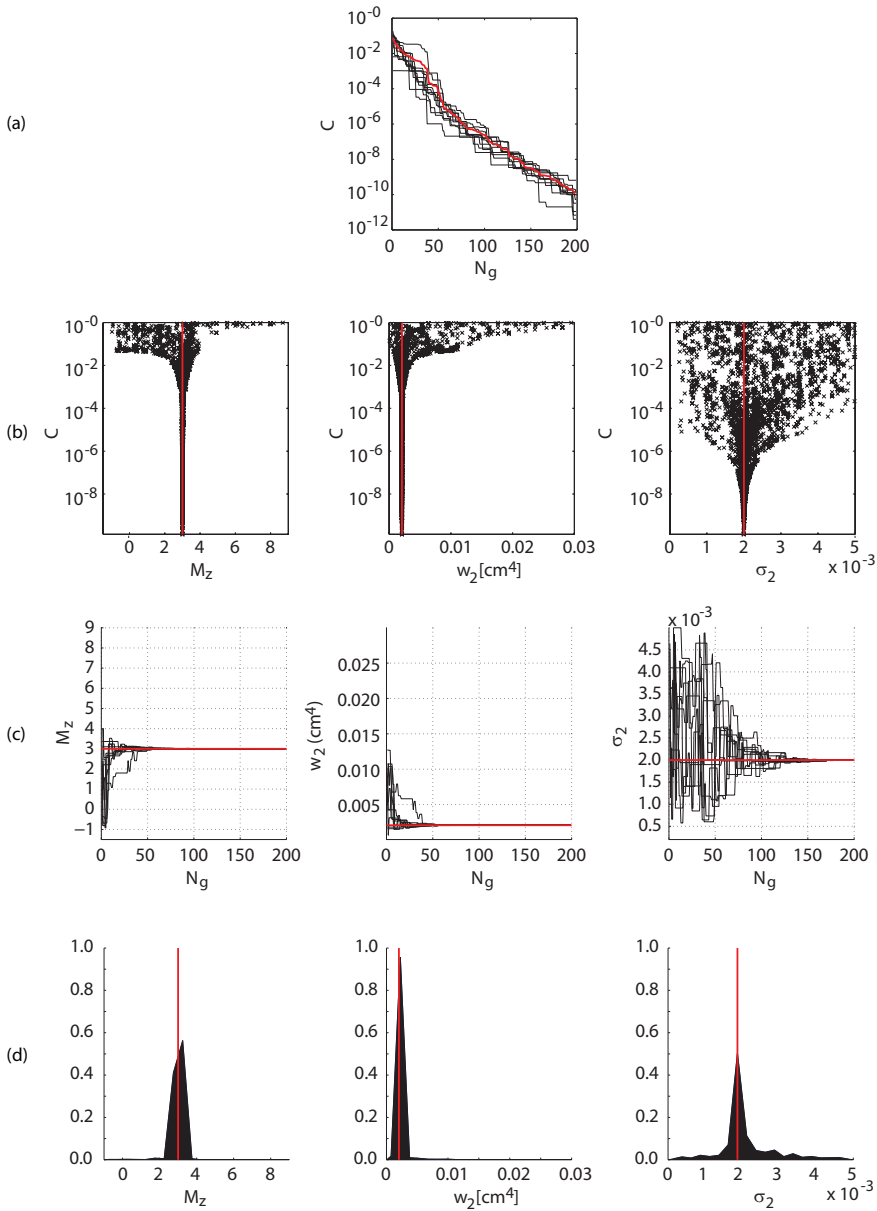


Figure E.3: Convergence behavior of DE when inverting M_z , w_2 , and σ_2 for a seafloor containing muddy sand. Shown are: (a) values of the cost function related to the specific parameters, (c) the convergence rate of the estimated parameters, and (d) the normalized histograms of the parameter estimates weighted by their costs. Red lines indicate in (a) the average energy and in (b)-(d) the true parameter values.

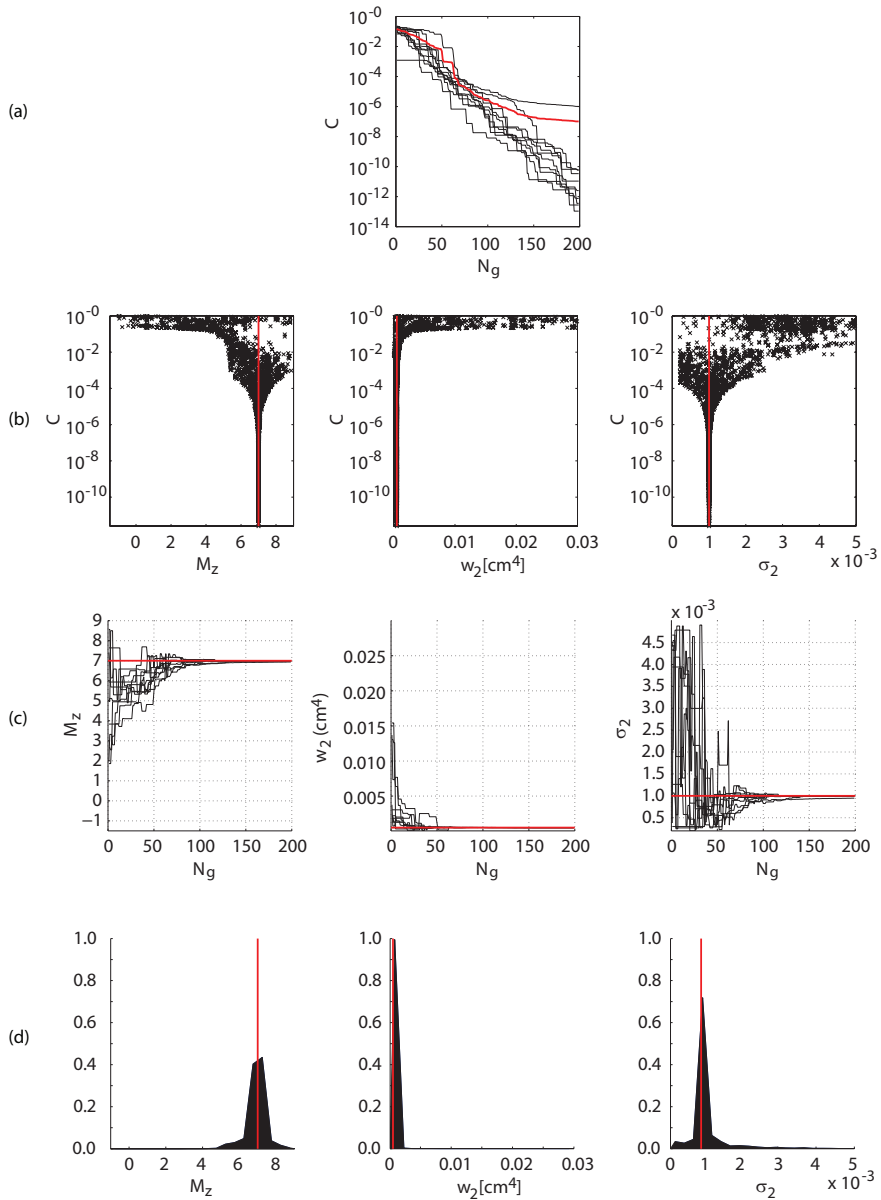


Figure E.4: Convergence behavior of DE when inverting M_z , w_2 , and σ_2 for a seafloor containing sandy clay. Shown are: (a) values of the cost function per generation, (b) values of the cost function related to the specific parameters, (c) the convergence rate of the estimated parameters, and (d) the normalized histograms of the parameter estimates weighted by their costs. Red lines indicate in (a) the average energy and in (b)-(d) the true parameter values.

The same trend as observed before is visible in Figures E.2-E.4(c), which show the convergence rate of the three parameters by plotting the best estimates of each generation. The parameter estimates converge after 150-200 generations, except for σ_2 for the sea bed containing sandy gravel. The estimates of σ_2 converge to values higher than the true value. Increasing the number of generation might be beneficial in this specific case. However, it is not evident that the estimates of σ_2 will approach the true values more closely.

Figures E.2-E.4(d) provide histograms of all parameter value estimates obtained during a single run. In order to focus on estimates with low costs, a weighing according to the Boltzmann distribution has been applied. This weighing has been adopted from the SA approach, where it provides a probability of selection $p_{SA,k}$ of the k -th parameter value combination \vec{m}_k dependent on the cost function C or fitness $1 - C$. [76]

$$p_{SA,k} = \frac{\exp[-(1 - C(\vec{m}_k))/T_{SA}]}{\sum_{j=1}^{Q \cdot N_g} \exp[-(1 - C(\vec{m}_j))/T_{SA}]} \quad (\text{E.4})$$

Table E.1: Mean grain size [ϕ]

Sediment type	True value	Mean	Standard deviation
Sandy gravel	-1	-0.945	6.803e-002
Muddy sand	3	2.999	9.441e-005
Sandy clay	7	7.000	2.265e-004

Table E.2: Spectral strength [cm^4]

Sediment type	True value	Mean	Standard deviation
Sandy gravel	0.012937	0.012901	4.532e-005
Muddy sand	0.002070	0.0020701	1.225e-007
Sandy clay	0.000518	0.000518	1.731e-008

Table E.3: Volume scattering parameter [-]

Sediment type	True value	Mean	Standard deviation
Sandy gravel	0.002	0.002238	2.8975e-004
Muddy sand	0.002	0.001998	2.6392e-006
Sandy clay	0.001	0.000999	1.6939e-007

The temperature T_{SA} , as defined in SA (see App. E.1), is chosen as the average costs of all parameter value combinations considered for the $Q = 16$ population members throughout $N_g = 200$ generations. Suppressing those parameter value combinations with high costs by applying Eq. E.4, the histograms in Figs. E.2-E.4(d), in general, show only a small spread around the true values. The best estimates can be expected for w_2 . For M_z , the peak around the true value is slightly broader and shows a slight deviation from the true value. Obviously, a large number of estimates lie close to the true value, before finally converging to it. The opposite is observed for the estimates of σ_2 . Here, large number of estimates lies further away from the true values, even at lower cost levels, causing the wings of the weighted histograms to rise. However, at least for the fine grained sediments (Fig. E.3 and Fig. E.4), the true value is reached at the lowest cost levels, resulting in a clearly defined peak.

The mean and standard deviation of the estimated parameters M_z , w_2 , and σ_2 obtained for the three sediment types sandy gravel, muddy sand and sandy clay are summarized in Tables E.1-E.3. For this calculation, the best results of ten independent inversions are considered. It is evident that the performance of the DE method is mainly dependent on the type of sediment present. The largest differences between mean and true value are observed for the sediment containing gravel, independent of the estimated parameter.

Bibliography

- [1] X. Lurton, *An introduction to underwater acoustics: Principles and applications*. Springer, 2002.
- [2] J. Grotzinger, T. H. Jordan, F. Press, and R. Siever, *Understanding Earth*, 5th ed. Freeman, 2007.
- [3] A. L. Rice, "The Challenger Expedition: the end of an area or a new beginning?" in *Understanding the oceans: a century of ocean exploration*, M. Deacon, T. Rice, and C. P. Summerhayes, Ed. Routledge, 2003, pp. 27–48.
- [4] C. de Moustier, "Beyond bathymetry: mapping acoustic backscattering from the deep seafloor with Sea Beam," *Journal of the Acoustic Society of America*, vol. 79, no. 2, pp. 316–331, 1985.
- [5] J. E. Hughes Clarke, "Toward remote seafloor classification using angular response of acoustic backscattering: a case study from multiple overlapping GLORIA data," *IEEE Journal of Oceanic Engineering*, vol. 19, no. 1, pp. 364–374, 1994.
- [6] L. Hellequin, J.-M. Boucher, and X. Lurton, "Processing of high-frequency multibeam echo sounder data for seafloor characterization," *IEEE Journal of Oceanic Engineering*, vol. 28, no. 1, pp. 78–89, 2003.
- [7] G. Canepa and E. Pouliquen, "Inversion of geo-acoustic properties from high frequency multibeam data," in *Boundary Influences in High Frequency, Shallow Water Acoustics*, N. G. Pace and P. Blondel, Eds. University of Bath, UK, 2005, pp. 233–240.
- [8] D. G. Simons and M. Snellen, "A Bayesian approach to seafloor classification using multi-beam echo-sounder backscatter data," *Applied Acoustics*, vol. 70, no. 10, pp. 1258–1268, 2009, doi 10.1016/j.apacoust.2008.07.013.
- [9] J. M. Preston, "Automated acoustic seabed classification of multibeam images of Stanton Banks," *Applied Acoustics*, vol. 70, no. 10, pp. 1277–1287, 2009.
- [10] W. Collins, R. Gregory, and J. Anderson, "A digital approach to seabed classification," *Sea Technol.*, vol. 37, no. 18, pp. 83–87, 1996.
- [11] L. J. Hamilton, P. J. Mulhearn, and R. Poeckert, "Comparison of RoxAnn and QTC View acoustic bottom classification system performance for the Cairns area, Great Barrier Reef, Australia," *Cont. Shelf Res.*, vol. 19, pp. 1577–1597, 1999.

- [12] C. R. Bates and E. J. Whitehead, "ECHOplus measurements in the hopavågen bay, norway," *Sea Technol.*, vol. 42, no. 6, p. 34, 2001.
- [13] D. D. Sternlicht and C. P. de Moustier, "Remote sensing of sediment characteristics by optimized echo-envelope matching," *Journal of the Acoustic Society of America*, vol. 114, no. 5, pp. 2727–2743, 2003.
- [14] —, "Time-dependent seafloor acoustic backscatter (10-100 kHz)," *Journal of the Acoustic Society of America*, vol. 114, no. 5, pp. 2709–2725, 2003.
- [15] Wienberg, C. and A. Bartholomä, "Acoustic seabed classification in a coastal environment (outer Weser Estuary, German Bight) - a new approach to monitor the dredging and dredge spoil disposal," *Continental Shelf Research*, vol. 25, no. 9, pp. 1143–1156, 2005.
- [16] P. A. van Walree, M. A. Ainslie, and D. G. Simons, "Mean grain size mapping with single-beam echo sounders," *Journal of the Acoustic Society of America*, vol. 120, no. 5, pp. 2555–2566, 2006.
- [17] J. M. Preston, A. C. Christney, W. T. Collins, and S. Bloomer, "Automated acoustic classification of sidescan images," in *Proceedings of the IEEE Oceans Conference '04*, 2004, pp. 2060–2065.
- [18] J.-P. Hermand and P. Gerstoft, "Inversion of broad-band multitone acoustic data from the YELLOW SHARK summer experiments," *IEEE Journal of Oceanic Engineering*, vol. 21, no. 4, pp. 324–346, 1996.
- [19] M. Snellen, D. G. Simons, M. Siderius, J. Sellschopp, J. and P. L. Nielsen, "An evaluation of the accuracy of shallow water matched field inversion results," *Journal of the Acoustic Society of America*, vol. 109, no. 2, pp. 514–527, 2001.
- [20] S. E. Dosso, M. J. Wilmut, and A.-L. S. Lapinski, "An adaptive-hybrid algorithm for geoacoustic inversion," *IEEE Journal of Oceanic Engineering*, vol. 26, pp. 324–336, 2001.
- [21] M. Siderius, P. L. Nielsen, and P. Gerstoft, "Range-dependent seabed characterization by inversion of acoustic data from a towed receiver array," *Journal of the Acoustic Society of America*, vol. 112, pp. 1523–1535, 2002.
- [22] M. R. Fallat, S. E. Dosso, and P. L. Nielsen, "An investigation of algorithm-induced variability in geoacoustic inversion," *IEEE Journal of Oceanic Engineering*, vol. 29, no. 1, pp. 78–87, 2004.
- [23] Yong-Min Jiang and N. Ross Chapman, "Bayesian geoacoustic inversion in a dynamic shallow water environment," *Journal of the Acoustic Society of America*, vol. 123, no. 6, pp. EL155–EL161, 2008.
- [24] C. Flewelling, N. Millard, and I. Rose, "TOBI, a vehicle for deep ocean survey," *IEEE Journal of Oceanic Engineering*, vol. 5, no. 2, pp. 85–93, 1993.

- [25] J.-P. Hermand, "Broad-band geoacoustic inversion in shallow water from waveguide impulse response measurements on a single hydrophone: Theory and experimental results," *IEEE Journal of Oceanic Engineering*, vol. 24, no. 1, pp. 41–66, 1999.
- [26] J.-P. Hermand and J.-C. Le Gac, "Subseafloor geoacoustic characterization in the kilohertz regime with a broadband source and a 4-element receiver array," in *Proceedings of the Oceans '08 MTS/IEEE Quebec conference - Oceans, Poles and Climate: Technological Challenges*. Marine Technology Society, Institute of Electrical and Electronics Engineers, IEEE, Sep. 2008.
- [27] —, "Toward higher acoustic frequencies and fewer hydrophones to invert for sub-bottom properties with underwater robots: Experimental results," in *Proceedings of the Pacific Rim Underwater Acoustics Conference '09, Mid to High Frequency Ocean Acoustics: Modeling, Measurement, and Applications*, 2009, pp. 79–82.
- [28] M. Berrada, et al., "Efficient semi-automatic adjoint generation and its application for implementing acoustic particle velocity in geoacoustic inversion," in *Proceedings of the 8th International Conference on Theoretical and Computational Acoustics (ICTCA) '07*, 2007, pp. 13–21.
- [29] J.-C. Le Gac and J.-P. Hermand, "MREA/BP07 cruise report," NATO Undersea Research Center, La Spezia, Italy, Tech. Rep. NURC-CR-2007-04-1D1, Dec. 2007.
- [30] O. Carrière, J.-P. Hermand, J.-C. Le Gac, and M. Rixen, "Full-field tomography and Kalman tracking of the range-dependent sound speed field in a coastal water environment," *Journal of Marine Systems. Special issue on MREA and Coastal Processes: Challenges for Monitoring and Prediction*, vol. 78, pp. S382–S392, 2009, doi:10.1016/j.jmarsys.2009.01.036.
- [31] O. Carrière, J.-P. Hermand, and J. V. Candy, "Inversion for time-evolving sound-speed field in a shallow ocean by ensemble Kalman filtering," *IEEE Journal of Oceanic Engineering*, vol. 34, no. 4, pp. 586–602, 2009.
- [32] M. Siderius and J.-P. Hermand, "Yellow shark spring 1995: Inversion results from sparse broadband acoustic measurements over a highly range-dependent soft clay layer," *of the Acoustic Society of America*, vol. 106, no. 2, pp. 637–651, 1999.
- [33] F. L. Chiocci, L. Orlando, and P. Tortora, "Small-scale seismic stratigraphy and paleogeographical evolution of the continental shelf facing the SE Elba Island (northern Tyrrhenian Sea, Italy)," *Journal of Sedimentary Petrology*, vol. 61, no. 4, pp. 506–526, 1991.
- [34] D. G. Simons, M. Snellen, and M. A. Ainslie, "A multivariate correlation analysis of high-frequency bottom backscattering strength measurements with geotechnical parameters," *IEEE Journal of Oceanic Engineering*, vol. 32, no. 3, 2007.
- [35] P. A. van Walree, J. Tegowski, C. Laban, and D.G. Simons, "Acoustic seafloor discrimination with echo shape parameters: A comparison with the ground truth," *Continental Shelf Research*, vol. 25, pp. 2273–2293, 2005.
- [36] I. Jolliffe, *Principal component analysis*, 2nd ed. Springer, 2002.

- [37] G. A. F. Seber, *Multivariate Observations*. Wiley, 1984.
- [38] A.R. Amiri-Simkooei, M. Snellen, and D.G. Simons, "Riverbed sediment classification using MBES backscatter data," *Journal of the Acoustic Society of America*, vol. 126, no. 4, pp. 1724–1738, 2009.
- [39] ———, "Principal component analysis of single-beam echo-sounder signal features for seafloor classification," *IEEE Journal of Oceanic Engineering*, vol. 36, no. 2, pp. 259–272, 2011.
- [40] Applied Physics Laboratory, University of Washington, "APL-UW high-frequency ocean environmental acoustic models handbook," Oct. 1994, Technical Report APL-UW TR 9407AEAS 9501.
- [41] R.J. Urick, *Principles of underwater sound*, 3rd ed. Peninsula Publishing, 1983.
- [42] D. G. Simons, K. Siemes, and M. Snellen, "The potential of inverting geo-technical and geo-acoustic sediment parameters from single-beam echosounder returns," in *Proceedings of the Underwater Acoustic Measurements Conference (UAM), Nafplion, Greece, 2009*.
- [43] M. Snellen, K. Siemes, and D.G. Simons, "On the practical applicability of single-beam model-based seafloor classification," in *Proceedings of the European Conference on Underwater Acoustics (ECUA) '10, Istanbul, 2010*.
- [44] P. D. Mourad and D.R. Jackson, "High frequency sonar equation models for bottom backscatter forward loss," in *Proceedings of the IEEE Oceans conference 1989*, vol. 4, 1989, pp. 1168–1175.
- [45] C. de Moustier and D. Alexandrou, "Angular dependence of 12-kHz seafloor acoustic backscatter," *Journal of the Acoustic Society of America*, vol. 90, no. 1, pp. 522–531, 1991.
- [46] D. G. Simons and M. Snellen, "A comparison between modeled and measured high frequency bottom backscattering," in *Proceedings of the European Conference on Underwater Acoustics (ECUA) '08, Paris, 2008*.
- [47] T. F. Coleman and Y. Li, "An interior trust region approach for nonlinear minimization subject to bounds," *SIAM Journal on Optimization*, vol. 6, no. 2, pp. 418–445, 1996.
- [48] C. L. Lawson and R. J. Hanson, *Solving least-squares problems*. Prentice-Hall, Inc., 1974, series in automatic computation.
- [49] A. Amiri-Simkooei, M. Snellen and D. G. Simons, "Using MBES for classification of riverbed sediments," in *Proceedings of the European Conference on Underwater Acoustics (ECUA) '08, 2008*.
- [50] K. Siemes, M. Snellen, D. G. Simons, and J.-P. Hermand, "Using MBES backscatter strength measurements for assessing a shallow water soft sediment environment," in *Proceedings of the IEEE Oceans Conference, Bremen, 2009*.

- [51] A. B. Baggeroer, W. A. Kuperman, and P.N. Mikhalevsky, "An overview of matched field methods in ocean acoustics," *IEEE Journal of Oceanic Engineering*, vol. 18, no. 4, pp. 401–424, 1993.
- [52] A. Tolstoy, *Matched field processing for underwater acoustics*. World Scientific Publishing Co., 1993.
- [53] M. R. Fallat and S. E. Dosso, "Geoacoustic inversion via local, global, and hybrid algorithms," *Journal of the Acoustic Society of America*, vol. 105, no. 6, pp. 3219–3230, 1999.
- [54] M. Siderius, P. Gerstoft, and P. L. Nielsen, "Broadband geo-acoustic inversion from sparse data using genetic algorithms," *Journal of Computational Acoustics*, vol. 6, pp. 117–134, 1998.
- [55] C. F. Mecklenbräuker and P. Gerstoft, "Objective functions for geoacoustic inversion derived by likelihood methods," *Journal of Computational Acoustics*, vol. 8, no. 2, pp. 259–270, 2000.
- [56] Y. H. Goh, P. Gerstoft and W. S. Hodgkiss, "Statistical estimation of transmission loss from geoacoustic inversion using a towed array," *Journal of the Acoustic Society of America*, vol. 122, no. 5, pp. 2571–2579, 2007.
- [57] M. I. Taroudakis and M. G. Markaki, "Bottom geoacoustic inversion by matched field processing—a sensitivity study," *Inverse Problems*, vol. 16, pp. 1679–1692, 2000.
- [58] M. Snellen and D.G. Simons, "An assessment of the performance of global optimization methods for geo-acoustic inversion," *Journal of Computational Acoustics*, vol. 16, no. 2, pp. 199–223, 2008.
- [59] F. B. Jensen and M. C. Ferla, "SNAP: The SACLANTCEN normal-mode acoustic propagation model," SACLANT Undersea Research Centre, La Spezia, Italy, Tech. Rep. SM-121, 1979.
- [60] E. L. Hamilton and R. T. Bachman, "Sound velocity and related properties of marine sediments," *Journal of the Acoustic Society of America*, vol. 72, no. 6, pp. 1891–1904, 1982.
- [61] E. L. Hamilton, "Compressional-wave attenuation in marine sediments," *Geophysics*, vol. 37, no. 4, pp. 620–646, 1972.
- [62] —, "Geoacoustic modeling of the seafloor," *Journal of the Acoustic Society of America*, vol. 68, no. 5, pp. 1313–1340, 1980.
- [63] K. Siemes, M. Snellen, A. R. Amiri-Simkooei, D. G. Simons, and J.-P. Hermand, "Predicting spatial variability of sediment properties from hydrographic data for geo-acoustic inversion," *IEEE Journal of Oceanic Engineering*, vol. 35, no. 4, pp. 766–778, 2010.
- [64] W. C. Krumbein and L. L. Sloss, *Stratigraphy and Sedimentation*, 2nd ed. Freeman, 1963.

- [65] C. K. Wentworth, "A scale of grade and class terms for clastic sediments," *Journal of Geology*, vol. 30, pp. 377–392, 1922.
- [66] R. L. Folk and W. C. Ward, "Brazos River bar: a study in the significance of grain size parameters," *Journal of Sedimentary Petrology*, vol. 27, no. 1, pp. 3–26, 1957.
- [67] R. L. Folk, "A review of grain-size parameters," *Sedimentology*, vol. 6, pp. 73–93, 1966.
- [68] ———, *Petrology of sedimentary rocks*. Hemphill, 1974.
- [69] F. P. Shepard, "Nomenclature based on sand-silt-clay ratios," *Journal of Sedimentary Petrology*, vol. 24, pp. 151–158, 1954.
- [70] R.J. Urick, *Sound propagation in the sea*. Peninsula Publishing, 1982.
- [71] F. B. Jensen, W. A. Kuperman, M. B. Porter, and H. Schmidt, *Computational ocean acoustics*. AIP Press, 1994.
- [72] P. C. Etter, *Underwater Acoustic Modelling and Simulation*, 3rd ed. Spon, 2003.
- [73] ———, "Underwater acoustic modeling techniques," *The Shock and Vibration Digest*, vol. 13, no. 2, pp. 11–20, 1981.
- [74] T. Weise, *Global optimization algorithms – Theory and application*, 2nd ed., 2009, online available at <http://www.it-weise.de>, last viewed 04.08.2011.
- [75] S. Kirkpatrick, C. D. Gelatt, M. P. Vecchi, "Optimization by simulated annealing," *Science*, vol. 220, pp. 671–680, 1983.
- [76] P. Gerstoft, "Inversion of seismoacoustic data using genetic algorithms and a posteriori probability distributions," *Journal of the Acoustic Society of America*, vol. 95, no. 2, pp. 770–782, 1994.
- [77] K. V. Price, R. M. Storn, and J. A. Lampinen, *Differential evolution. A practical approach to global optimization*. Springer, 2005.
- [78] T. Bäck, *Evolutionary algorithms in theory and practice: Evolution Strategies, Evolutionary Programming, Genetic Algorithms*. Oxford University Press US, 1996.
- [79] M. Dorigo, V. Maniezzo, and A. Colorni, "The ant system: Optimization by a colony of cooperating agents," *IEEE Transactions on Systems, Man, and Cybernetics Part B: Cybernetics*, vol. 26, no. 1, pp. 29–41, 1996, online available at <ftp://iridia.ulb.ac.be/pub/mdorigo/journals/IJ.10-SMC96.pdf>, last viewed 04.08.2011.
- [80] R. Storn and K. Price, "Differential evolution – A simple and efficient adaptive scheme for global optimization over continuous spaces," ICSI Technical Report TR-95-012, Mar. 1995.

Summary

Detailed information about the oceanic environment is essential for many applications in the field of marine geology, marine biology, coastal engineering, and marine operations. Especially, knowledge of the properties of the sediment body is often required.

Acoustic remote sensing techniques have become highly attractive for classifying the sea bottom and for mapping the sediment properties, due to their high coverage capabilities and low costs compared to common sampling methods. In the last decades, a number of different acoustic devices and related techniques for analyzing their signals have evolved. Each sensor has its specific application due to limitations in the frequency range and resolution. In praxis, often a single acoustic tool is chosen based on the current application, supported by other non-acoustic data where required. However, different acoustic remote sensing techniques can supplement each other, as shown in this thesis. Even more, a combination of complementary approaches can contribute to the proper understanding of sound propagation, which is essential when using sound for environmental classification purposes. This includes the knowledge of the relation between acoustics and sediment properties, the focus of this thesis.

Providing a detailed three dimensional environmental picture that allows for gaining maximum insight into this relation is aimed at. For this purpose, standard and advanced techniques for classifying the underwater environment are presented. Systems dealt with cover both standard hydrographic surveying systems (including a single-beam echosounder using 12, 38, and 200 kHz, a 300 kHz multibeam echosounder, and two seismic systems in the range of 0.5–15 kHz) and dedicated measurement configurations consisting of a source (0.3–1.6 kHz) and a receiver array. Both their field of application and their limitations are analyzed. Furthermore, special attention has been paid to the efficiency regarding the collection and processing of the data.

The research presented in this thesis is a part of an interdisciplinary experimental effort that aims at addressing an integrated concept of Maritime Rapid Environmental Assessment (MREA). In this context, the MREA/Blue Planet (BP)'07 trial [29], was carried out in a shallow water environment with fine grained sediments of the Mediterranean Sea in 2007. The data collected throughout this trial form the basis of this thesis. In order to provide an even more comprehensive analysis of the relation between acoustics and sediment properties, a second dataset is considered, covering a larger variety of sediment types. These data are collected in the North Sea in 2004.

After a description of acoustic devices used for surveying the sea bottom in Chapter 2 and an introduction of the two environments in which data are obtained in Chapter 3, different approaches for analyzing the environmental characteristics are discussed throughout the thesis. In general, we can distinguish between phenomenological and model based approaches. The phenomenological approaches employ parameters related to the acoustic

signal, which give information on the presence of acoustic classes, when they are mapped. Such parameters are, for example, the intensity of the reflected signal under normal incidence or backscatter values in the case of measurements under oblique angles. Also parameters describing the shape of the signal are relevant. However, a link to sediment parameters, such as grain size, can only be obtained when using additional ground truth data. Model based approaches, on the other hand, provide a direct link of the acoustic signal to sediment properties by fitting a sophisticated physical description of the acoustic signal to the measured one. However, this comes at the price of high computational efforts. Especially, in cases in which large numbers of model parameters need to be searched for, an efficient optimization technique is required to search for those parameter values that maximize the agreement between measured and modeled signal. Throughout this thesis, differential evolution is used for efficient optimization. This optimization strategy employs several parameter value combinations at once, which are then iteratively altered by mutation and combination, creating a better fit.

In Chapter 4, classification methods applicable to the signals of a single-beam echosounder are analyzed. First, a phenomenological approach is considered. It employs a number of statistical moments of the acoustic signal to describe its shape, which is known to be related to the sediment roughness and hardness. Since these statistical moments are possibly correlated, a principal component analysis is performed conform [36], to transform these parameters by means of an eigenvalue decomposition of the parameter covariance matrix into a smaller number of uncorrelated variables. From these principal components, acoustic classes are obtained by a cluster analysis. A different approach is the modeling of the received echoes, assuming these to be shaped by the scattering at the rough sediment–water interface and at inhomogeneities in the sediment volume as proposed by [13]. Here, model parameters are the sediment–water ratio of mass density, the sediment–water ratio of sound speed, the imaginary to real wave number ratio, the spectral strength of surface roughness, and a volume scattering parameter. Empirical relations that couple these parameters to the mean grain size are used. These are valid for mean grain sizes from -1ϕ to 9ϕ . Due to only little variation in these empirical relations for grain sizes between 7ϕ and 9ϕ , an extrapolation to even smaller grain sizes (larger ϕ -values) did not succeed. Deviations of the empirical relations for the spectral strength and the volume scattering parameter from the true values, as documented in [40], are confirmed. Beyond this, it is found that the parameters to be estimated should at least include the mean grain size, the spectral strength accounting for surface roughness, and a volume scattering parameter. In an attempt to reduce the computational effort needed, a second model is investigated. It deduces the reflection coefficient from the echo energy and empirically relates it to the mean grain size, as proposed by [16]. This approach was found to be hampered by a limited beamwidth. Even for echosounders with a larger beamwidth, the model is restricted to medium and large grain sizes since the reflection coefficient is not sensitive to mean grain sizes larger than 5.5ϕ . Overall, only the phenomenological approach could be successfully applied to the small grain sizes that are present in the MREA/BP'07 area. Still, for the medium-sized grain sizes in the North Sea, the estimates of the model-based approach which incorporates the mean grain size, the spectral strength, and the volume scattering show reasonable agreement with the grab samples.

In Chapter 5, a Bayesian approach as proposed by [8] is applied to classify multibeam echosounder data. It employs the intensity of the backscattered acoustic signal per beam. By treating the beams separately, the across-track variations of the sea bottom are ac-

counted for. Adaptations have been made to obtain consistent results at different beam angles and depths. The Bayesian approach is based on the assumption that the central limiting theorem holds and the backscatter values are normally distributed. A number of Gaussians, representing each an acoustic class of the sediment at the beam under consideration, is then fitted to the histogram of these data. Typically, the acoustic classes are linked to grain size or sediment type. Indeed, the distribution of these classes is shown to be representative for the distribution of the sediment type. It is also in agreement with the distribution of single-beam echosounder classes. However, a comparison with ground truth data obtained from grab samples reveals that parameters other than the grain size, such as the presence of gas, are also important for interpreting the acoustic classes. Furthermore, small-scale structures on the seafloor could be revealed by this approach.

Chapters 6 and 7 treat dedicated acoustic systems, consisting of a source and a receiving array. Here, a drifting sparse vertical line array with four hydrophones and a stationary source are employed. Matched-filter processing (pulse compression) is applied to the data obtained at the hydrophone positions. The acoustic field is then modeled by normal modes and geoacoustic inversion of the parameters that are descriptive for the environment is applied. The underlying environmental model is composed of three layers: the water column, a sediment layer, and the subbottom. When modeling the entire acoustic field, one has to account for a large number of parameters, which results in high computational costs. Therefore, investigations towards an optimal inversion strategy and optimal frequency band are carried out. Furthermore, the performance of geoacoustic inversion in three different environments is investigated. The approach turns out to work well for very small grain sizes of $10 - 11 \phi$. It is also shown that the presence of gas can be indicated by the inverted sediment sound speed. However, the approach is found to be hampered by short source–receiver ranges of less than a kilometer and by the presence of a sediment layer of over 40 meters of thickness.

A comparison of all environmental descriptions presented so far confirms the consistency of the environmental picture established. Furthermore, the ability of the different results to explain phenomena that could not be related to grain size has become apparent. In addition, a combination of the classification of the upper sediment layer achieved by hydrographic surveying and the sediment layering obtained from seismic measurements is shown to be a representative criterion for selecting areas for subseafloor sediment classification by geoacoustic inversion techniques.

Samenvatting

Gedetailleerde informatie over de omgeving onder de zeespiegel is van essentieel belang voor vele toepassingen in het gebied van marine geologie, marine biologie, kustontwikkeling en marine operaties. Vaak is vooral de kennis van de eigenschappen van het sediment vereist.

Akoestische *remote sensing* technieken zijn, vergeleken met standaard bemonsteringsmethoden, aantrekkelijk voor het classificeren van de zeebodem en voor het in kaart brengen van de sedimenteigenschappen, vanwege hun hoge dekkingsgraad en lage kosten. In de laatste decennia zijn er verschillende akoestische instrumenten en technieken voor het analyseren van hun signalen ontwikkeld. Als gevolg van beperkingen in de bandbreedte en resolutie heeft elke sensor zijn specifieke toepassing. Afhankelijk van de toepassing, wordt in de praktijk vaak een enkel akoestisch instrument gekozen. Indien nodig wordt dit ondersteund door andere niet-akoestische metingen.

Verschiede akoestische *remote sensing* technieken kunnen elkaar echter aanvullen, zoals in dit proefschrift wordt getoond. Sterker nog, een combinatie van complementaire benaderingen kunnen bijdragen aan een goed begrip van de geluidspropagatie onder de zeespiegel, welk van essentieel belang is bij het gebruik van geluid voor de classificatie van een bepaald oceanisch gebied. Dit betreft kennis van de relatie tussen de akoestiek en de sediment eigenschappen, hetgeen de focus van dit proefschrift vormt.

Het genereren van een gedetailleerd driedimensionaal beeld met maximaal inzicht in deze relatie wordt hierbij nagestreefd. Hiervoor worden standaard en geavanceerde technieken voor het classificeren van een oceanisch gebied gepresenteerd. Behandeld worden zowel standaard hydrografische systemen (een *single-beam* echolood met 12, 38 en 200 kHz, een 300 kHz *multibeam* echolood en twee seismische systemen van 0.5–15 kHz) als speciale meetconfiguraties bestaand uit een bron (0.3-1.6 kHz) en een array van ontvangers. Zowel hun gebied van toepassing als hun beperkingen zijn geanalyseerd. Bovendien is er bijzondere aandacht besteed aan het efficiënte verzamelen en bewerken van de data.

Het onderzoek dat in dit proefschrift wordt gepresenteerd is een onderdeel van een interdisciplinaire experimentele inspanning die gericht is op het geïntegreerd concept van *Maritime Rapid Environmental Assessment* (MREA). In dit verband is de MREA/Blue Planet (BP) '07 trial uitgevoerd in 2007 [29], in een ondiep deel van de Middellandse Zee dat bekend staat om zijn fijnkorrelige sedimenten. De verzamelde gegevens van deze trial vormen de basis van dit proefschrift. Om een nog uitgebreidere analyse van de relatie tussen de akoestiek en de eigenschappen van het sediment te verkrijgen, wordt een tweede dataset met een groter aantal sedimenttypes beschouwd. Deze gegevens zijn verzameld in de Noordzee in 2004.

Nadat er in hoofdstuk 2 een beschrijving van de gebruikte akoestische systemen is gegeven, gevolgd door een introductie van de twee omgevingen waarin gegevens zijn verzameld in hoofdstuk 3, worden in het resterende deel van het proefschrift de verschillende

benaderingen voor het analyseren van de gebiedseigenschappen besproken. In het algemeen kunnen we fenomenologische en model-gebaseerde benaderingen onderscheiden. De fenomenologische benadering werkt met parameters die gerelateerd zijn aan het akoestische signaal. Als deze parameters in kaart worden gebracht, geven zij informatie over de aanwezigheid van akoestische klassen. Dergelijke parameters zijn bijvoorbeeld de intensiteit van het gereflecteerde signaal onder loodrechte invalshoek of *backscatter* waarden voor metingen onder een schuine hoek. Ook parameters die de vorm van het signaal beschrijven zijn relevant. Een link naar sediment parameters, zoals korrelgrootte, kan echter alleen worden verkregen door het gebruik van aanvullende *ground truth* data. Model-gebaseerde benaderingen geven een directe koppeling van het akoestische signaal met de sediment eigenschappen, door een fysieke beschrijving van het akoestische signaal op de gemeten signalen te fitten. Dit vergt veel rekentijd. Vooral in de gevallen waarin het aantal modelparameters groot is, zijn efficiënte optimalisatiemethodes nodig, om naar die parameterwaarden te zoeken, die naar de grootste mogelijke overeenkomst tussen het gemeten en het gemodelleerde signaal leiden. In dit proefschrift wordt gebruik gemaakt van *differential evolution* als een efficiënte optimalisatiemethode. Deze optimalisatiemethode gebruikt verschillende combinaties van parameterwaarden tegelijk, die vervolgens iteratief worden gewijzigd door mutatie en combinatie om een betere fit te genereren.

In hoofdstuk 4 worden classificatiemethoden voor de signalen van een *single-beam* echolood geanalyseerd. Eerst wordt een fenomenologische benadering gevolgd. Deze maakt gebruik van een aantal statistische momenten die de vorm van het akoestische signaal beschrijven en gerelateerd aan de ruwheid en hardheid van het sediment zijn. Aangezien deze statistische momenten mogelijk gecorreleerd zijn, is er een *principal component analysis* uitgevoerd conform [36], die deze parameters door middel van een *eigenvalue decomposition* van de covariance matrix in een kleiner aantal ongecorrleerde variabelen transformeert. Uit deze hoofdcomponenten (*principal components*) worden akoestische klassen verkregen door een cluster analyse. Een andere benadering is het modelleren van de ontvangen echo's onder de aanname dat de signalen worden gevormd door *scattering* zowel aan de ruwe grens tussen sediment en water als ook aan inhomogeniteiten in het sediment volume, zoals voorgesteld door [13]. De gebruikte modelparameters zijn de sediment–water verhouding van massa dichtheid, de sediment–water verhouding van de geluidssnelheid, de verhouding van het imaginaire tot het reële golfgetal, de *spectral strength* van de sediment–water ruwheid en een *volume scattering parameter*. Er wordt gebruik gemaakt van empirische relaties die deze parameters aan de gemiddelde korrelgrootte koppelen. Deze zijn geldig voor gemiddelde korrelgroottes tussen -1ϕ en 9ϕ . Door slechts weinig variatie in deze empirische relaties voor korrelgroottes tussen 7ϕ en 9ϕ is een extrapolatie naar nog kleinere korrels (grotere ϕ -waarden) niet gelukt. Afwijkingen van de empirische relaties van de werkelijke waarden voor de *spectral strength* en de *volume scattering parameter*, die zijn gedocumenteerd in [40], worden bevestigd. Hiernaast is geconstateerd dat de te schatten parameters ten minste de gemiddelde korrelgrootte, de *spectral strength* en de *volume scattering parameter* zouden moeten omvatten. De *spectral strength* houdt rekening met de oppervlakteruwheid, terwijl de *volume scattering parameter* de verstrooiing binnen de sedimentlagen beschrijft. In een poging om de benodigde rekentijd te beperken, wordt een tweede model bekeken. In dit model wordt de reflectiecoëfficiënt van de echo energie afgeleid en empirisch gerelateerd aan de gemiddelde korrelgrootte, zoals voorgesteld in [16]. Deze aanpak blijkt beperkt door de openingshoek. Zelfs voor echoloden met een grote bundelbreedte is het model beperkt tot middelgrote en grote korrelgroottes, aangezien

de reflectie coëfficiënt niet gevoelig is voor gemiddelde korrelgroottes van meer als 5.5ϕ . De conclusie is dat alleen de fenomenologische benadering goed kan worden toegepast op de kleine korrelgroottes die bepalend zijn voor het MREA/BP'07 gebied. Toch vertonen de model-gebaseerde schattingen van de gemiddelde korrelgrootte redelijke overeenkomst met de monsters voor de middelgrote korrels in de Noordzee, als ook de *spectral strength* en de *volume scattering parameter* worden geschat en niet uit de empirische vergelijkingen worden berekend.

In hoofdstuk 5 wordt een *Bayesian approach*, zoals voorgesteld in [8], toegepast om *multibeam* echolood data te classificeren. Deze aanpak werkt met de intensiteit van het verstrooide (*scattered*) akoestische signaal per bundel. Door de bundels van de *multi-beam* echolood afzonderlijk te behandelen, wordt er rekening gehouden met de *across-track* variaties van de zeebodem. Aanpassingen zijn gemaakt om consistente resultaten voor de verschillende hoeken van de bundels en voor verschillende dieptes te verkrijgen. De *Bayesian approach* is gebaseerd op de veronderstelling dat de centrale limietstelling geldt en dat backscatter waarden dus normaal verdeeld zijn. De som van een aantal normale verdelingen, die elk een akoestische klasse van het sediment representeren, wordt vervolgens aan een histogram van deze *backscatter* waardes aangepast. Meestal worden de akoestische klassen aan korrelgrootte of sedimenttype gekoppeld. Inderdaad wordt getoond dat de verdeling van deze klassen representatief is voor de verdeling van het type sediment. Het is ook in overeenstemming met de kaart van *single-beam* echolood klassen. Uit een vergelijking met *ground truth* gegevens (monsters) blijkt daarentegen dat voor de interpretatie van de akoestische klassen andere parameters dan de korrelgrootte, zoals de aanwezigheid van gas, belangrijk zijn. Verder kunnen kleine structuren op de zeebodem doormiddel van deze benadering worden aangetoond.

De hoofdstukken 6 en 7 behandelen specifieke akoestische systemen, bestaande uit een bron en een array van ontvangers. Hier wordt een drijvend *vertical line array* met slechts vier hydrofonen en een stationaire bron gebruikt. *Matched-filter processing* (puls-compressie) wordt toegepast op de hydrofoon-data. Het akoestische veld wordt vervolgens gemodelleerd door *normal modes* en geo-akoestische inversie wordt toegepast op de parameters die beschrijvend zijn voor het gebied. Het onderliggende model is opgebouwd uit drie lagen: de waterkolom, een sedimentlaag en de subbodem. Bij het modelleren van het gehele akoestische veld moet met een groot aantal parameters rekening worden gehouden, waardoor een grote rekenkracht is vereist. Daarom is er onderzoek naar een optimale inversiestrategie en een optimale frequentieband uitgevoerd. De prestatie van de geo-akoestische inversie is onderzocht in drie verschillende omgevingen. De aanpak blijkt goed te werken voor zeer kleine korrelgroottes van $10 - 11 \phi$. Ook wordt aangetoond dat de aanwezigheid van gas kan worden aangegeven door de geïnvverteerde geluidssnelheid in het sediment. Deze benadering is alleen minder ideaal voor korte bron-ontvanger afstanden van minder dan een kilometer en in aanwezigheid van een sediment laag van meer dan 40 meter dikte.

Een vergelijking van alle gepresenteerde gebieds-beschrijvingen bevestigt de consistentie van het verkregen *environmental picture*. Uit het onderzoek blijkt dat de verschillende resultaten fenomenen kunnen verklaren, die niet aan korrelgrootte kunnen worden gerelateerd. Bovendien is aangetoond dat een combinatie van de classificatie van de bovenste sedimentlaag, door middel van hydrografische metingen, en de gelaagdheid van het sediment, verkregen uit seismische metingen, representatief is voor de selectie van gebieden voor een *subseafloor*-sediment-classificatie door middel van geo-akoestische inversietechnieken.

Acknowledgements

The research presented in this thesis is financially supported by The Netherlands Organisation for Applied Scientific Research (TNO) and by the Office of Naval Research. It has been carried out as cooperation between the Delft University of Technology (TU Delft) and Université libre de Bruxelles (U.L.B.).

This thesis would not be realized without the help and support of many people. Regrettably, I cannot acknowledge all of them by name.

First of all, I would like to thank my supervisors Prof. Dick G. Simons from TU Delft and Prof. Jean-Pierre Hermand from U.L.B. for their guidance throughout this project. Their advice and critical feedback have significantly improved the quality of research presented here. Jean-Pierre Hermand has provided a large amount of the data presented in this thesis and has contributed with his ideas of interpreting the results, for which I am very grateful. I would like to thank him for inviting me to Brussels several times to discuss the findings. I have been fortunate that Dick Simons has given me the opportunity study various aspects of the underwater acoustics, which allowed me to see the environmental picture as a whole. I also owe my gratitude to him for giving me the time to finish the thesis in my own pace and for making me finish in the end. Furthermore, I would like to thank Dick Simons for correcting my Dutch translation of the summary and propositions.

I am also very grateful to Mirjam Snellen for her daily supervision. She always had an open ear for questions and never tired of sharing her experience with me. Her lectures in underwater acoustics also prepared me well for the challenges ahead.

The members of the doctoral committee are highly acknowledged for their thorough review of this thesis.

The support of all individuals and institutions involved in the MREA/BP07 joint research project is highly appreciated. Especially, the contributions of the Royal Netherlands Navy, TNO, and NATO Undersea Research Centre in the observational program are hereby deeply acknowledged. Special thanks go to Piero Boni and Paola Nardini for the processing of the seismic data and the preparation of the environmental database, respectively.

I owe my thanks to Gerrit Blaquiere from TNO, who introduced me to the sonar group of TNO and invited me to present my work. The discussion of my work during these presentations has challenged and enriched my ideas. I would like to thank all members of the sonar group who joined the discussions and have given an inspiration for my research.

Further, I would like to thank my colleagues and former colleagues from both TU Delft and U.L.B. for their help and support. From U.L.B., I especially want to thank Olivier Carrière for his time comparing our results and for sharing his desk during the meetings in Brussels. Special thanks go to Ali Reza Amiri-Simkooei, my first roommate at TU Delft, for his help with the classification approach and the discussion of the classification results. Ali Reza, thank you also for providing a template in \LaTeX format for this thesis. I would also like to express my thanks to all other members and former members of the acoustic remote sensing group at TU Delft that helped me to enjoy my time at TU Delft. In particular but not exclusively I think of Jelle de Plaa, Jeroen Janmaat, Mathieu Colin, Dimitrios Eleftherakis, Julius Fricke, and Michael Arntzen. I will not forget the breaks with hot chocolate, the nice conversations, the cooking events, the drinks we had together, and my efforts to convince some of you of joining me in geocaching. I would like to acknowledge the help provided by Mathieu Colin in translating the French forms.

During my time at TU Delft we changed groups several times. All colleagues from the related groups I would like to thank for the enjoyable atmosphere at work and especially during our get-togethers at lunchtime. Thank you, Roderik Lindenbergh, for introducing me to The Netherlands Center for Coastal Research (NCK).

I owe my gratitude to all secretaries taking care of the formalities concerning my work. In memory of Ria Scholtes, for here warm welcome when I arrived at TU Delft. Unfortunately she left us so early. Special thanks go to Lidwien de Jong for her never ending support and attention. I would like to acknowledge Vera van Bragt and Geeta van der Zaken for their help with the formalities to complete my thesis.

Finally, I would like to thank my family and friends for their moral support. Especially, I am very grateful to my husband, Christian, who readily agreed on moving to the Netherlands and allowed me to take on this challenging research. Without his patience I would not have succeeded in finishing this thesis. Thank you also for spending so much time with our daughter Laura to provide me with enough space to finish this thesis.

Curriculum vitae

Kerstin Siemes, formerly Kerstin Herms, was born on the 11th of May 1978 in Wermelskirchen, Germany.

After having experienced a preeducation in Mathematics and Geographie (lectureship) from 1998 to 2002, at Bonn University, Germany, she continued with studies in Geodesy and Geoinformation, also at Bonn University, Germany. In March 2007, she completed her degree with a diploma thesis on 'Exploration of the scalespace with respect to the extraction of buildings in terrestrial coloured images' and was rewarded with the DVW-Award for good and fast studies in Geodesy and Geoinformation. Directly after, Kerstin worked half a year as a graduate assistant at the Department of Photogrammetry, at Bonn University, Germany.

At the end of 2007, Kerstin started her doctoral research in the field of underwater acoustics in the Acoustic Remote Sensing Group, currently part of the Air Transport and Operations Group, Faculty of Aerospace Engineering, Delft University of Technology (TU Delft), The Netherlands. The research is carried out in joint cooperation with the Environmental Hydroacoustics Lab, Université libre de Bruxelles (U.L.B.), Belgium. The presented thesis covers her work in the field of underwater environmental classification.

Kerstin lives with her husband Christian and daughter Laura in The Hague and enjoys geocaching in her free time.

Bibliography

Peer-reviewed journals

K. Siemes, M. Snellen, A. R. Amiri-Simkooei, D.G. Simons, and J.-P. Hermand: "Predicting spatial variability of sediment properties from hydrographic data for geo-acoustic inversion," *IEEE Journal of Oceanic Engineering*, 35(4), pp. 766–778, 2010.
contribution to Chs. 3, 4, and 5

M. Snellen, K. Siemes, and D.G. Simons: "Model-based sediment classification using single-beam echo sounder signals," *J. Acoust. Soc. Am.*, Volume 129, Issue 5, pp. 2878–2888, 2011.
contribution to Chs. 3 and 4

Conference proceedings

K. Siemes, M. Snellen, D.G. Simons, J.-P. Hermand, M. Meyer, and J.-C. Le Gac: "High-frequency multibeam echosounder classification for rapid environmental assessment," in

Proceedings of the European conference of Underwater Acoustics (ECUA), Paris, 2008.
contribution to Ch. 5

K. Siemes, M. Snellen, D.G. Simons, and J.-P. Hermand: "Using MBES backscatter strength measurements for assessing a shallow water soft sediment environment," in *Proceedings of the Oceans IEEE conference*, Bremen, 2009.
contribution to Ch. 5

K. Siemes, M. Snellen, D.G. Simons, and J.-P. Hermand: "Inverting for bottom parameters in shallow-water soft sediment environments using MBES backscatter strength," in *Proceedings of the Underwater Acoustic Measurements (UAM) conference*, Nafplion, 2009.

M. Snellen, K. Siemes, and D.G. Simons: "A model-based method for reducing the sound speed induced errors in multi-beam echo-sounder bathymetric measurements," in *Proceedings of the Oceans IEEE conference*, Bremen, 2009.

M. Snellen, K. Siemes, and D.G. Simons: "An efficient method for reducing the sound speed induced errors in multibeam echosounder bathymetric measurements," in *Proceedings of the Underwater Acoustic Measurements (UAM) conference*, Nafplion, 2009.

D.G. Simons, M. Snellen, and K. Siemes: "The potential of inverting geo-technical and geo-acoustic sediment parameters from single-beam echo sounder returns," in *Proceedings of the Underwater Acoustic Measurements (UAM) conference*, Nafplion, 2009.

K. Siemes, M. Snellen, D.G. Simons, and J.-P. Hermand: "Feasibility of geo-acoustic inversion using a sparse array of hydrophones at short range," in *Proceedings of the European Conference on Underwater Acoustics (ECUA)*, Istanbul, Turkey, 2010.
contribution to Ch. 6

M. Snellen, K. Siemes, and D.G. Simons: "On the practical applicability of single-beam model-based seafloor classification," in *Proceedings of the European Conference on Underwater Acoustics (ECUA)*, Istanbul, Turkey, 2010.
contribution to Ch. 4

K. Siemes, J.-P. Hermand, M. Snellen, and D.G. Simons: "Frequency and signal type dependence of the performance of broad-band geoacoustic inversion in a shallow water environment with soft sediments," in *Proceedings of the Underwater Acoustic Measurements (UAM) conference*, 2011.
contribution to Chs. 3 and 6

Other

D.G. Simons, A. Amiri-Simkoei, K. Siemes, and M. Snellen: "Recent developments in multi-beam echo-sounder processing - The multi-beam potential for sediment classification and water column sound speed estimation," in *Management of massive point cloud data: wet and dry*, P.J.M. van Oosterom et al., Eds., NCG 49, pp.33–44, 2010.